MOLECULAR COMPLEXATION AND DEFECT DYNAMICS IN DIAMOND BY PARTICLE-SOLID INTERACTIONS

Bryan Patrick Doyle

A thesis submitted to the Faculty of Science, University of the Witwatersrand, Johannesburg, in fulfilment of the requirements for the degree of Doctor of Philosophy.

Johannesburg 1999

I declare that this thesis is my own work. It is being submitted in fulfilment of the requirements for the degree of Doctor of Philosophy at the University of the Witwatersrand. It has not been submitted before for any degree or examination at any other university.

Bryan Patrick Doyle

24th day of March 2000

To my father

Kevin Patrick Doyle

1939 - 1987

who was the greatest man I ever knew

and whom I wish I could share my achievements with

and to my mother

Målfrid Doyle

who has lovingly cared for us and

lives every day in his memory with a smile on her face.

Abstract

This thesis addresses, as its primary topic, the behaviour of the heavy ion ^{111}In in the diamond lattice. More specifically the lattice sites occupied after implantation and annealing have been investigated using the technique of 2-dimensional Conversion Electron Emission Channeling (CEEC). The study of a suite of carefully chosen, defect-rich diamonds has allowed the investigation of In-defect interactions and any resultant complex formation. The experimental work has been supported by density functional theory calculations of the energetically most stable site for ^{111}In in pure diamond.

We propose, following from the results in this thesis, that vacancies are the most important defect constituents in the final configurations of implanted and annealed indium in diamond. This is found to be the case independent of the other defects in the crystal, be they boron, hydrogen or nitrogen in different forms. The possibility of hydrogen complexation is however not excluded. The origin of the random fraction measured in previous studies is proposed to be partially due to In in different multi-vacancy complexes. Theoretically the most stable site for the In was found to be bond-centred in a di-vacancy.

Secondarily, the behaviour of hydrogen in diamond has been investigated through Elastic Recoil Detection analysis (ERDA). Diamond has a natural abundance of hydrogen. In order to fully interpret any In-H interactions that occur it is necessary to better understand the mobility of hydrogen in the diamond lattice. To this end the diffusion of both implanted and plasma loaded hydrogen has been studied. The naturally occurring hydrogen distributions in natural as well as in synthetic diamonds have also been studied with the same aim in mind. The ERDA measurements have necessitated the development of a sophisticated 3-dimensional ERDA system utilising a 2-dimensional position sensitive detector. The evolution of ERDA at this laboratory into a routine analytical tool has been a necessary part of this work. The mobility of hydrogen or

lack thereof has been found to be dependent on various factors. These include the starting configuration of the hydrogen species and whether pre-damage through ion implantation has been made to the crystal.

The work of this thesis is important in two contexts. Indium is a heavy ion and the results stress the importance of vacancies, both singly and multiply, in heavy ion implantation. This has ramifications for those wishing to use heavy ions in the fabrication of diamond electronic devices. Hydrogen is a common impurity in diamond and the findings here on its mobility (and lack thereof) are of relevance to the diamond physics community.

Acknowledgements

I would like to acknowledge the following people for their guidance, advice and support, without which this thesis would not have been possible:

- my supervisors, Doctor S.H. Connell and Professor J.P.F. Sellschop. Their support, encouragement and guidance were invaluable. One can only admire their enthusiasm for science and especially physics.
- My overseas collaborators, in particular Dr. U. Wahl for his help with the channeling measurements, both experimentally and with the analysis of the data; as well as Dr. J.E. Butler for sharing with us his insights on CVD diamond.
- Prof. J.E. Lowther, who performed the DFT calculations. Collaboration between experimentalists and theorists is so important.
- All my SRCNS collaborators: E.J. Storbeck - who helped me solve all the channeling mysteries and didn't mind when I interrupted his weekends; Dr. E. Sideras-Haddad - he taught me a great deal; M.G. Bossenger (Matty), C.G. Fischer (well, well, well), I.Z. Machi, R.D. Maclear (who coded the ERDA analysis software), S.R. Naidoo - for implanting above and beyond the call of duty; Dr. R.W.N. Nilen (De Longhi), D.B. Rebuli (who selflessly helped me with so much work, and proof-read this thesis), T.G. Stevens - who taught me the intricacies of networking, and H. van Heerden.
- My other outside collaborators: Prof. K. Bharuth-Ram and Mr. K. Dewhurst.
- The technical staff of the SRCNS: J.S. Augustine (John A) - eternally ready to lend a helping hand; J.U.M. Beer (John B) - thanks dude man; A.H. Andeweg - always helpful; E. Rood and O. Pekar - the friendly faces of the workshop, K. Cooney, R. Son, I.D. McQueen, G.H. Wernick, N. Filmater, M. Rebale, R. Cruise, P. Babie and L. Matlhadisha - Eytha mpho!

- The administrative staff of the SRCNS: Mrs. P. Mclachlan - Pepsi - you added spark to the Schonland; Mrs. C.E. Dawood, Mrs. D.D. Monyamane.
- Those who helped with discussions and questions: Prof. H. Hofsäss, Dr. B. Lindgren, Prof. J.F. Prins.
- Dr. R. Hart, someone to talk to about sport, women and the fun things in life.
- Prof. H.J. Annegarn and S.J. Piketh: for new insights in science.
- All those who contributed to the coding of *manybeam* and FDD: Dr, U. Wahl, Prof. H. Hofsäss and the originators at Åarhus.
- All the students, who were friends as well: Mr. M.J. Butler, Ms. E.B. Meter, Ms. S.L. Meter, Dr. Z.Z. Vilakazi (The Black Flash), as well as J.D. De Wet and C.G. Smallman.
- Reuven Essig and Mark Dalton, for letting me poach the drawings of the accelerators.
- Prof. T. Derry, O. Malinga, S. Masala, A. Mthembu, Dr. T. Nam, C. Raluswinga, W. Tleane and Prof. J.I.W. Watterson for little things here and there.
- To friends and family for their support and encouragement, especially my brother Graham (Grammen).
- The one who stood by me this year when all I did was work and no play - Ruth, you complete me.

I wish to express my gratitude to the National Research Foundation (previously the Foundation for Research Development), the University of the Witwatersrand, the Schonland Research Centre for Nuclear Sciences, UNESCO, the IAEA and the Anglo American Chairman's Trust for financial support. I would also like to thank Messrs. De Beers Industrial Diamonds (Pty) Ltd. and the Naval Research Laboratory (Washington) for supplying the diamond samples used throughout this work.

Contents

List of Tables

List of Figures

Nomenclature

ADC : analogue to digital converter

BC : bond-centred

BWBA : Bloch wave Born approximation

CEEC : conversion electron emission channeling

CIRA : cold implant rapid anneal

CL : cathodoluminescence

CVD : chemical vapour deposition

DAS : data acquisition system

DC : direct current

DFT : density functional theory

DLC : diamond-like carbon

ESCA : electron spectroscopy for chemical analysis

EFG : electric field gradient

ENDOR : electron-nuclear double resonance

EPR : electron paramagnetic resonance

ERDA : elastic recoil detection analysis

ESR : electron spin resonance

GGA : generalised gradient approximation

GPIB : general purpose interface board

HPHT : high-pressure high-temperature

IBA : ion beam analysis

IR : infrared (spectroscopy)

LDA : local density approximation

LODDI : low-damage drive in

MQ NMR : multiple quantum nuclear magnetic resonance

μSR : muon spin rotation

NIM : nuclear instrumentation methods

NMR : nuclear magnetic resonance

NRRA : nuclear resonant reaction analysis

PAC : perturbed angular correlations

PC : polycrystalline

ppm : parts per million (atomic)

PSD : position sensitive detector

RBS : Rutherford backscattering spectrometry

RF : radio-frequency

ROI : region of interest

RTA : rapid thermal anneal

S : substitutional

SIMS : secondary ion mass spectrometry

SRCNS : Schonland Research Centre for Nuclear Sciences

SSB : silicon surface barrier (detector)

TOF : time-of-flight

Chapter 1

Introduction

1.1 Motivation

Diamond shows much promise as an important semiconductor material of the future, due to its many extreme properties, such as its large breakdown field, high thermal conductivity, radiation hardness, extremely high Debye temperature (and resultant very low heat capacity), and high saturated electron velocity. Other extreme properties of diamond include its hardness (diamond has the greatest known resistance to plastic flow), low coefficient of thermal expansion, extremely high atomic number density and compiete optical transparency (barring defects) in the wavelength region 2.5 μm to 225 nm. In any semiconductor knowledge of the behaviour of impurities, in particular of dopant-impurity complexes is paramount. Due to diamond's metastable nature ion implantation is currently the most viable method known to introduce dopants into the bulk. The exact conditions of implantation and subsequent annealing have been shown to be of utmost importance in ion implantation in diamond (Prins, 1993a, and Prins, 1993b). In order to achieve n-type doping, some attention is switching to heavier dopant atoms (Prins, 1998b), in the belief that they might generate shallow dopant states which would be suited to the manufacture of diamond electronic devices. ^{111}In has been a much used probe to study the interactions of heavy ions with materials.

The primary reason for this is that the particulars of this radioactive isotope's decay, namely the emission of conversion electrons coupled with a two-gamma-ray cascade, make it a suitable tool for various experimental techniques[1]. One of these is *Conversion Electron Emission Channeling* or *CEEC*. Due to the periodic lattice structure of a crystal the yield of particles emitted from a site within the crystal, measured at a point outside the lattice is non-uniform, depending both on the lattice site of the emitter and the angle to the crystal direction at which it was detected. Allied with powerful theoretical models which enable one to calculate quantum mechanically the yield expected from different lattice sites one is able to deduce the occupied lattice site/sites. CEEC thus allows one to garner a vast amount of information on the interactions of the ^{111}In probe. There has been a fair amount of work on ^{111}In in the pure type IIa diamond system (Burchard *et al*, 1993, Quintel *et al*, 1996, and Bharuth-Ram *et al*, 1996). A two-stage annealing cycle has been identified in the case of diamond for the In site (Burchard *et al*, 1993, Quintel *et al*, 1996, and Hofsäss *et al*, 1993), with the first stage occurring at between 300 and 600 K and the second after 1200 K. These results indicate a strong (between 35 and 60%), substitutional or near-substitutional (less than 0.1 Å away), fraction. The possibility of a significant tetrahedral interstitial site has been ruled out by earlier emission channeling results (Hofsäss *et al*, 1993).

We have extended these studies to encompass a range of defect-rich diamond systems in order to gauge whether In forms molecular complexes with any of the given defects. This has been achieved by studying a carefully chosen suite of natural diamonds containing nitrogen (in various configurations), boron and extended defects such as dislocations and grain boundaries. Studies on diamonds containing artificially introduced hydrogen have also been performed. Previous CEEC results have also been elucidated through the capture of 2-dimensional data, as opposed to the more usual 1-dimensional method. The 2-dimensional spectra contain greater information due to both planar channeling and the fine structure caused by quantum mechanical diffrac-

[1]As a group III element In is also a possible candidate for an acceptor impurity if it can be incorporated on substitutional sites in diamond, without causing substantial lattice damage.

tion effects being observed simultaneously with the axial channeling effects.

Further insight into the In-in-diamond system has also been achieved through the calculation of the energetically most stable site for In in the pure diamond lattice. *Ab initio* plane-wave pseudopotential local density Density Functional Theory (DFT) calculations were performed on this particular system for the first time. Various different sites for the In atom were modelled and lattice relaxation was employed to yield realistic results.

The secondary thrust of this thesis has been the study of the diffusion and distributions of hydrogen in diamond, to indirectly gain more insight into the configurations/complexes in which it plays a role. In silicon (due to its diamond structure often being used for comparison), the passivation of indium by hydrogen is well known (Wichert *et al*, 1987, Deicher *et al*, 1989, and Skudlik *et al*, 1992a), and as mentioned above, In-H interactions are probed for in this work. The primary purpose of the hydrogen measurements was to gain as much information on its behaviour in diamond as possible, as a basis for the interpretation of any observed In-H interactions, or the lack thereof. Hydrogen is a common impurity in both natural (Sellschop *et al*, 1980) and synthetic diamond (Madiba *et al*, 1988). In natural diamond it is introduced in the high pressure and high temperature genesis deep within the earth's core, possibly as water and methane. Hydrogen also serves a vital catalytic role in the growth of synthetic diamond in the Chemical Vapour Deposition (CVD) process. It is often incorporated into the bulk during this process. In silicon hydrogen is known to activate or passivate optical and electrical centres (due to its tendency to interact with weak or stretched bonds), form extended structures (platelets), catalyse the diffusion of oxygen etc. (Estreicher, 1995). Accordingly there has been a vast increase in research in this field in recent times. Many important questions do however remain unanswered.

We have used the technique of Elastic Recoil Detection Analysis (ERDA) to obtain

3-dimensional images of the hydrogen distributions within the diamond bulk. ERDA is basically forward Rutherford scattering in which incident heavy ions are used to recoil the light ions of interest into a detector placed in a forward position. An integral part of this work has been the development of a 2-dimensional position sensitive detector (PSD) system which has enabled a great increase in detector efficiency without an accompanying loss of energy resolution. This system has allowed 3-dimensional ERDA to become a routine analysis technique at the Schonland Research Centre for Nuclear Sciences (SRCNS). A number of different samples with varying hydrogen concentrations and distributions have been studied. Primarily the mobility of hydrogen introduced into diamonds, both through ion implantation and that attempted via plasma loading, has been investigated. The results have been brought together with previous work from the literature in order to increase understanding of the mechanisms involved.

In summary we have used the experimental technique of 2-dimensional Conversion Electron Emission Channeling to extend existing knowledge on the In-in-diamond system to include defect-rich systems. We have also theoretically modelled the pure In-in-diamond system using Density Functional Theory to find the energetically most stable site. Secondarily, we have used ERDA to investigate hydrogen mobility and distributions in various diamond samples under different conditions, to complement the CEEC work on hydrogen-rich diamond. The emphasis has been to look, both directly and indirectly, for the formation of complexes in the diamond bulk.

1.2 Plan of Thesis

This thesis is presented in the following fashion. We begin with a literature review of the pertinent diamond physics. For each method used there is a theoretical chapter which lays the basis for the method used. Each is followed by a chapter giving the details of the measurement with the obtained results. In the case of the DFT calculations the theory and the results are contained in a single chapter. We end with a detailed discussion which attempts to explain the results of the experiments and calculations,

in combination with earlier work from the literature.

In **chapter 2** information on diamond is given, with special focus on previous work on the complexation and behaviour of In and hydrogen in diamond. The theory of channeling and in particular the quantum mechanical "many-beam" treatment needed for electron channeling at these energies is given in **chapter 3**. Experimental results on In in diamond obtained via CEEC are given in **chapter 4**. The calculations on the In-in-diamond system using DFT, as well as a theoretical background to DFT are given in **chapter 5**. A review of the ERDA technique, along with the necessary fundamental kinematical and scattering processes, is presented in **chapter 6**. The results on hydrogen in diamond using ERDA are given in **chapter 7**. All the results are discussed in depth in **chapter 8** and final conclusions are in **chapter 9**. Finally an appendix containing publications resulting from this work as well as other studies which were made in the duration of this thesis are in **Appendix A**.

This thesis has addressed a number of outstanding issues with regard to the behaviour of the heavy ion ^{111}In and the light ion hydrogen. It is hoped that the results, in the form of the published papers, will form a significant contribution to the field. The In work is especially important to those interested in employing heavy ions to create n-type diamond, the hydrogen work being of general interest to anyone concerned with this particular defect in the diamond bulk. Some of the hydrogen work deals more specifically with issues connected with the CVD growth of diamond.

Chapter 2

Molecular Complexation in the Diamond Lattice: Indium and Hydrogen

Carbon exists in many allotropic forms. Of these diamond exhibits the most extreme properties of all known materials. Its large breakdown field, high thermal conductivity and high saturated electron velocity, coupled with recent advances in n-type and p-type doping (Prins 1988, Prins, 1998b), suggest it for a large number of electronic device applications. Pure diamond is a wide band-gap semiconductor, with an indirect energy gap of 5.49 eV at 77 K (Clark *et al*, 1964). The important role played by defects and impurities in determining the various properties of diamonds, specifically in this case their electrical properties, is a vital reason for their study.

2.1 The diamond lattice

Diamond is the cubic form of crystalline carbon and belongs to the space group $O_h^7(F4_1/d\bar{3}2/m)$ with two atoms per primitive (Bravais) cell. It can be seen as two

interpenetrating face centred cubic lattices displaced by $(\frac{1}{4}, \frac{1}{4}, \frac{1}{4})a_0$ along the body diagonal, where a_0 is the edge length of the cubic unit cell and has a value of 3.567 Å. The diamond structure is shown in Figure 2.1. Diamond is metastable and if subjected to high temperatures (~900 K in atmosphere, ~1800 K in an inert atmosphere or ultra-high vacuum, see Evans, 1979, and refs. therein), or if the lattice is damaged above a certain threshold it will revert to the graphitic form. A number of studies on this ion-induced graphitization have been performed (see for instance Spits *et al*, 1994), all dependent on ion type. Results independent of ion type, showing an amorphization threshold of 10^{22} vacancies.cm^{-3}, have further clarified the issue (Uzan-Saguy *et al*, 1995).

The nearest-neighbour distance is 1.544 Å, which is nearly 10% larger than in graphite (the most common carbon allotrope), yet the density of diamond, 3.515 g/cm^3, is 56% greater than that of graphite. This is due to the high anisotropy of the graphite structure. Within the diamond lattice the individual carbon atoms are all tetrahedrally coordinated and bonded to four identical carbon atoms. The C-C bond is sp^3 hybridized which accounts for the high displacement energy, 35±5 eV (see Bourgoin and Massarani, 1976, and references therein[1]). Several good reviews on diamond physics exist, among them those by Field, (Field, 1992), and Davies, (Davies, 1994a).

Two other elemental materials, namely silicon and germanium, have the diamond structure, which provides the basis for many comparisons between them and diamond, in both bulk properties as well as for the behaviour of any impurities or defects that they might contain.

[1]The displacement energy is defined as the recoil energy transmitted to an atom in the lattice that is required to produce a displacement. In the case of diamond this is the energy required to break the four carbon-carbon bonds, allow the displaced atom to pass through the saddle point of the potential into an interstitial position plus the energy associated with the resultant lattice distortion.

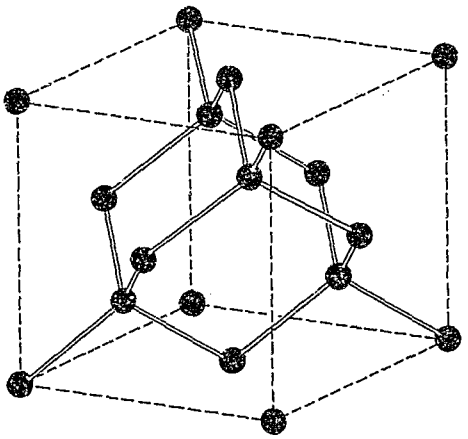

Figure 2.1: Crystal structure of diamond, showing the tetrahedral bond arrangement (from Kittel, 1986)

2.2 Impurities and defects in diamond

Diamonds are classified according to the dominant defects that they contain. Those that contain nitrogen as a dominant defect are termed type I. Most natural diamonds belong to the subdivision type Ia, where the nitrogen is believed to be present in aggregated form. The majority of the aggregates are what are known as A or B centres. An A centre is believed to be a pair of nearest-neighbour nitrogen atoms (Davies, 1976), while a B centre is believed to be made up of four nitrogen atoms surrounding a vacancy (Davies, 1977). These configurations are shown in Figure 2.2.

Within this class one has type IaA, IaB and IaAB diamonds, depending on whether only A centres, B centres or both occur in the particular stone. The A and B centre nitrogen aggregates are non-paramagnetic. If the nitrogen is present as single substitutional defects then the sample is termed type Ib. These defects are known as P1 centres, shown in Figure 2.2. They form deep donors situated at $\approx$1.7 eV below the conduction band (Farrer, 1969). Type Ib stones are easily identified by their electron

paramagnetic resonance (EPR) signal and characteristic one-phonon absorption spectrum. Synthetic stones grown by the high-pressure high-temperature (HPHT) method are commonly type Ib (Chrenko *et al*, 1971). Nitrogen pairs (A centres) have been detected in HPHT stones grown at relatively higher temperatures (Kluev *et al*, 1973, and Kanda *et al*, 1990). Natural type Ib stones are very rare but specimens sharing type Ia and type Ib character do occur (Woods and Collins, 1983). Another common nitrogen defect is the P2 or N3 centre, comprising three nitrogen atoms bonded to a vacancy. This is also shown in Figure 2.2.

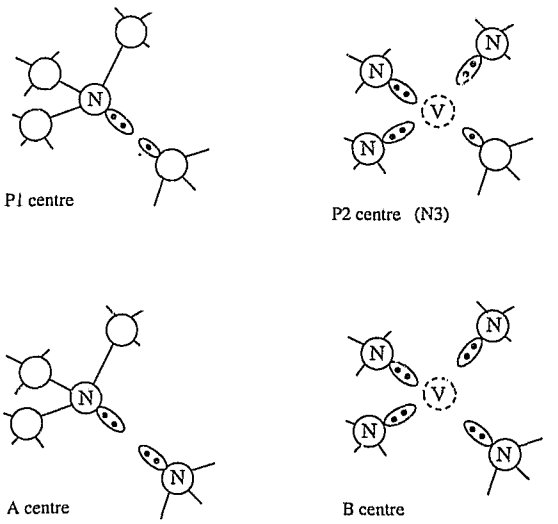

Figure 2.2: Schematic diagrams of some of the important nitrogen (N) and vacancy (V) related defects in diamond. The black dots represent unbonded electrons and the unmarked circles represent carbon atoms. Courtesy of RWN Nilen (Nilen, 1998).

Concentrations of nitrogen below 1-2 ppm in both aggregate or substitutional form are below the detection limit of conventional infrared (IR) instrumentation (Woods, 1992). Such samples are classified as type IIa, if non-semiconducting, and type IIb if semiconducting[2]. The semiconducting properties of type IIb diamond are due to substitutional boron (Chrenko, 1973, Lightowlers and Collins, 1976, and Sellschop *et al*, 1975), which forms shallow acceptors. Type IIa diamonds tend to be less perfect in general than type IIb, having more mosaic structure.

There is good evidence that type IIa diamonds also contain boron, at lower doses than in type IIb stones (Prins, 1998a), but which are not electrically active. It is thought that vacancies in diamond are deep lying donors which can compensate boron acceptors (Dyer and Ferdinando, 1966, Collins *et al*, 1969, and Vermeulen and Farrer, 1975). More recent work postulates vacancy clusters or sub-lattices - "vacloids", as the compensating donors for boron acceptors in implanted diamonds (Prins, 1989), and this is thought to be the case in natural type IIa samples as well (Prins, 1998c). This hypothesis has led to some controversy, most notably due to disagreements over the distributions of damage-induced vacancies and interstitials (Gippius, 1995). The work of Prins both experimentally and the accompanying hypotheses, does however appear to offer the best future for the production of diamond semiconductor devices[3].

2.3 Vacancies and self-interstitials in diamond

The neutral vacancy in diamond, V^0, formed by the removal of a carbon atom and its four valence electrons, is one of the most common defects in diamond, especially as it is easily formed during ion implantation. It gives rise to a characteristic optical

[2]Although IR measurements of the total nitrogen content are the accepted method for determining diamond type, analyses using nuclear reactions (which show the entire nitrogen content, independent of bonding configuration), have shown the total nitrogen content to lie above that determined by IR, yielding the following average concentrations: type Ia, 200-5000; type Ib, 150-600; type IIa, 4-40; and type IIb, 4-40 ppm (atomic), (Sellschop, 1992).

[3]More information can be found in the cited papers.

absorption band, known as GR1, (see for instance Stoneham, 1992). V^0 readily diffuses in diamond, with an activation energy most recently measured at 2.3±0.3 eV (Davies *et al*, 1992). There is a school of thought that believes this activation energy to be lower, of the order of 1.7 eV (Clark and Palmer, 1960). This makes diffusion a viable process for usual anneal times (of the order of 30 min.), at temperatures between 898 and 1073 K.

It has been found that vacancies passivate both donors and acceptors. At temperatures where vacancies become readily mobile they diffuse and have been found to passivate large dopants (Prins, 1998d).

Negative vacancies, V^-, or ND1 centres, composed of a neutral vacancy that has trapped an electron, are also present in diamond. Heating or illumination activates charge-exchange processes between the V^0 and V^- centres, (see Davies and Manson, 1994). ND1 centres are more easily observable in type Ib diamonds where the Fermi level lies nearer to the conduction band which facilitates these charge transfer mechanisms (Prins, 1992).

The mirror image as it were of the vacancy is the self-interstitial. As in the case of the vacancy it is most easily formed during irradiation. Interstitials are more mobile than vacancies, with an activation energy of 1.3 eV (Clark and Palmer, 1960, Prins, 1993a). Diffusion is thus prevalent between 548 and ~873 K. The fact that interstitials migrate without carrier defects at room temperature leads to the conclusion that they diffuse by means of a "direct" mechanism - jumping from interstice to interstice. This has been shown to also be possible for many other foreign atoms, for example boron (Spits *et al*, 1991).

Thus there exist two distinct regimes in the annealing of irradiated or implanted diamond, one where interstitial diffusion dominates and another where vacancy diffusion

does. These diffusion mechanisms lead to recombination processes. The reconstruction to a perfect lattice structure is hampered by a tendency for interstitials to diffuse out of the diamond bulk, leaving an excess of vacancies. These agglomerate to form the vacancy clusters or "vacloids" mentioned in the previous section. These form deep lying donors $\approx$4 eV below the conduction band (Prins, 1989).

In order to control the recombination of vacancies and interstitials after ion implantation and to ensure the activation of the implanted dopants a number of annealing schemes have and are being developed. These include:

- Cold Implantation-Rapid Anneal (CIRA), where implantation is performed at very low temperatures ($\sim$77 K), such that the implanted atoms and the vacancies and self interstitials formed during implantation are "frozen in". This is followed by a rapid thermal anneal (RTA), in which recombination of vacancies and interstitials (both intrinsic and extrinsic) occurs (Prins, 1988)

- Low-damage Drive In (LODDI), in which the dopant atoms are implanted in a layer adjacent to one that already contains an especially created low vacancy concentration. The dopant atoms are driven into this low vacancy region during annealing and annihilate with the vacancies (Prins, 1998e).

2.4 Indium in the diamond lattice

Indium has been a much used probe to study the interactions of heavy ions in the diamond lattice. A number of CEEC and Perturbed Angular Correlations (PAC[4]) studies have been performed, notably on type IIa samples[5]. The pertinent parameters of these studies are tabulated in Table 2.1. Although variations have been found in these studies, common features can be extracted,

[4]PAC uses the hyperfine interaction of the radioactive probe atom with its electronic surroundings to deduce information on its bonding partners and atomic surroundings.

[5]This is with the possible exception of the work of Kalish *et al* where the type of diamond used was not specified (Kalish, 1979).

Authors	Technique	In site fractions	Other observations
Kalish *et al* 1979	PAC	3% with ν_Q=117 MHz, 1% with ν_Q=19 MHz	Diamond type not specified, Annealing stage $\approx$ 1000 K, EFG symmetry orientation unimportant, Immediate probe surroundings don't "heal" under annealing
Appel *et al* 1981	PAC	5% with ν_Q=117 MHz	EFG has $\langle 111 \rangle$ symmetry
Burchard *et al* 1993	PAC, CEEC	10% with ν_Q=117 MHz, 60% at substitutional or near-substitutional sites	Formation of ν_Q=117 MHz defect requires high initial damage level, Annealing stage above 1000 K, Majority of ^{111}In on *subst. sites* but high local defect conc.

Table 2.1: Results of previous studies of the lattice locations of ^{111}In in diamond. PAC results identify unique sites through their quadrupole coupling frequency, ν_Q, while CEEC identifies actual lattice site locations. The EFG is the electric field gradient experienced by the probe atom in PAC measurements.

Authors	Technique	In site fractions	Other observations
Hofsäss *et al* 1993	CEEC	up to 45% subst. and 55% random or 50-60% near-subst.(~0.1 Å) and rest random	2 annealing stages: 300-600 K and ~1000 K
Bharuth-Ram *et al* 1996	PAC, CEEC	35% substitutional or near-subst. (~0.2 Å), 10% with ν_Q=117 MHz 8% with ν_Q=315 MHz	Implant at 1373 K or 295 K implant plus 1673 K anneal yield same max. subst. fraction, All In atoms have defect(s) within the 1st or 2nd neighbour
Quintel *et al* 1996	CEEC	40% substitutional or 50% near-subst. (~0.15 Å)	2 annealing stages: 300-600 K and 1173-1273 K, same max. fraction for high temp. implant or room temperature implant plus anneal

Table 2.1: cont.

- a high temperature anneal (> 1000 K), is needed in order to obtain the unique ν_Q=117 MHz PAC configuration, or to drive a large proportion of the In atoms onto substitutional or near-substitutional sites
- the anneal actually is a two stage process with the first anneal occurring at 300-600 K and the second at just above 1000 K
- there appears to be no measurable difference between a room temperature implant followed by a high temperature anneal, and a high temperature implant (for doses $\sim 10^{12}$ - 10^{13}cm^{-2})
- the surroundings of the In atom after annealing are still defect-rich due to the damage caused by the implantation
- 35-60% substitutional or near-substitutional ($\lesssim$0.2 Å) fractions are measured using CEEC
- 3-10% of the 117 MHz configuration can be obtained with PAC. This unique defect has still to be identified, but appears to be damage related.

It must be kept in mind that the PAC and CEEC measurements measure different parameters and thus the PAC and CEEC results provide complementary information, the conclusions of which do not necessarily substantiate each other[6]. As previously mentioned the majority of these studies were performed on type IIa diamonds and no information exists on defect-rich systems.

[6]A comment should also be made on the work of Hofsäss (Hofsäss *et al*, 1993), in that uncertainties do exist in the site identification due to the lack of a complete 2-dimensional treatment, also in the displacement magnitudes from substitutional sites and in the experimental smoothing of the theoretical simulations (Wahl, 1998).

2.5 The role of hydrogen in the growth dynamics of CVD diamond

One of the main reasons for the explosion in diamond research in the past decade has been the vast improvements in the quality of and ease with which Chemical Vapour Deposition (CVD) diamonds can be grown. This is a result of the increase in knowledge of the gas phase and surface chemistry processes that occur. A simplified schematic of these processes is shown in Figure 2.3. Present studies focus primarily on diamond CVD reactors which are low-pressure, hot-filament or microwave systems, containing a mixture of hydrogen and a hydrocarbon gas, typically methane, with the hydrocarbon concentration being less than 1% (Goodwin and Butler, 1997). The parameters of such a system are typically a pressure of 20-30 Torr and a substrate temperature of 800-900°C which results in a growth rate of the order of 1 μm/hr.

In the diamond CVD process a crucial role is played by free radicals, particularly atomic hydrogen. In hot-filament systems atomic hydrogen is produced by thermal decomposition of H_2 on the hot filament substrate. In plasma-enhanced systems such as microwave, radio-frequency (RF) or DC arcjet reactors, further atomic hydrogen to the above is produced in the plasma through the interaction of hydrogen molecules and the energetic free electrons of the plasma,

$$H_2 + e^- \rightarrow H + H + e^- \tag{2.1}$$

If the system is under higher pressures (> 100 Torr), collisions between H_2 and energetic heavier particles in the plasma becomes important,

$$H_2 + M \rightleftharpoons H + H + M \tag{2.2}$$

There are a number of reactions that cause recombination of molecular hydrogen, among these the reverse of equation 2.2. Among these reactions,

$$H + CH_4 \rightleftharpoons CH_3 + H_2 \tag{2.3}$$

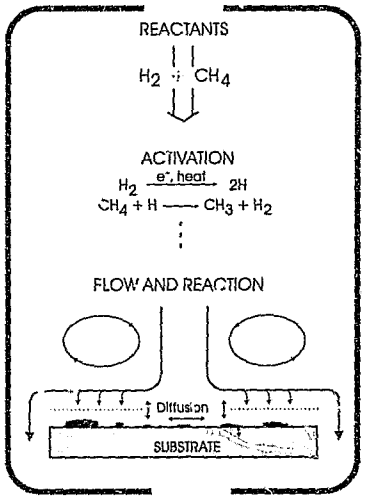

Figure 2.3: Schematic of processes occurring during diamond CVD (from Butler and Woodin, 1993).

is of great importance as it forms methane radicals which are the building blocks of the diamond CVD crystal. This and the removal of hydrogen from the diamond surface i.e.

$$C_dH + H \rightarrow C_d^* + H_2 \tag{2.4}$$

where C_dH represents a hydrogen-terminated surface site and C_d^* an unterminated site, are the major roles of atomic hydrogen in diamond CVD. Equation 2.4 is in equilibrium with the hydrogenation of the growth surface due to the constant flux of atomic hydrogen onto that surface,

$$C_d^* + H \rightarrow C_dH \tag{2.5}$$

CH_2 and atomic carbon have also been postulated as the constituents for carbon addition to the diamond surface. These are thought to occur in sufficiently activated

systems, that is those with a H/H_2 ratio of more than a few percent. They are generated by an extension of equation 2.3,

$$CH_m + H \rightleftharpoons CH_{m-1} + H_2 \tag{2.6}$$

The diamond CVD growth process is by no means completely understood. A good review of work so far has been made by Goodwin and Butler (Goodwin and Butler, 1997). What is most definitely clear is the definitive role played by hydrogen in CVD growth, and that the diamond is exposed to a high concentration of activated hydrogen, which suggests its possible incorporation (see Section 2.6.3).

2.6 Hydrogen in the diamond lattice

Hydrogen plays an important role in diamond, in particular in CVD diamond where it is probably the most important, but not necessarily homogeneously distributed, impurity. This importance is analogous to the case of silicon where hydrogen is known to activate or passivate optical and electrical centres (due to its tendency to interact with weak or stretched bonds), form extended structures (platelets), catalyse the diffusion of oxygen etc. (Estreicher, 1995). Accordingly there has been an vast increase in research in this field in recent times.

2.6.1 Muonium

When polarised positive muons enter the bulk of a solid they can interact with electrons to form a bound state known as muonium,

$$\mu^+ + e^- \rightarrow \mu^+ e^- \tag{2.7}$$

This decays with a half-life of 2.2 μs emitting a positron and two neutrinos. Detection of the positron allows the interactions of the muonium to be investigated. Muonium is a light chemical isotope of hydrogen. In Table 2.2 various properties of muons, protons, muonium and hydrogen are compared. A further explanation of this Muon Spin

Nuclei		
	muon (μ^+)	proton (p^+)
Mass (m_e)	206.768	1836.15
Charge (e)	+1	+1
Spin	1/2	1/2
Half-life	2.2μs	$> 10^{31}$y
Atoms		
	Muonium (Mu)	Hydrogen (H)
Reduced mass (m_e)	0.995	0.999
Radius (Å)	0.531	0.529
Activation energy (eV)	-13.54	-13.59

Table 2 2: A comparison of some of the important properties of muons and protons, and muonium and hydrogen

Rotation (μSR) technique can be found in the book of Schatz and Weidinger (Schatz and Weidinger, 1992).

μSR studies have provided a large amount of information on the behaviour of hydrogen in various systems (see following sections). In diamond two paramagnetic states of muonium have been identified. These are muonium at tetrahedral interstitial sites (Mu_T), and bond-centred muonium (Mu_{BC}), (Patterson, 1988, and refs. therein).

2.6.2 Hydrogen in natural diamond

Hydrogen is a common impurity in natural diamond, with concentrations ranging from 100 to 1100 ppm (by weight), (Sellschop, 1979). Much of this is thought to exist as sub-microscopic droplets (originating from the parental magma), containing water, methane and other hydrogen-containing compounds which were incorporated during the diamond's synthesis in nature (Sellschop, 1987). Theoretical studies have con-

centrated on various hydrogen defects in the lattice itself. Mainwood and Stoneham calculated total-energy surfaces for interstitial molecular and atomic hydrogen (as well as muonium), in both silicon and diamond (Mainwood and Stoneham, 1984). They found that the tetrahedral interstitial site for atomic hydrogen was not lower in energy than other possibilities for both diamond and silicon. They also found atomic hydrogen to be favoured in diamond (albeit by only 0.14 eV), whereas in silicon molecular hydrogen was more stable (by 2 eV)[7]. They did not however discount the possibility of the formation of molecular hydrogen in diamond in conjunction with defect centres or at elevated temperatures.

The discovery of bond-centred muonium led to various calculations on the stability of bond-centred hydrogen, which was then found to be more stable than tetrahedrally sited interstitial hydrogen (Claxton *et al*, 1986, and Estle *et al*, 1987). These calculations were repeated by Briddon and co-workers who calculated the stability of the bond-centred hydrogen as 1.9 eV over the tetrahedral site. In this case the carbon-carbon bond length was increased by 43%, with the hydrogen atom in the middle, 1.1 Å from each carbon atom (Briddon *et al*, 1988). They also studied the case of molecular hydrogen, which was found to be 3.32 eV higher in energy than a bond-centred hydrogen atom with the other hydrogen atom on the corresponding anti-bonding site, the so-called H_2^* complex (Chang and Chadi, 1989). The stability of H_2^* over two separate bond-centred atoms by 1.5 eV also has been shown (Briddon *et al*, 1988, and Mehandru *et al*, 1992). It should be noted that the H_2^* complex has been observed in proton-irradiated silicon (Holbech *et al*, 1993).

The various theoretical studies have been accompanied by both the muonium work and other experimental work on hydrogen detection. Infrared absorption studies show a 3107 cm^{-1} peak attributed to a C-H stretching mode (Woods and Collins, 1983). Nuclear studies of the total hydrogen content have found no correlation between the

[7] In the last few years H_2 in silicon has been the focus of much experimental and theoretical attention (Murakami *et al*, 1996, Leitch *et al*, 1998, and refs. therein)

strength of these absorptions and the total hydrogen concentration, which sheds doubts on the origin of the 3107 cm^{-1} peak (Sellschop *et al*, 1980). C-H stretching mode absorptions are common in CVD diamond and have been correlated to hydrogen content for CVD films with less than 0.2 atomic percent hydrogen (see McNamara Rutledge and Gleason, 1996)[8]. Electron Spin Resonance (ESR) measurements (on proton-implanted synthetic HPHT stones), failed to detect any signals with hydrogenic hyperfine structure, indicating that implanted hydrogen exists in a mostly non-paramagnetic form (Isoya *et al*, 1993).

2.6.3 Hydrogen incorporation during CVD growth

The CVD diamond growth process has many competing mechanisms which lead to the formation of non-diamond carbon and defects. As the growth surface is bathed in hydrogen during growth this inevitably leads to the incorporation of hydrogen into these defects. Of the intrinsic carbon defects in polycrystalline CVD there are two which are of the most importance: grain boundaries and sp^3 defects. Point defects, such as single vacancies and interstitial carbon seem to be rare or non-existent in as-grown CVD material.

Grain boundaries arise from two major mechanisms, twinning and the collision of two separate grains. Twinning on the (111) plane is the most common structural defect seen in a CVD diamond grain. If twinning occurs on multiple, non-parallel (111) planes it can lead to higher order grain boundaries. The growth of polycrystalline CVD begins with the nucleation of diamond growth at a number of sites. When these growing grains collide complex grain boundaries are formed due to the non-alignment of the crystal faces. As these two growth surfaces are both sp^2 bonded and H-terminated it seems likely, from a growth mechanism point of view, that hydrogen traps at these grain

[8]It should be noted that neither free hydrogen atoms nor molecular hydrogen (except if the molecule is in the presence of a local electric field gradient), give rise to absorptions in this C-H stretch region (McNamara Rutledge and Gleason, 1996).

boundaries (Goodwin and Butler, 1997). sp^3 defects arise when partially hydrogen-terminated carbon, not yet bonded to four other carbon neighbours, is buried by the surrounding diamond growth (Butler and Woodin, 1993).

2.6.4 Hydrogen in CVD diamond

The postulated inclusion of hydrogen at grain boundaries and sp^3 defects during growth has prompted many experimental studies into its location and concentrations, both as a tool to further investigate the mechanisms of growth and to determine the effect of hydrogen on the properties of CVD diamond. It must be held in mind that most of the samples used in these studies were prepared under varying conditions using different methods, and thus may have differing concentrations of hydrogen and other defects, varied grain sizes etc. It must also be noted that, when using *ex situ* methods to determine the hydrogen concentration, up to 70% of the bonded hydrogen can be due to water (and other hydrocarbons), absorped onto the surface (Arkhipov *et al*, 1996). Enhanced concentrations of hydrogen on the surface of approximately 10 000 ppm wt. have been reported for natural diamond (Sellschop *et al*, 1980).

McNamara *et al* studied various films using IR absorption and ^1H Nuclear Magnetic Resonance (NMR), (McNamara *et al*, 1992). Concentrations from 0.017 to 0.219 atomic % were measured using this specific NMR technique. These concentrations were found to correlate with optical absorption in the 8 to 10 μm wavelength IR region. They identified two bonding configurations for hydrogen, which were in close spatial proximity (it should be noted that neither of these was the 3107 cm^{-1} line previously mentioned). Segregation of hydrogen into regions of extremely high local hydrogen density was also observed. These were postulated to be grain boundaries, defects, voids or possibly even a heavily hydrogenated phase. Work then followed using Multiple Quantum (MQ) NMR which again indicated a fairly large scale clustering of hydrogen (Levy and Gleason, 1992). MQ NMR has the advantage in that it is able to distinguish between 2-D and 3-D distributions. The hydrogen was found to lie on 2-D sites, which could

be surfaces or grain boundaries.

In films of high hydrogen concentrations (>0.2 at. %), some evidence has been found of the presence of hydrogen, that is involved with sp^2-bonded defects (McNamara *et al*, 1994). Here it was also calculated that hydrogen at grain boundaries alone was not sufficient to explain the total measured hydrogen concentration. This is consistent with thermal conductivity measurements which suggest that the remaining hydrogen is lying on surfaces of internal voids, several microns in dimension (McNamara Rutledge *et al*, 1995).

Hayashi *et al* performed cathodoluminescence (CL) measurements on homo-epitaxial samples which, together with Secondary Ion Mass Spectrometry (SIMS) results, indicate the existence of hydrogen-related gap states in the subsurface region (Hayashi *et al, 1997)*. These results are supported by the observation of hydrogen-related acceptor states in the top 20 nm of CVD films (Looi *et al*, 1998).

A number of EPR measurements have been performed on CVD diamond films (Jia *et al*, 1993, Zhou *et al*, 1996, Talbot-Ponsonby *et al*, 1996, 1998a and 1998b). A centre attributed to hydrogen coupled to a carbon dangling bond has been identified (Jia *et al*, 1993). This centre has been named H1 (Zhou *et al*, 1996). It has been postulated to be a unique defect with a single hydrogen atom $\sim$ 1.9 Å away from the unpaired electron spin (Zhou *et al*, 1996). It was first thought to occur in the diamond bulk (although internal surfaces are a possibility), (Jia *et al*, 1993), with any hydrogen on grain boundaries supposed to be in the form of H_2. Zhou *et al* proposed that H1 occurrs when hydrogen enters a stretched bond at a grain boundary or other extended misfit region (Zhou *et al*, 1996). Other workers found it to be inhomogeneously distributed and that the defects were concentrated in a small fraction of the entire diamond volume (Talbot-Ponsonby, 1996). Further work again indicated H1 to be at grain boundaries or in hydrogenated non-diamond material in between grain boundaries (Talbot-Ponsonby,

1998a). Their Electron-Nuclear Double Resonance (ENDOR) results also indicate that H1 is, in addition to the near-neighbour hydrogen, in an environment with other hydrogen atoms 0.2-1.0 nm away.

A second centre, H2, has also been identified. It is thought to be similar to H1, but with the near-neighbour hydrogen $\sim$ 2.3 Å away (Zhou *et al*, 1996). There is somewhat of a contradiction in the literature regarding H2 in that one group found it only in samples where H1 was absent (Zhou *et al*, 1996), whereas in other work another defect, possibly H2, was found to always accompany H1 (Talbot-Ponsonby, 1998a).

2.6.5 The diffusion of hydrogen

With hydrogen impurities and defects being of such importance in diamond, its dynamics and diffusion characteristics must be of equal importance. It must be borne in mind when studying these that the behaviour of defects in diamond is complex, with multiple trapping, detrapping and diffusion mechanisms at play. This partially explains the discrepancies that exist in studies on hydrogen diffusion thus far.

Interestingly enough, the diffusion of molecular hydrogen was theoretically investigated before that of atomic hydrogen. Early calculations showed that tetrahedral interstitial hydrogen molecules could migrate to other tetrahedral sites via the hexagonal site, with a barrier of only 0.37 eV, compared to 0.95 eV in the case of silicon (Mainwood and Stoneham, 1984).

For the case of atomic hydrogen the barrier diffusion from one tetrahedral site to another was found to be almost certainly too high for diffusion at low temperatures (1.1 eV), (Estreicher *et al*, 1986). The same group also found a barrier of 2.4 eV for diffusion of atomic hydrogen from a tetrahedral to a bond-centred site (Estle *et al*, 1987).

As mentioned previously the most stable form of atomic hydrogen was calculated to be at the bond-centred site. Thus Mehandru, Anderson and co-workers calculated the diffusion barriers for atomic hydrogen, in various charge states, from one bond-centred site to the next. They predicted this to occur along the high-density (110) planes with an activation energy of 1.9 eV (for neutral hydrogen), (Mehandru *et al*, 1992). Positive hydrogen (a proton), was found to be very mobile, with a barrier of only 0.1 eV (Mehandru and Anderson, 1994). This contrasts with negative hydrogen, with a calculated barrier of 2.5 eV. They also looked at the interaction of these hydrogen atoms with common defects, such as vacancies and substitutional nitrogen. The vacancies were found to be traps for diffusing hydrogen, with one vacancy able to accommodate up to four hydrogens with sequentially weaker binding energies (Mehandru *et al*, 1992). The first hydrogen atom was calculated to have a binding energy of 5.3 eV, with each additional hydrogen having a binding energy $\sim$ 1 eV weaker. The hydrogen atom inside the vacancy also reduces the vacancy mobility. In the same paper the mobility of hydrogen in p-type diamond was expected to be increased, analogous to silicon. Substitutional nitrogen was implied to be a hydrogen trap, with a lower limit for hydrogen diffusion from the trap set at 1.49 eV (Mehandru and Anderson, 1994).

Experimental investigations of hydrogen diffusion are relatively recent, with a number of the measurements utilising indirect methods. The first of these was the discovery of low resistivity CVD films which were postulated to be due to the hydrogen passivation of deep traps (Landstrass and Ravi, 1989a). Upon annealing at 873 K for 30 minutes the resistivity was found to increase up to six orders of magnitude, due to the electrical activation of the deep traps, either by dehydrogenation of the films, or by a shift of the hydrogen from an electrically active to an non-electrically active site. These resistivity changes were found to occur at temperatures as low as 100°C. After exposure to a hydrogen plasma at 673 K for four hours the resistivity was once more reduced and the film displayed essentially identical I-V characteristics to the pre-anneal film. This was presumed due to the rehydrogenation of the film. The reverse of this

experiment was also performed on natural type IIa diamond crystals (Landstrass and Ravi, 1989b). Exposure to a hydrogen plasma caused a marked reduction in resistivity, which returned to high values upon annealing.

The discovery of this effect of hydrogen on the electrical properties of diamond led to work, both theoretical and experimental, which dealt with this phenomena. Theoretical calculations of various hydrogen surface configurations showed an enhanced surface conductivity due to hydrogen-induced surface states in the gap (Gavrilenko, 1993). The adsorption of hydrogen removed these states, resulting in a drop in conductivity. This was noted as a possible explanation for the work of Landstrass and Ravi by Gavrilenko as well as Davies, who also hypothesised that plasma-induced surface damage would cause electrical conductivity (Davies, 1994b). A broad CL peak at around 540 nm has been observed in hydrogenated CVD films, which indicated the existence of hydrogen-related gap states in the subsurface region of the as-deposited homo-epitaxial films (Hayashi *et al*, 1997). The presence of high-density hydrogen in the subsurface of these films suggests the presence of hydrogen-induced shallow acceptors in the surface region. Perhaps the most interesting work has been the calculations performed on the stability of interstitial molecular hydrogen in the presence of vacancies and self-interstitials in silicon (Estreicher *et al*, 1998). Vacancies and self-interstitials, both rapid diffusers in diamond, were found to dissociate molecular hydrogen, which was thus found to only be stable in perfect or near-perfect parts of the lattice. It was suggested that the exposure of the material to a hydrogen plasma caused the injection of vacancies which rapidly diffused to the neighbourhood of acceptors. If the sample contained molecular hydrogen this was then dissociated and the resultant atomic hydrogen passivated the acceptors. This was speculated to be a possible explanation for any high values for hydrogen diffusion that have been obtained, as well as the results of Landstrass and Ravi.

In keeping with the upsurge in research on CVD diamond further experimental studies on hydrogen diffusion in CVD diamond have been undertaken. ^{1}H NMR has been used

to track the evolution of the hydrogen signal upon annealing. A change in the number of relaxation centres open to the hydrogen in the sample has been observed (Mitra and Gleason, 1993). It is thought that hydrogen from broken methyl groups in grain boundaries becomes available during annealing to passivate the carbon dangling bonds. Further work showed that a small fraction of hydrogen is mobile at room temperature (McNamara *et al*, 1994). This was proposed to be either a small molecule trapped at a void or a grain boundary, or due to a mobile surface species, such as a methyl group. The stability of ESR signals under annealing was also investigated. The H1 centre was seen to reduce in intensity at ~1500 °C (Jia *et al*, 1993, Zhou *et al*, 1996), indicating that hydrogen was migrating from this centre (or evolution of the centre was occurring). At similar temperatures (1700 K), some of the hydrogen postulated to be on grain boundaries or in inter-granular material was seen to become mobile but was not lost from the sample (Talbot-Ponsonby *et al*, 1998b). Thus there was a redistribution of the hydrogen amongst different bonding configurations. If annealed to 1900 K for four hours in vacuum (no external graphitization was observed), some hydrogen was lost from the sample.

Hydrogen has been shown to be mobile in diamond-like carbon (DLC) films (with a carbon bonding ratio of sp^3/sp^2=70%), (Vainonen *et al*, 1997). A diffusion coefficient of D_H=0.7 nm^2/s at 860 °C was obtained. Diffusion of hydrogen through plasma loading into natural type IIa diamond , measured using SIMS, has been reported (Popovici *et al*, 1995). A value of D_H=24 nm^2/s at 860 °C was measured. Various doubts have been cast on this result. The much higher value obtained for the hydrogen diffusion coefficient in diamond as compared to DLC has been attributed to uncertainties in the sample temperature (Vainonen *et al*, 1997). The authors themselves concluded that the high diffusion rate was influenced by crystal imperfections and this view has been supported by others who noted the fact that type IIa diamonds are known to have a high mosaic spread (Sellschop, 1998, Butler, 1998).

Most recently, work on boron-doped p-type diamond has shown deuterium, in the form of D^+ due to the semiconducting nature of the solid state, to be mobile, with a low effective diffusion activation energy of 0.35 eV (Chevallier *et al*, 1998). The effective diffusion coefficient was found to range from 8×10^{-15} cm^2/s at 508 K to 1×10^{-13} cm^2/s at 753 K, for a boron concentration of 5×10^{19} cm^{-3}. This diffusion was found to be limited by the boron concentration. This work corresponds to the previously mentioned work of Mehandru and Anderson who found the proton to be by far the most mobile form of hydrogen.

Implanted hydrogen has been found to trap deeply in its own range distribution, for high dose implants (Smallman *et al*, 1996). No enhanced trapping rate was found into a pre-damaged layer that was created. This implanted hydrogen distribution was found to be stable under annealing (1473 K, 30 min., argon atmosphere). These measurements utilised Nuclear Resonant Reaction Analysis (NRRA), which measures the entire hydrogen distribution for all bonding configurations. Later ERDA measurements confirmed the lack of enhanced trapping into the pre-damaged layer under identical annealing conditions (Connell *et al*, 1996).

In conclusion hydrogen, easily the most elusive impurity in diamond, has become the focus of much attention. For CVD diamonds it appears to lie on the grain boundaries and other extended defects. Reports of hydrogen diffusion have been made, dependent it seems on the initial state and form of the hydrogen, but clarification of these is needed. Further work on its exact location in the CVD bulk is also required. These are two points addressed in different degrees in this thesis, with a view towards possible complexation with In atoms.

Chapter 3

Theory of Conversion Electron Emission Channeling

3.1 Introduction

The concept of a charged particle *channeling* through a crystal, that is the anisotropic yield of particles transmitted through the crystal, the yield being dependent on the orientation (in relation to the various axes and planes), at which the particle is incident upon the crystal (see Figures 3.1 and 3.2), has been known for a considerable time (Piercy *et al*, 1963). Classically, if one considers a particle entering a crystal in a direction sufficiently close to a major axis, then the particle (let us presume it positive), will suffer a large number of small-angle scattering events that will gently steer it within the crystal "channel". In the case of negative particles the channelled particles will be attracted to and bound to the positive atomic rows or strings. For electrons and other light particles this classical view is replaced by a quantum mechanical framework, in which the electrons (in this case), are treated as Bloch waves and the resultant channeling phenomena are seen as diffraction effects (DeWames and Hall, 1968, and Howie, 1978). The reasons for this are discussed in the following section.

In channeling the measured observable is a yield distribution of particles detected outside the crystal. This distribution is built up from a large number of particles. Thus one uses a statistical basis for treating the classical system (Lindhard, 1965). One considers an ensemble of particles with a uniform transverse momentum distribution. One then applies classical equations of conservation of energy and momentum to describe the modified passage of the particles through the crystal. Upon exiting the crystal the final transverse momentum distribution translates into a distribution of emission angles and thus the yield distribution. A good review of classical channeling can be found in (Gemmell, 1974).

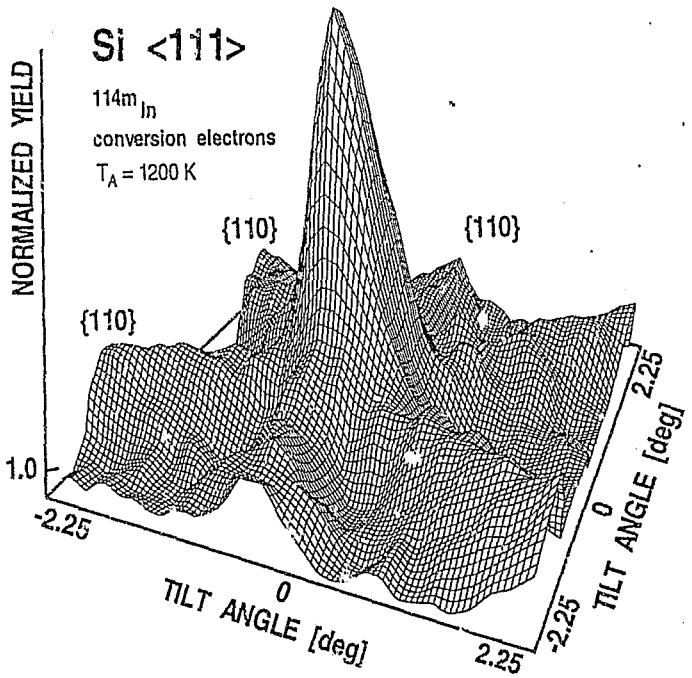

Figure 3.1: Emission channeling pattern of conversion electrons from ^{114m}In in silicon, as a function of tilt angle around the ⟨111⟩ axis (from Hofsäss *et al*, 1994).

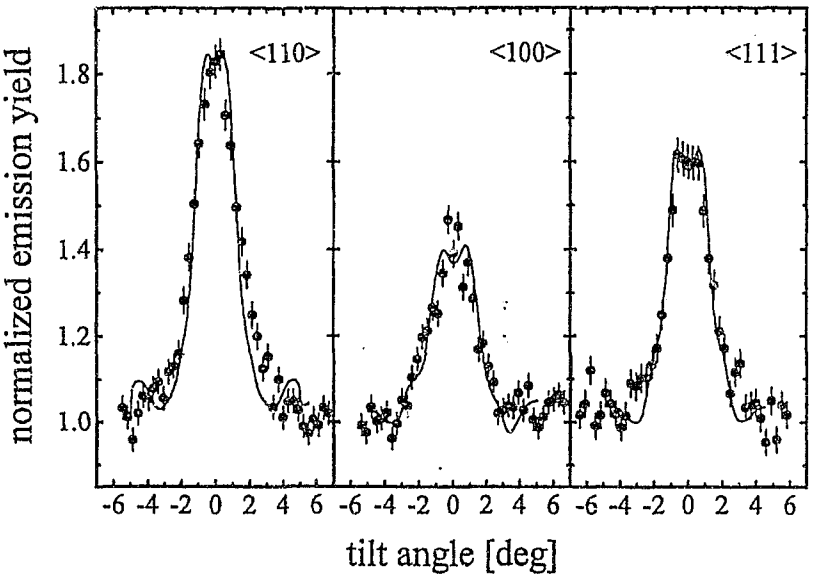

Figure 3.2: Measured emission channeling yields along the ⟨110⟩, ⟨100⟩ and ⟨111⟩ axial directions in diamond for 43 keV electrons from ^{73}As. The solid lines are a theoretical fit (from Hofsäss, 1996).

The Gemmell review focusses on particle beam channeling. This is where the source of channeled particles is located outside of the crystal, in contrast with emission channeling, where the source of particles are radioactive atoms or elementary particles inside the lattice which decay to emit particles which then undergo channeling effects (Hofsäss and Lindner, 1991). An anisotropic yield of these particles is then detected outside of the crystal. A schematic of this technique, showing how the detected variation in channeling yield allows one to distinguish between an emitter located at a substitutional and an interstitial site, is shown in Figure 3.3. This form of channeling has been known for almost as long as particle beam channeling (Domeij and Björkvist, 1965, and Uggerhøj, 1966). Emission channeling has a number of major advantages over the more common ion channeling technique, when studying impurity configurations in

crystals:

- a very low concentration of probe atoms (i.e. impurities), is required, less than 10^{13} atoms/cm^2, which corresponds to typically 10^{17} atoms/cm^3 or 10 ppm
- in the case of electrons with energies below a few hundred keV, due to their low momenta, radiation damage is avoided during analysis
- the number of emitted particles needed for analysis is orders of magnitude less than those in an analysing beam, again vastly reducing radiation damage
- there is, in principle, no restriction on the impurity-host combination used, as charged particle emitters exist for isotopes of almost all elements (see Table 3.1). In fact conversion electron emitters exist for almost all elements in the periodic table. Usually ion channeling, and Rutherford Backscattering Spectrometry (RBS) in particular, are limited to systems with impurities heavier than the host atoms.

The first three of these factors greatly reduces the effects of radiation damage. The low damage due to the radioactive impurity implantation can also sometimes be annealed out before the analysis begins. This allows the study of the effects of thermal annealing on radiation damage.

The basis from which both classical and quantum mechanical treatments of channeling operate is that the individual strings of atoms in an axis are seen as one simple continuous potential. This is the so-called *continuum approximation* of Lindhard (Lindhard, 1965), and is based on the assumption that each channeled particle is negligibly affected by the individual small-angle scatterings it undergoes and that it is only the combined sum of a large number of such events that has an effect. The periodicity of the lattice in the longitudinal direction allows one to then "smear out" the axial potential.

Isotope	Half-life	Emitted particle	Energy	Particles per decay	Production
π^+	26 ns	μ^+	4.12 MeV	1	PSI, LAMPF
μ^+	2.2 μs	e^+	$\approx$ 36.6 MeV	1	PSI
^{8}Li	0.8 s	α	$\approx$ 1.6 MeV	2	ISOLDE
^{32}P	14.3 d	β^-	1.7 MeV	1	Neutron activation
^{73}As	80.3 d	e^-	K 42 keV	0.78	ISOLDE (^{73}Br)
			L 52 keV	0.11	
^{64}Cu	12.7 h	β^+	660 keV	0.19	Neutron activation
		β^-	570 keV	0.40	
^{84}Rb	32.9 d	β^+	1.66 MeV	0.11	ISOLDE
		β^+	780 keV	0.11	
^{86}Rb	18.8 d	β^-	1.77 MeV	0.90	ISOLDE
			680 keV	0.10	
^{107}Cd/	6.5 h	e^-	K 67 keV	0.47	ISOLDE
^{107}Ag			L 89 keV	0.43	
^{110m}Ag	252 d	β^-	87 keV	0.61	Neutron activation
			529 keV	0.36	
^{111m}Cd	48.6 m	e^-	K 125 keV	0.44	ISOLDE
			L 219 keV	0.05	
			I. 247 keV	0.21	
^{115m}Cd	44.8 d	β^-	1.62 MeV	0.97	ISOLDE
^{115}Cd	53.4 h	e^-	K 308 keV	0.41	ISOLDE
			K 332 keV	0.09	
		β^-	580 keV	0.40	
		β^-	1.11 MeV	0.60	
^{111}In	2.83 d	e^-	K 145 keV	0.08	Neutron activation
			K 219 keV	0.05	

Table 3.1: Data of radioactive isotopes and elementary particles suitable as charged particle emitters (from Hofsäss and Lindner, 1991). e^- signifies a conversion electron whereas β^- denotes an electron emitted through beta decay.

Isotope	Half-life	Emitted particle	Energy	Particles per decay	Production
^{112m}In	20.9 m	e^-	K 127 keV	0.68	ISOLDE
			L 152 keV	0.20	
		β^-	670 keV	0.44	
		β^+	1.56 MeV	0.21	
^{114m}In	49.5 d	e^-	K 162 keV	0.44	ISOLDE
			L 186 keV	0.35	
		β^-	1.98 MeV	0.95	
^{118m}In	8.5 s	e^-	K 100 keV	0.6	ISOLDE
^{119m}In	18.0 m	β^-	2.7 MeV	0.95	ISOLDE
^{119}In	2.1 m	β^-	1.6 MeV	1	ISOLDE
^{118}Sb	3.5 m	β^+	2.7 MeV	0.75	ISOLDE (^{118}Xe)
^{118}I	14.3 m	β^+	5.45 MeV	0.54	ISOLDE (^{118}Xe)
^{122}I	3.5 m	β^+	3.1 MeV	0.77	ISOLDE (^{122}Cs)
^{123}I	13.0 h	e^-	K 126 keV	0.14	ISOLDE (^{122}Cs)
^{175}Hf	70 d	e^-	K 26 keV	0.07	Neutron activation
			K 280 keV	0.08	
			K 370 keV	0.03	
^{181}Hf	42.5 d	e^-	K 66 keV	0.16	Neutron activation
			L 122 keV	0.5	
			K 69 keV	0.06	
			K 482 keV	0.02	
		β^-	400 keV	1	
^{133}Xe	5.25 d	e^-	K 45 keV	0.7	fission
		β^-	350 keV	1	
^{175}Yb	4.19 d	β^-	466 keV	0.87	Neutron activation
			353 keV	0.03	
			73 keV	0.10	

Table 3.1: cont.

Isotope	Half-life	Emitted particle	Energy	Particles per decay	Production
^{198}Au	2.7 d	β^-	960 keV	0.99	Neutron activation
^{203}Hg	46.8 d	e^-	K 279 keV	0.13	ISOLDE
		β^-	210 keV	1	
^{212}Bi	60.6 m	α	6.1 MeV	0.36	decay of ^{228}Th
^{212}Po	0.22 μs	α	8.8 MeV	1	daughter ^{212}Bi
^{218}Po	3.1 m	α	6.0 MeV	1	decay of ^{226}Rn
^{214}Po	0.16 ms	α	7.68 MeV	1	daughter ^{218}Po
^{222}Rn	3.8 d	α	5.49 MeV	1	daughter ^{226}Rn

Table 3.1: cont.

3.2 The Dynamical theory of Electron Diffraction

The electrons emitted in emission channeling experiments typically have energies ranging from 100 keV to several MeV. Light particles with these energies have to be treated within a quantum mechanical framework (DeWames and Hall, 1968, and see the discussion in Sørensen and Uggerhøj, 1989). In part this is because the potential acting on the channeled electrons is comparable to their transverse energy (Tamura and Ohtsuki, 1974), and also because the Compton wavelength of such particles is comparable to the lattice spacing of the crystal. A more correct method of determining the quantum mechanical nature of such particles is to determine the number of bound transverse states (Andersen *et al*, 1977). In other words, if only discrete states occur then the motion is quantised and we no longer deal with a classical system. For electrons of a few MeV or less one does indeed have a finite number of such discrete, quantised states (Sørensen and Uggerhøj, 1989). A quantum mechanical theory to describe electron channeling at such energies does exist, based on the dynamical theory of electron diffraction (Howie, 1978). This has been built on the solid theoretical and experimental foundation layed through work on electron diffraction and scattering, especially in electron microscope studies.

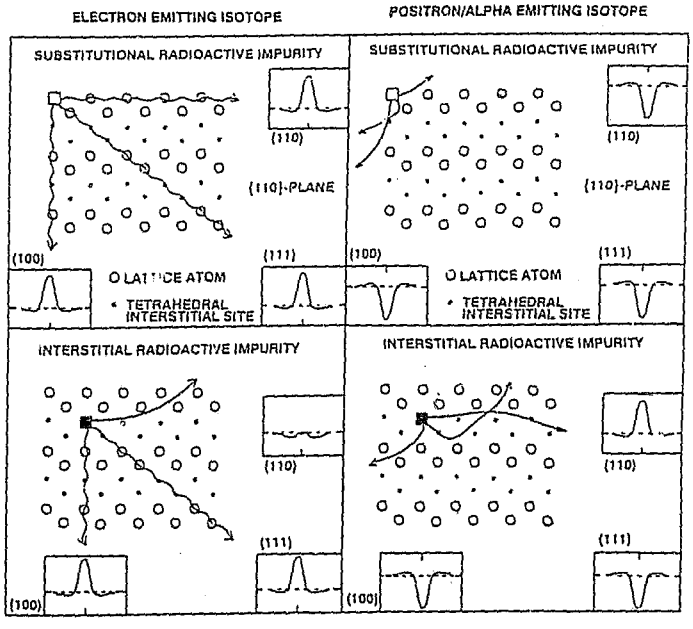

Figure 3.3: Schematic of the emission channeling technique, shown for a (110) plane of the diamond-type lattice, for both electron and positron/alpha emitters (from Hofsäss 1996).

3.2.1 The many-beam formalism

Experimentally what is measured in electron emission channeling is the yield of electrons outside the crystal as a function of angle θ to an axis or plane, emitted from a particular site $(z, \mathbf{r})$ inside the lattice. The Reciprocity Theorem of scattering theory (Lindhard, 1965) states:

The amplitude at B of a wave originating from a source at A, and scattered by P, is equal to the scattered amplitude at A due to the same source placed at B,

which holds generally for electrons elastically scattered in an absorbing medium (Fogany and Turner, 1968). Thus the electron yield outside of the crystal at a point $\mathbf{x}$ originat-

ing from a site $(z, \mathbf{r})$, is equal to the probability of an electron emitted from $\mathbf{x}$ being detected at $(z, \mathbf{r})$. This probability is known as the normalised scattering yield. In the many-beam formalism it is this reverse process that is calculated.

The many-beam formalism was developed by Andersen and co-workers (Andersen *et al*, 1981), and is reviewed by Hofsäss *et al* (Hofsäss *et al*, 1994). We consider relativistic electrons of total energy $E = \sqrt{(\hbar c)^2 k^2 + m_0^2 c^4}$, velocity $v = \hbar k/m$ and relativistic mass $m = m_0.\gamma$, incident upon a crystal nearly parallel to a crystal axis, which we define as the z-axis. Relativistic corrections have been shown to be important for electron energies above 100 keV (Howie, 1978). We ignore spin-dependent terms (Andersen *et al*, 1981), and use the time-independent Klein-Gordon equation,

$$\left((\hbar c)^2 \Delta_{\mathbf{R}} + \left[E - V(\mathbf{R})\right]^2 - m_0^2 c^4\right) \Psi(\mathbf{R}) = 0 \tag{3.1}$$

To a first approximation the motion of the electrons may be separated into a longitudinal component along z, with $k_z \cong k$, and a transverse component in the $x - y$ plane with $k_t \cong k.\theta$, θ being the angle of incidence (Lervig *et al*, 1967). The wave-function under the above-mentioned approximation is thus written as,

$$\Psi(\mathbf{R}) = e^{ikz}.\Psi(\mathbf{r}_\perp) \tag{3.2}$$

with $\mathbf{r}_\perp = (x, y)$. Within the continuum approximation we put $z = vt$[1] and the transverse potential is $V(\mathbf{r}_\perp) = V(\mathbf{r}_\perp, t) = V(\mathbf{r}_\perp)$. A 2-dimensional time-dependent Schrödinger equation is then obtained for the transverse wave-function (Andersen *et al*, 1977)[2],

$$\left[-\frac{\hbar^2}{2m}\Delta_{r_\perp} + V(\mathbf{r}_\perp)\right] \Psi(\mathbf{r}_\perp, t) = i\hbar \frac{\partial}{\partial t} \Psi(\mathbf{r}_\perp, t) \tag{3.3}$$

[1] $v_z \cong v = \frac{\hbar k}{m}$

[2] The fact that the momentum of the electron is almost completely in the forward direction allows us to write $\frac{d^2}{dz^2} \ll 2k\frac{d}{dz}$. We also have $E \gg V$, the energy of the electron being hundreds of keV, whereas the transverse potential is of the order of eV.

This potential is averaged due to thermal vibrations of the lattice atoms. The initial system was treated in a relativistic manner. The transverse momentum of the electrons is however low, due to the forward momentum component being approximately equal to the total momentum. Thus the transverse motion of the electron is non-relativistic. This fact enables the transformation from the Klein-Gordon equation into the Schrödinger equation above. We then use separation of variables (along with putting $\Psi(\mathbf{r}_\perp, t) = \Psi(\mathbf{r}_\perp)e^{iE\hbar/t}$), to obtain a 2-dimensional stationary Schrödinger equation for the transverse motion of the electrons,

$$\left[-\frac{\hbar^2}{2m}\Delta_{r_\perp} + V_{th}(\mathbf{r}_\perp)\right]\Psi(\mathbf{r}_\perp) = E\Psi(\mathbf{r}_\perp) \tag{3.4}$$

where $V_{th}(\mathbf{r}_\perp)$ is the thermally averaged, transverse potential. A convenient method of solving Equation 3.4 is to expand the thermally averaged continuum potential and the wave-functions in a Fourier series. We choose to exploit the periodicity of the lattice in our expansion by using a carefully chosen set of reciprocal lattice vectors (there are many sets), as the k-space points in order to ensure rapid convergence. We obtain

$$V_{th}(\mathbf{r}) = \sum_{nm} V_{nm}^{th} e^{i\mathbf{g}_{nm}\mathbf{r}_\perp} \tag{3.5}$$

for the potential. $\mathbf{g}_{nm} = n\mathbf{g}_1 + m\mathbf{g}_2$ with $\mathbf{g}_1$ and $\mathbf{g}_2$ the reciprocal lattice base vectors corresponding to the distances to the neighbouring axes. The expanded wave-function is

$$\Psi(\mathbf{r}_\perp) = \sum_{\mathbf{k}} C(\mathbf{k})e^{i\mathbf{k}\mathbf{r}_\perp} \tag{3.6}$$

If the wave-vector $\mathbf{k}$ is contained in a wave-function Ψ, then all the other wave-vectors in the Fourier expansion of that wave-function will have the form $\mathbf{k} + \mathbf{G}$, where $\mathbf{G}$ is any reciprocal lattice vector (see for instance Kittel, 1986). Thus Equation 3.6 becomes

$$\begin{aligned}
\Psi(\mathbf{r}_\perp) &= \sum_{\mathbf{G}} C(\mathbf{k}-\mathbf{G})e^{i(\mathbf{k}-\mathbf{G})\mathbf{r}_\perp} \\
&= e^{i\mathbf{k}\mathbf{r}_\perp}\sum_{\mathbf{G}} C(\mathbf{k}-\mathbf{G})e^{-i\mathbf{G}\mathbf{r}_\perp} \\
&= e^{i\mathbf{k}\mathbf{r}_\perp}u_{\mathbf{k}}(\mathbf{r}_\perp)
\end{aligned} \tag{3.7}$$

where $u_k(\mathbf{r}_\perp)$ is a Bloch function. We rewrite the Bloch functions in the notation used in Equation 3.5 as

$$u_k(\mathbf{r}_\perp) = \sum_{nm} C^j_{nm} e^{i\mathbf{g}_{nm}\mathbf{r}_\perp} \tag{3.8}$$

The potentials used in both the work of Hofsäss *et al* (Hofsäss *et al*, 1994), and in our work, were obtained using the Doyle-Turner approximation to atomic potentials determined from Hartree-Fock calculations (Doyle and Turner, 1968), detailed below. In theory any potential can be used (although the proper choice is paramount (Andersen *et al*, 1982a)), and work is underway to include tailor-made molecular potentials in the analysis of diamond electron channeling work (Storbeck, 1999).

The kinematic scattering factor for electrons is given by

$$f_{el}(s) = \frac{8\pi^2 m_0 e}{h^2} \int_0^\infty r^2 \varphi(r) \frac{sin(4\pi sr)}{(4\pi sr)} dr \tag{3.9}$$

where $s = sin\,\theta/\lambda$ Å^{-1} and $\varphi(r)$ is the atomic potential. This can be written in an equation of the form

$$f(s) = \sum_{i=1}^{n} a_i e^{(-b_i s^2)} + c \tag{3.10}$$

where a_i, b_i and c are parameters. Doyle and Turner used relativistic Hartree-Fock calculations to determine the atomic potentials for a large number of atoms and ions. Equation 3.9 above was then used to calculate the kinematic scattering factors. Parametric fits to these, from $sin\,\theta/\lambda = 0.0$ to 2.0 Å^{-1}, were made using equations of type 3.10 above. The resultant parameters have been tabulated (tabulating the atomic potentials for the 67 atoms and ions would be exhaustive). Using the Doyle-Turner approximation the potential is then given by

$$V_{th}(\mathbf{r}_\perp) = \frac{2a_0 e^2}{d} \sum_{i=1}^{4} \frac{a_i}{b_i + 2\rho^2} e^{-\frac{r_\perp^2}{b_i + 2\rho^2}} \tag{3.11}$$

where d is the atomic spacing along the axis, a_o the Bohr radius, ρ is the one-dimensional vibrational amplitude of the lattice atoms and the coefficients a_i and $B_i = 4\pi^2 b_i$ are the aforementioned parameters which have been tabulated by Doyle and Turner (Doyle and Turner, 1968). The corresponding Fourier components of $V_{th}(\mathbf{r}_\perp)$ are now

$$V_{nm}^{th} = 2\pi N a_0 e^2 e^{-\frac{1}{2}\mathrm{g}_{nm}^2\rho^2} \sum_{i=1}^{4} a_i e^{-\frac{1}{4}\mathrm{g}_{nm}^2 b_i} \tag{3.12}$$

where N is the atomic density[3]. The Schrödinger equation is solved numerically giving eigenvectors $u_j(\mathbf{r}_\perp)$ and eigenvalues E_j. An example of a transverse potential for the $\langle 110 \rangle$ axis in diamond with the resultant energy levels for channeled 4 MeV electrons is shown in Figure 3.4

The total wave-function for the transverse motion can then be expanded in terms of the resultant eigenfunctions

$$u(z, \mathbf{r}_\perp) = \sum_j \alpha_j u_j(\mathbf{r}_\perp) e^{-iE_j \frac{z}{\hbar v}} = e^{ik_t \mathbf{r}_\perp} \sum_j \alpha_j e^{-iE_j \frac{z}{\hbar v}} \sum_{nm} C_{nm}^j e^{i\mathrm{g}_{nm}\mathbf{r}_\perp} \tag{3.13}$$

Outside the crystal the electrons are described in terms of a plane wave. Thus at the crystal surface (z=0), the Bloch waves have to equal an incoming (or outgoing) plane wave, that has transverse component $e^{ik_t \mathbf{r}_\perp}$. In order for the transition from crystal to the exterior (or vice-versa) to be smooth, one must also match their first derivatives. Thus the amplitude coefficients in Equation 3.13 are defined and we have

$$\alpha_j = C_{00}^j \tag{3.14}$$

and

$$\sum_j |\alpha_j|^2 = \sum_j |C_{00}^j|^2 = 1 \tag{3.15}$$

[3]In ZnS-type lattices and for the $\langle 110 \rangle$ axis in diamond-type lattices, these Fourier components have to be calculated from a superposition of two different continuum potentials. This leads to the components being modified by phase factors or there being additional imaginary components which result in complex electron wave-functions $\omega_j(\mathbf{r}_\perp)$ (Hofsäss *et al*, 1994)

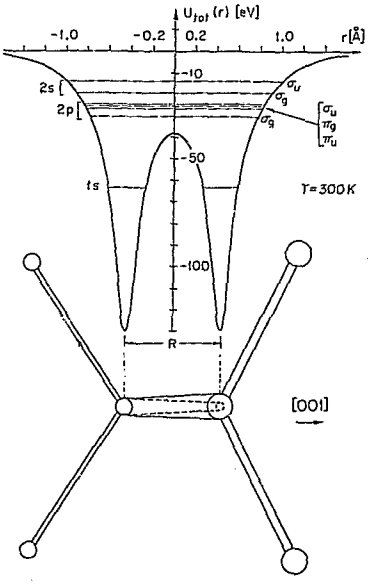

Figure 3.4: Potential and energy levels for 4 MeV electrons channeled along the ⟨110⟩ axis in diamond, with the atomic core and bond configuration in diamond viewed along the <110> direction shown below (from Andersen *et al*, 1982b). This potential exhibits molecular character.

and for any given eigenstate j the initial population is simply $|\alpha_j|^2$.

We can thus determine the normalised scattering yield, that is, the intensity of the Bloch waves at any position $(z, \mathbf{r}_\perp)$ inside the crystal, which result from an incident plane wave with transverse momentum k_t:

$$\begin{aligned} P(z,\mathbf{r}_\perp) &= |u(z,\mathbf{r}_\perp)|^2 \\ &= \sum_i |C_{00}^i|^2.(1-e^{-z/\lambda_i}) \\ &+ \sum_{ij} C_{00}^i C_{00}^j . e^{\frac{z}{2}(1/\lambda_i+1/\lambda_j)} . e^{i(E^i-E^j)\frac{z}{\hbar v}} \times I_{nmn'm'}^{ij} \end{aligned} \tag{3.16}$$

with

$$I^{ij}_{nmn'm'} = \sum_{nm}\sum_{n'm'} C^{i}_{nm} C^{j}_{n'm'} . e^{i(g_{nm}-g_{n'm'})^2 \rho_l^2} . e^{i(g_{nm}-g_{n'm'})r_\perp} \qquad (3.17)$$

As previously mentioned in this section this is the quantity of interest, which equates to the measured yield of particles emitted from sites within the crystal. The thermal vibrations of the impurity atoms at which the scattering occurs cause the position $\mathbf{r}_\perp$ to be folded together with a Gaussian distribution. A Debye-Waller-type factor results (i.e. $\sim e^{-\frac{1}{3}<u^2>G^2}$, where G is a reciprocal lattice vector and $\mathbf{u}(t)$ is the time dependent fluctuation in position of the atom due to thermal vibrations), with one-dimensional thermal vibrational amplitude ρ_1 of the impurity. The normalised scattering yield oscillates as a function of z because of interference between different eigenstates. An example of these oscillations is given in Figure 3.5. The exponential decay of the maximum yield is due to dechanneling, which is discussed in the following section.

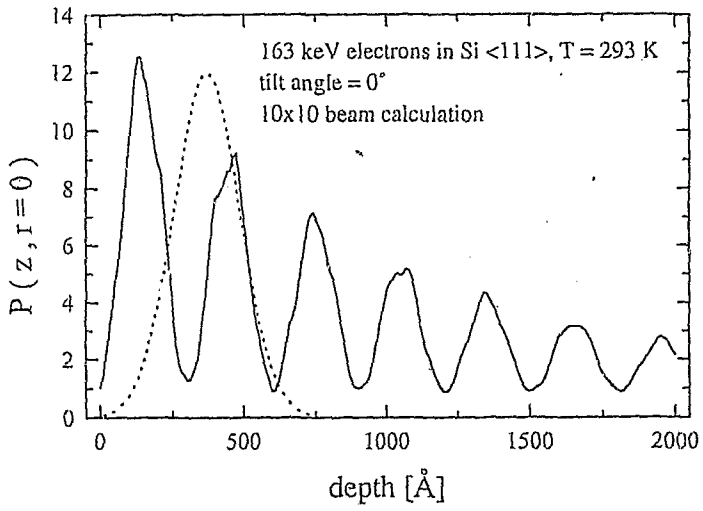

Figure 3.5: Calculated normalised scattering yield of 163 keV electrons incident to the ⟨111⟩ axis in silicon (from Hofsäss *et al*, 1994).

3.2.2 Dechanneling

Dechanneling is the depopulation of previously channeled electrons from the relevant eigenstates. This is due to transitions between eigenstates or just large angle scattering. The three dominant contributions to dechanneling are thermal incoherent scattering (scattering from vibrating lattice atoms that involves large momentum transfer), electronic scattering from lattice electrons and defect scattering. In order to quantify dechanneling we consider a mean free path λ_j, being the exponential decrease in maximum yield seen in Figure 3.5.

For thermal incoherent scattering we consider the scattering of a plane wave off a lattice atom. We obtain the cross-section (Andersen *et al*, 1982a and Andersen *et al*, 1985),

$$\sigma_{inc} = 2\alpha^2\beta^{-2}\pi a_0^2 \int_0^\infty |f(g)|^2(1 - e^{-g^2\rho^2})g\, dg \tag{3.18}$$

where α is the fine structure constant, β=v/c and g is a reciprocal lattice vector. It should be noted that the correlation between neighbouring pairs of atoms is not taken into account in this treatment and thus we underestimate the scattering cross-section by approximately 25-40%, depending on which axis we are dealing with (Andersen *et al*, 1982a). Dechanneling through thermal incoherent scattering increases greatly for heavier matrices due to the quadratic dependence of scattering on atomic number. In the case of diamond it is much less pronounced (Hofsäss *et al*, 1996).

For channeled bound states there is often a concentration of the wave-functions around the atomic string, resulting in an increase in thermal incoherent scattering (Andersen *et al*, 1981). For electrons in the axially localised eigenstates j, this enhancement in incoherent scattering is by a factor of $|u_j(0)|^2_{th}$ - the electron intensity at the string convoluted with a Gaussian representing thermal vibrations of the atoms in the string. For the electrons in eigenstate j we obtain a mean free path for thermal incoherent scattering of

$$\lambda_j = \frac{1}{|u_j(0)|^2_{th} N \sigma_{inc}} \tag{3.19}$$

Thus we have $\lambda_j \propto E$, due to the $1/E$ dependence of the scattering cross-section in Equation 3.18. For the case of diamond this typically has a value of about 500 nm (conversion electron energy taken to be 200 keV and for the deepest bound state), (Hofsäss *et al*, 1994).

The reciprocal mean free path for electronic scattering has been shown to be, for electrons with velocity v incident on an electron gas of uniform density n, (Lervig *et al*, 1967),

$$\frac{1}{\lambda_{el}} = \frac{e^2}{2\hbar v^2}\omega_0 \ln \frac{4mv^2}{\hbar\omega_0} \tag{3.20}$$

where $\omega_0 = \sqrt{4\pi e^2 n/m_0}$ is the plasma frequency, and we have $\lambda_{el} \propto E/\ln E$. If one uses conversion electrons with energies between 100 and 200 keV, one obtains values for the mean free path for electronic scattering of around 100 nm in diamond (Hofsäss *et al*, 1994). The electron states of the transverse motion are however quantized, which leads to a reduction of approximately an order of magnitude in electronic scattering (Andersen *et al*, 1982a, and Andersen *et al*, 1985). Electronic scattering is usually neglected (when compared to thermal incoherent scattering), except in the case of low-Z materials, such as diamond (Hofsäss *et al*, 1994). Obviously electronic scattering is most important compared to thermal incoherent scattering when one is dealing with states with a low intensity at atomic sites.

It is not possible to calculate theoretically a mean free path for defect scattering without knowing *a priori*, the type, lattice sites and concentration of defects in the sample i.e. complete knowledge of the defects in a particular sample. One can however experimentally obtain such a mean free path by implanting emitters at different depths (energies) and observing the resultant yields.

3.3 Features of conversion electron emission channeling

There are a number of particular features exhibited by CEEC, some of which can be utilized to provide unique information about a system:

- structural defects, either in the immediate surroundings of the emitter atom, or in the channels or planes in which channeling occurs, greatly dampen any channeling effects (Hofsäss *et al*, 1992). This can be utilized to observe annealing behaviour in a system of interest

- due to the dominance of thermal incoherent scattering in dechanneling in most materials, electron channeling effects show a strong temperature dependence (Hofsäss *et al*, 1987)

- the dependence of the half-width of channeling peaks or dips on the atomic number of the atoms in the rows along which the electron is being channeled can be used in compound semiconductors to determine which sub-lattice site the emitter occupies (if there is a significant difference in atomic numbers between the different constituents of the compound semiconductor), (Hofsäss *et al*, 1987)[4]

- electron channeling is very sensitive to small displacements from substitutional sites (Hofsäss *et al*, 1984, and Hofsäss *et al*, 1994). This is mostly a result of the electrons lying in the 1s state, which form the major contribution to axial channeling effects. These are highly localised in the atomic string and are thus greatly affected by any small displacement or even thermal vibrations of the emitter atom

- conversion electrons are especially suited to emission channeling because of the well-defined energies of the emitted particles. Knowledge of the exact energies

[4]It has been recently demonstrated that this significant difference in atomic numbers, although helpful, is not a necessary prerequisite for the sub-lattice sensitivity (Wahl *et al*, 1999).

greatly simplifies the theoretical calculations which then do not require a continuum of energies. Background subtraction is also a lot easier

- it should be noted that emission channeling cannot distinguish between small static displacements, of the order of 0.1-0.2 Å, and dynamic displacements due to thermal vibrations (Hofsäss, 1996).

3.3.1 2-D CEEC

Classical channeling effects are most often observed in 1-dimensional "rocking-curves" across a crystal axis, such as that shown in Figure 3.2. Such spectra show an increased amount of information in the 2-dimensional spectra (see Figure 3.1), especially in the case of electrons where quantum mechanical/diffraction effects become important. Thus, in order to gain a complete picture of the observed phenomena, a complete 2-dimensional analysis must be performed. Even in the case of classical channeling, the qualitative and quantitative identification of lattice sites of interest, particularly when several different sites are occupied, is greatly facilitated by the use of complete, 2-dimensional channeling spectra.

There are a number of improvements in using a 2-dimensional detector in 2-D CEEC measurements :

- the measurement time required, with the same information content being obtained, is reduced by approximately two orders of magnitude
- normalisation of each position on the spectrum is no longer required, for neither the activity of the sample nor the beam current received in irradiation experiments
- any errors due to the goniometer precision or reproducibility are eliminated
- the sample no longer needs to be as accurately aligned with the detector, a substantial reduction in the time needed to set up an experiment

- one is able to retain the angular resolution of the system without any accompanying loss in count rate

The CEEC measurements performed as part of this thesis were all made using a 2-dimensional detector, and it is the added information thus obtained that indicates to one the strength of this work.

3.4 Summary

The theoretical background given in this chapter served as an introduction to emission channeling, as well as highlighting its strengths. The reasons for a quantum mechanical treatment of electrons at these energies have been outlined and the more specific *many-beam* formalism has been detailed. This formalism is used in the next chapter to calculate the theoretical yields which are fitted to the experimental data. Of importance to note are Equations 3.12 and 3.13 which give the Fourier expansions of the transverse potential and the transverse wave-function respectively. These, together with the normalised scattering yield given in Equation 3.16, are used in the calculations of the theoretical yields.

The calculations in the next chapter include dechanneling which is also treated in this chapter. Finally the advantages of 2-dimensional CEEC are given to emphasise the benefits that have been gained.

Chapter 4

Conversion Electron Emission Channeling Measurements

4.1 Introduction

The acquisition of 2-dimensional CEEC data, and the resulting geometrical knowledge of the occupied In lattice sites in both pure and impurity-rich diamonds, has been a long sought after goal, for reasons detailed in the introduction. Such work sheds light on the question of complexation of In impurities with various defects, elemental or otherwise. A number of attempts were made at our laboratory to make such measurements using a 2-D silicon surface barrier detector of the type used in the current ERDA measurements (see Section 7.2.3). These attempts were unsuccessful, due to the fact that such detectors, which are based on the principle of resistive charge division, have insufficient position and energy resolution for CEEC measurements, with both resolutions being limited by the noise of the resistive charge division layer itself (Wahl *et al*, 1998). In order to lower the noise present in this layer the detector was cooled to 77 K using a liquid nitrogen cryostat, but this proved fruitless. As a result it was decided to perform the work at the ISOLDE facility at CERN, Switzerland, where a 2-dimensional detector is being specifically utilised for 2-D CEEC measurements (Doyle

et al, 1999).

The ^{111}In decay to ^{111}Cd, shown in Figure 4.1, has conversion electrons of four discrete energies: 144.6, 167.5, 218.6 and 241.6 keV. A conversion electron energy spectrum of this decay, taken during this work, is shown in Figure 4.2. It should be realised that ^{111}In is not an ideal CEEC candidate, due to the fact that the conversion coefficients of the two γ transitions in the decay of the excited daughter nucleus ^{111}Cd are rather low ($\alpha_K \approx 0.086$ (E_γ=171 keV) and $\alpha_K \approx 0.052$ (E_γ=245 keV)). Possible effects due to the physics of the decay process on the results obtained by the CEEC measurements are discussed in Appendix B, and thought to be negligible.

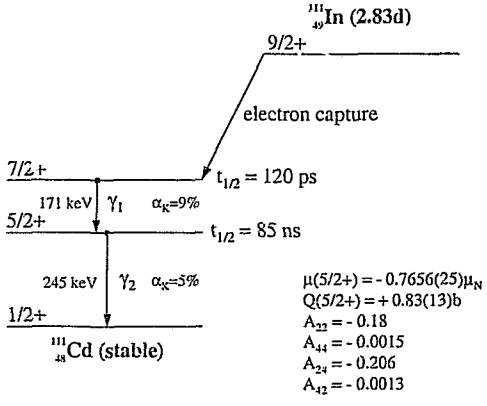

Figure 4.1: The decay scheme of radioactive ^{111}In. On the right the nuclear moments of the intermediate nuclear level and the anisotropy coefficients of the γ-γ cascade are shown. In competition with the γ-rays there is also the emission of K-shell conversion electrons, with probabilities of 8.7% and 5.4% and energies of 145 keV (K 171) and 219 keV (K 245). L-shell conversion electrons are also emitted at energies of 167.5 and 241.6 keV. The full conversion electron spectrum of the ^{111}In decay is shown in Figure 4.2.

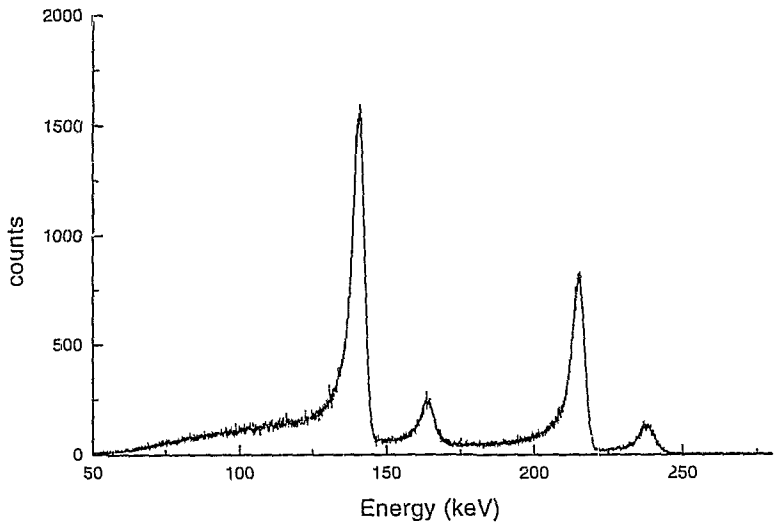

Figure 4.2: Conversion electron energy spectrum for the $^{111}In \rightarrow ^{111}Cd$ decay. This is an uncorrected spectrum so the 5 keV shift due to energy loss in the detector entrance window is visible.

4.2 Experimental method and set-up

4.2.1 Samples

A suite of four natural diamonds was used in these measurements: a pure type IIa stone, a type IIb stone and two pieces from the same type IaAB stone. The IIa stone was polished off-plane, such that the ⟨110⟩ and the ⟨111⟩ axes were both close to the surface normal. The other three stones were all cleaved and then polished as close to the ⟨111⟩ surface as possible. The samples were characterised by IR spectroscopy. The IaAB samples were found to have nitrogen in two forms: A centres > 800 ppm and B centres > 1100 ppm. The IIb sample was found to have a small nitrogen concentration: A centres = 8.3 ppm and B centres = 4.2 ppm. One of the IaAB samples as well as the IIa sample were implanted with 10 keV H ions at a dose of 5×10^{14} atoms/cm^2.

This results in a hydrogen profile which is peaked well beyond that of the In, seen in Figure 4.3. This is due to 10 keV being the lower limit on the energy obtainable from the SRCNS ion implanter. Using the TRIM98 Monte Carlo simulation code (Ziegler *et al*, 1985), the hydrogen concentration at the peak of the In implantation was found to be approximately 14 ppm (atomic), although the concentration varies throughout the In distribution, as seen in Figure 4.3. Thus we had a suite of samples with a large number of various defect configurations, including boron, hydrogen, nitrogen in different complexes, vacancies and extended defects. This allows us to compare the effects of different defects. It should be stressed that we have chosen to study these various defect-rich samples, all with well-characterised defect concentrations, as the only open route in a field where pure samples are not present.

4.2.2 Detector

In order to acquire the 2-D data with the required resolution in both energy and position a sophisticated detector was needed. This was a 22×22 Si pad detector developed at CERN, originally for use in particle physics (Weilhammer *et al*, 1996). The individual pads have an area of 1.3 × 1.3 mm^2, for a total detector size of 30 × 30 mm^2. This detector has a resolution of approximately 5.2 keV at the electron energies of interest, i.e. between 145 and 242 keV, see Figure 4.2. Due to the rather thick detector entrance window the electron energies were shifted approximately 5 keV. This can be seen in the figure. The detector backplane has 15-20 keV noise. This does not however contribute to the resolution but merely restricts the readout trigger of the detector to events of above 35-40 keV. This is perfectly adequate as the conversion electron energies are well above this. The 484 pads are coupled to 4 VLSI pre-amplifier chips, each with 128 channels. The signal from these is fed into a 1 MHz sampling analogue to digital converter (ADC) and then into a digital signal processor. Upon triggering of the detector, due to a signal on the detector backplane above a certain preset threshold, the pads are read out. This is a serial procedure which limits the maximum count rate of the

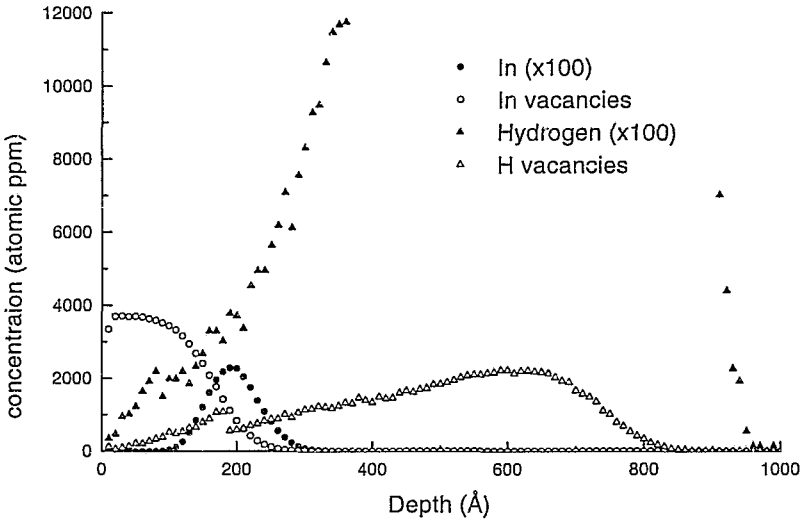

Figure 4.3: TRIM98 Monte Carlo simulations of the resultant indium, hydrogen and vacancy distributions after implantation. The indium dose in the simulation was 3.8×10^{12} atoms/cm^2 and that of the hydrogen was 5.0×10^{14} atoms/cm^2. From approximately 450 to 900 Å the hydrogen distribution extends upwards beyond the range of this plot.

detector to about 400 Hz, which is still suitable for most experiments, as long as the isotope in question has a half-life of more than a few hours.

Of importance in any channeling measurement is the angular resolution of the experimental set-up. For a position-sensitive detector, as in our case, this depends on the position resolution of the detector (which may vary with the energy and type of detected particle), the sample-detector distance and the size and shape of the beam spot projected onto the detector. This projection is defined as the area of the implanted beam spot on the sample (or more correctly, the area from which the detected particles are emitted), projected onto the detector under the angle of detection. If we approximate the position resolution of the detector and the projected beam-spot distribution

as 2-dimensional Gaussians with standard deviations $(\sigma_{det,x}, \sigma_{det,y})$ and $(\sigma_{pbs,x}, \sigma_{pbs,y})$, we then can write the total angular resolution as

$$\sigma_{ang,i} \approx arctan\left(\frac{\sqrt{\sigma_{pbs,i}^2 + \sigma_{det,i}^2}}{s}\right) \tag{4.1}$$

with s the sample-detector distance and i=x,y. For the case of a circular beam-spot one may insert rectangular probability distributions in place of the Gaussians (Wahl and the ISOLDE Collaboration, 1997), that is

$$\sigma_{pbs,i} = \frac{1}{2\sqrt{3}} d_i = 0.289 d_i \tag{4.2}$$

which gives us

$$\sigma_{ang,i} \approx arctan\left(0.289\frac{\sqrt{d_{pbs,i}^2 + d_{det,i}^2}}{s}\right) \tag{4.3}$$

For our system we have $d_{pbs,i} \approx d_{det,i} = 1$ mm which, together with a detector-sample distance of 285 mm, gives us an angular resolution of 0.08^o. In practice the angular resolution is slightly worse, around 0.1^o, due to electron scattering in the detector which degrades the position resolution slightly.

4.2.3 Measurements

All the samples were implanted with 60 keV ^{111}In ions using the on-line mass separator, ISOLDE. Due to constraints on beam-time and current the samples were implanted at various doses. These are tabulated in Table 4.1. The implantations were all performed at room temperature, through a 1 mm collimator. All implantations were made 7 degrees off-axis in order to avoid channeling effects down any major axes or planes. Using TRIM98 the vacancy distribution due to the implanted indium ions was calculated. This is shown in Figure 4.3 along with the implanted In distribution, which is peaked at 188 Å, with a maximum concentration of between 9 and 35 ppm (atomic), depending on the dose. The vacancy concentration at this depth was calculated to be on average for the samples approximately 1150 ppm. This high concentration is due to the fact that each In ion is calculated to create 273 vacancies in the diamond

bulk. This ties in with previous results that found the In to be in implantation-induced defect-rich surroundings (see Table 2.1). Similarly work on implanted ^{181}Hf was found to show a high probability of the probe atom being near a defect (Raudies *et al*, 1983). The samples implanted with hydrogen have an increased vacancy concentration of approximately 1400 ppm at the In peak. This vacancy distribution also extends further into the bulk than that due to the In ions alone.

All the samples were annealed at 1373 K for 20 minutes in a vacuum of 1×10^{-6} Torr, before measuring. This is above the value for the second stage of the In in diamond annealing cycle (see Section 2.4). The exception was the IIb sample which was measured both pre- and post-anneal. Measurements were performed in all major axial directions, apart from the IIa sample where the ⟨100⟩ direction could not be measured due to the sample geometry. The detector-sample distance of 285 mm allowed a channeling pattern of 6×6 degrees to be covered. Each measurement took roughly between eight and twelve hours, depending on the resident sample activity.

4.3 Data analysis

The analysis of this data consisted of three steps, namely the pre-analysis of the experimental data, the theoretical many-beam simulations and the fitting of these simulations to the experimental data. It must be noted here that only the analysis of the IIa and

Sample	^{111}In Dose ($\times 10^{12}$ atoms/cm^2)
IIa	3.63
virgin Ia	5.57
H-implanted Ia	1.59
IIb	6.04

Table 4.1: Implantation doses for the various samples used

the two IaAB samples was part of this work. The analysis of the IIb data was performed by E.J. Storbeck (Storbeck, 1999). All the results are however presented here in order to provide a more complete view of the system.

4.3.1 Pre-analysis of the experimental data

The data files obtained from the detector system allow one to generate an energy spectrum of the signals collected, seen in Figure 4.2. Regions of interest (ROIs), at the four conversion electron peaks were selected and the data was converted into a 2-dimensional format for use by the fitting program FDD. During this conversion the energy spectrum was calibrated. This calibration corrects for the previously mentioned energy shift due to energy loss in the detector window.

Once read into FDD the spectrum was scaled, the entire 2-D spectrum covering a 6×6 degrees solid angle. The collection efficiency of the outermost pads is somewhat reduced, so the outer 2 rows were discarded. In the experimental spectra shown in Figures 4.11 to 4.15 the slightly reduced solid angle can be easily seen. A small number of the pads were also not functioning during our measurements. These were given the average value of the surrounding pads[1]. This unfortunately results in a small loss of information in the measurements. An average value of the sections of the experimental spectrum that are obviously a result of neither axial nor planar channeling was taken and normalised to 1, reflecting the normal yield expected for an emitted particle in a random direction which experiences no significant channeling effects. As a final measure the 20×20 grid (the remainder after removal of the outer pads), was expanded to match the theoretical simulations. The scales of the final displayed plots have been converted back into degrees.

[1]After completion of this work it has been noted that a better method would have been to simply exclude these pads from the fit.

4.3.2 Many-beam calculations

The theoretical simulations were calculated using the dynamical theory of electron diffraction in the many-beam formalism described in Chapter 3, using the program *manybeam*. This code was originally developed at Åarhus, with much further work being done by H. Hofsäss and U. Wahl. Much thanks is due to all the contributors to and developers of this code. The potentials were expanded for $\pm 10 \times \pm 10$ reciprocal lattice vectors, which resulted in 441 Fourier components for the potential and 121 Fourier components for the electron wave-functions. Vibrational amplitudes of both the emitter atoms (^{111}In in diamond) and the host lattice (carbon in diamond) were empirically determined from tabulated Debye-temperatures in the literature (Nielsen *et al*, 1983, and Mayer and Rimini, 1977)[2]. The yield of electrons for ^{111}In emitters inside the lattice were calculated for a number of possible sites[3]. These sites are tabulated in Table 4.2. The yield was determined for a fine angular mesh of points 0.05^o apart. The profiles of the implanted emitters was determined from TRIM98 and folded with the calculated yield. Thus different calculations often had to be performed for one sample, because the emitters were at different depths as seen along different directions.

The *manybeam* program takes into account that all projections of a lattice in a particular axial direction are not the same for all instances of that projection. As an example we consider the bond-centred site. There are six ⟨110⟩ axes in the diamond structure. In three of these the bond-centred site is projected as a bond-centred site. In the other three it is projected as the midpoint of the double atom string. These projections are shown in Figure 4.4. The ⟨111⟩ and ⟨100⟩ projections are also shown. There are four ⟨111⟩ axes, three with the bond-centre projected as bond-centred and one with the bond-centre projected as apparently substitutional. The three ⟨100⟩ axes all have the

[2] $\theta_D(^{111}In) = \theta_D(^{12}C)\sqrt{(12/111)}$, using $\theta_D(^{12}C)$=1860 K.

[3] In the *manybeam* code the Bloch wave Born approximation (BWBA) has recently been implemented. The electronic wave-functions are now treated as Bloch waves, not plane waves. The cross-sections for dechanneling are then calculated from perturbation theory. This results in modifications of Equations 3.18 and 3.19.

Site	Code	Explanation
substitutional	S	
tetrahedral interstitial	T	
anti-bonding	AB	opposite the BC site on the other side of the carbon atom
hexagonal	H	centre of the ⟨110⟩ hexagon
ytterbium	Y	
split ⟨100⟩	SP	
C site	C	has C_{2V} symmetry
substitutional with vibration	S + U_1	S site with 1-dimensional vibrations of the In atom

Table 4.2: Sites calculated for emitters within the diamond lattice. Points at ⟨100⟩ and ⟨111⟩ displacements between these sites in one eighth steps were also calculated.

same projections. This degeneracy in apparent position was accounted for by linearly weighting of the different equivalent positions for each site in each channeling direction considered.

The projections also cause other effects. For instance the substitutional and tetrahedral sites have the same projections in both the ⟨100⟩ and the ⟨111⟩ directions and are thus indistinguishable when observing the emitter in these directions. It is only in the ⟨110⟩ direction that they can be differentiated.

The channeling spectra were calculated for the four energies at which conversion electrons are emitted in the ^{111}In→^{111}Cd decay. The branching ratios for the electrons at 144.6, 167.5, 218.6 and 241.6 keV are 53.43%, 8.01%, 32.5% and 6.05% respectively. The four spectra were folded together (to increase statistics), weighted by their branching ratios and smoothed with a factor of σ=2, which corresponds to an angular reso-

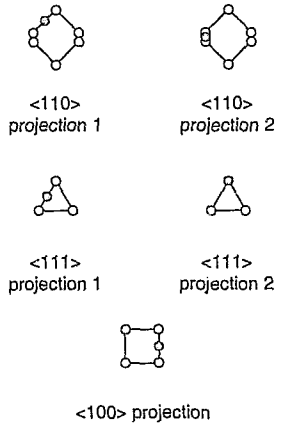

Figure 4.4: The different 2-dimensional projections of a bond-centred site for various axial directions.

lution of 0.1°, as determined earlier in this chapter (σ=angular resolution/resolution of the grid used in the *manybeam* calculations). The effect of the smoothing on the fine structure of the channeling patterns is shown in Figure 4.5. This fine structure is real and is due to diffraction effects. One can even observe where the borders of the Brillouin zone of the 2-dimensional lattice are, due to the fact that the Bragg condition is then fulfilled and one gets abrupt yield changes over a small angular range. This fine structure has also been observed in electron backscattering and transmission experiments. Calculations were performed using a greater number of reciprocal lattice vectors and thus more Fourier components in order to check that the calculations converged to these structures.

It is in the theoretical simulations that the main benefit of using conversion electrons over electrons emitted in β^- decay is derived. The discrete energies with known branching ratios allow a more accurate and simplified calculation than the continuum of energies obtained in β^- decay.

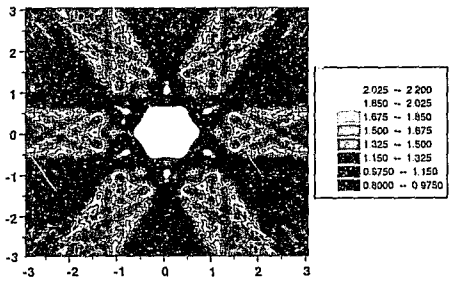

(a) unsmoothed

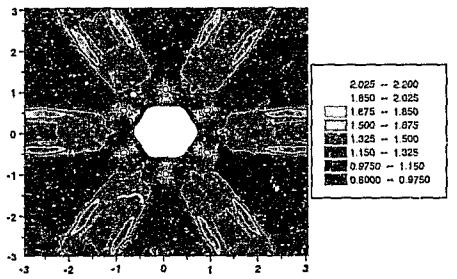

(b) smoothed

Figure 4.5: The effect of smoothing due to angular resolution is clearly shown. This is the calculated pattern for a substitutional emitter along the ⟨111⟩ direction (it should be noted that in this figure and a number of the following CEEC spectra that the x-y scaling of these plots slightly distorts the symmetry due to a square range of angles being displayed by a non-square rectangle).

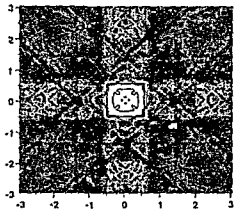

(a) ⟨100⟩

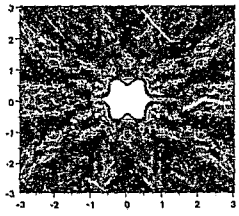

(b) ⟨110⟩

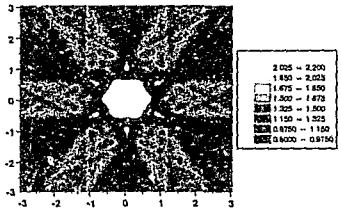

(c) ⟨111⟩

Figure 4.6: Calculated channeling yield for a substitutional emitter, as seen along the three major axial directions.

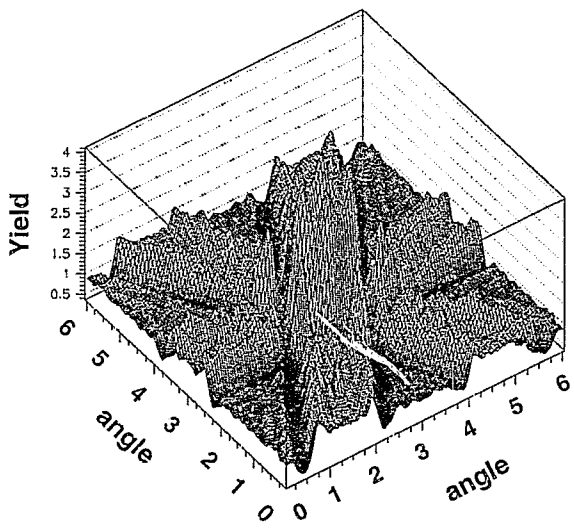

Figure 4.7: 3-dimensional calculated channeling yield from a substitutional or tetrahedral emitter along the $\langle 111 \rangle$ axis. Note the axial channeling peak and the ridges due to planar channeling.

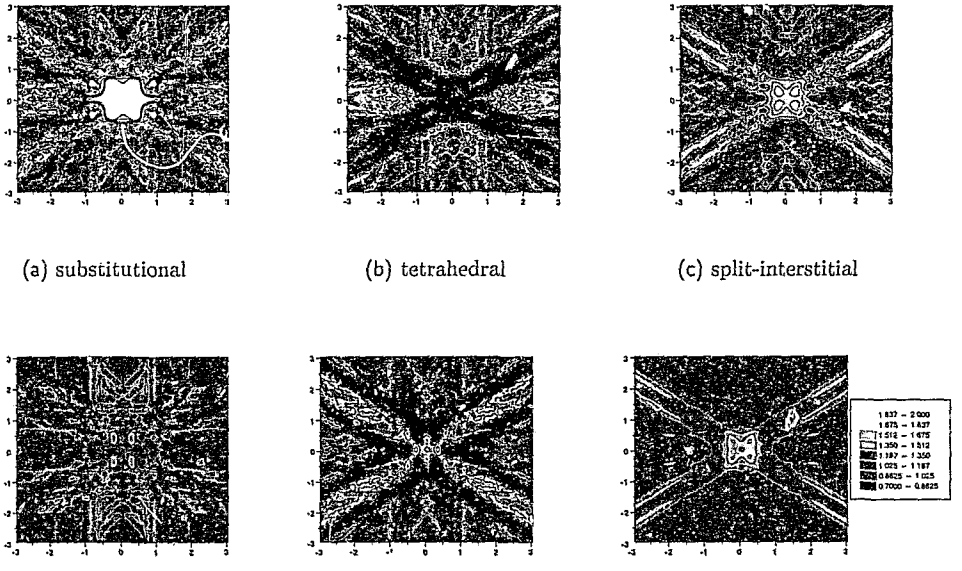

(a) substitutional (b) tetrahedral (c) split-interstitial

(d) C site (e) bond-centred (f) subst. with u1 = 0.4 Å

Figure 4.8: The different channeling patterns obtained for emitters at different lattice sites, as seen down the ⟨110⟩ direction. In (f), u1 is the vibrational amplitude.

A series of calculated channeling patterns is shown in Figures 4.6 to 4.9. Figure 4.6 shows the different spectra which are obtained from one site seen from three different axial directions. These differences arise because the different directions have different atomic spacings along the axes and thus different strength potentials. In Figure 4.7 a 3-dimensional channeling pattern is presented which illustrates both the axial and the planar channeling. The marked differences obtained in the 2-dimensional yield from various sites is shown thereafter in Figure 4.8. Finally the transition from a substitutional to a bond-centred emitter site along the ⟨111⟩ axis seen along the ⟨110⟩ direction is in Figure 4.9. It should be noted that the colour scale used in such plots affects the detail visible. An example of this is Figure 4.10 where the various features within the axial channeling peak are only visible on a certain colour scale. This should be kept in mind in figures with multiple plots, where the choice of scale is not always advantageous for all the constituent plots.

4.3.3 Fitting procedure

The individual sites defined earlier as well as a number of points directly between them were fitted individually for each of the three major directions, to the experimental data. Combinations of the best fits were then made (up to a maximum of three sites), to find the best overall fit, which was determined by a reduced χ^2 value. A number of fitting parameters apart from the site parameters were used. These included a scaling factor, two cartesian and one angular coordinate for both translational and azimuthal orientation. The sites considered in the simulations were substitutional, tetrahedral, bond-centred, anti-bonding, hexagonal, split-interstitial and the C and Y sites. Various points between these along the ⟨111⟩ and ⟨100⟩ directions were also fitted. The expected value for the In vibrational amplitude was 0.034 Å. This parameter was varied for the substitutional site up to a value of 0.400 Å in order to try and improve the fit. In our vibrational model this is equivalent to the In occupying an isotropic distribution around the substitutional site. All parameters were simultaneously optimised using

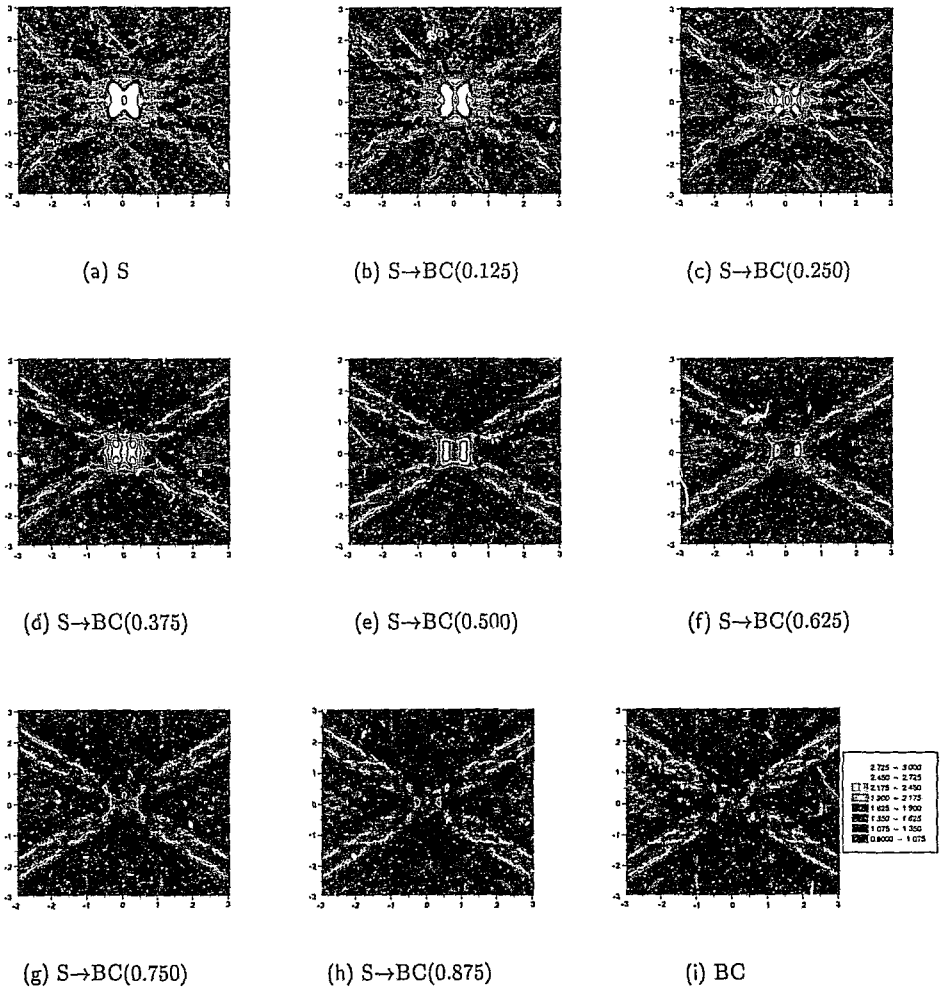

(a) S (b) S→BC(0.125) (c) S→BC(0.250)

(d) S→BC(0.375) (e) S→BC(0.500) (f) S→BC(0.625)

(g) S→BC(0.750) (h) S→BC(0.875) (i) BC

Figure 4.9: The transition in yields obtained for an emitter along various points from S to BC along the ⟨110⟩ direction.

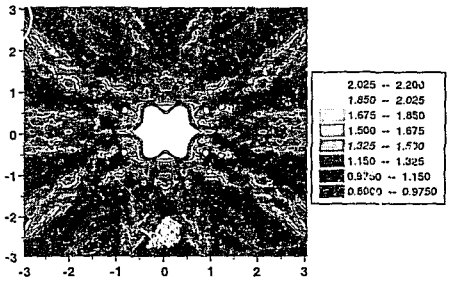

(a)

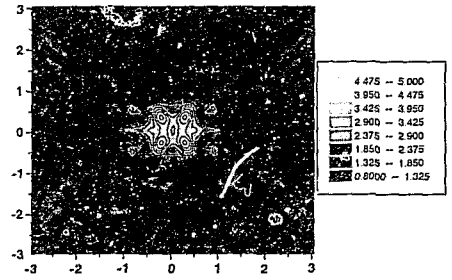

(b)

Figure 4.10: The effect of the maximum and minimum values chosen for the colour scale on the visible features within the axial channeling peak.

non-linear least squares fitting routines. A random fraction due to emitters located on irregular sites (i.e. very low fractions on a number of different sites) or dechanneled electrons, was also included in the fitting procedure. The results were then compared with the other major channeling directions to find the sites occupied and the relevant fractions. The fractions were corrected for background in the energy spectra by fitting a trapezoidal function to the background components under the relevant energy peaks. A trapezoidal function was chosen to account for the tailing in the energy peaks due to incomplete charge collection (or possibly inelastic scattering in the sample), which can be seen in Figure 4.2. This background correction is another advantage of using conversion electrons as opposed to β^- electrons, where the background contribution is not as easily subtracted.

Sample	Substitutional	S →BC (0.6) ⟨111⟩	Random
IIb - pre-anneal	12(10)%	55(10)%	33(8)%
IIb - post-anneal	31(5)%	45(3)%	24(3)%
IIa (hydrogen implanted)	22(8)%	54(17)%	24(8)%
Ia	28(6)%	59(8)%	13(8)%
Ia (hydrogen implanted)	29(4)%	58(4)%	13(9)%

Table 4.3: Fractions obtained for ^{111}In emitters implanted into various diamond samples. The errors for each fraction are given in brackets.

Of the sites attempted and combinations thereof it should be noted that both the tetrahedral interstitial (T) and the bond-centred (BC) sites were attempted in combination with other sites. The reasoning behind this is that these sites often result either in a blocking (below normal yield) or rather homogeneous pattern, and thus could partially substitute for a random fraction. This was found not to be the case.

4.4 Results

The fractions obtained that fitted the experimental data the best are shown in Table 4.3. The most favoured sites were a combination of substitutional and a site approximately 60% of the way from substitutional to bond-centred along the ⟨111⟩ axis (which we shall refer to as S-BC(0.6)). The experimental spectra as well as the best fits to them, using these sites, are shown in Figures 4.11 to 4.15. The theoretical fits are seen to contain a richer structure than the experimental data. Smoothing of the theoretical fits is much more regular than the effect of the angular resolution of the detector. The effect of annealing the sample can clearly be seen in the IIb pre- and post-anneal fractions. After annealing the fraction of emitters on substitutional sites increased as

expected, at the expense of the emitters at both the S-BC(0.6) and the random sites.

The errors are determined by the differences in fractions obtained for a sample from the data acquired using the different channeling directions. Such differences are always present due to errors introduced by the dechanneling approximation in the simulations, errors in the In implantation depth profile in a single crystal, as well as by the imperfect treatment of the angular resolution. Within these errors the fractions obtained are seen to be nearly identical for all samples, independent of defect concentration. This implies not that In-defect complexation with the chosen defects is not occurring, although this now seems more likely, but rather that if it does, it does not affect the In lattice site enough to influence its channeling spectra i.e. the In is displaced less than 0.1 Å. The implications of the data are further discussed in Chapter 8.

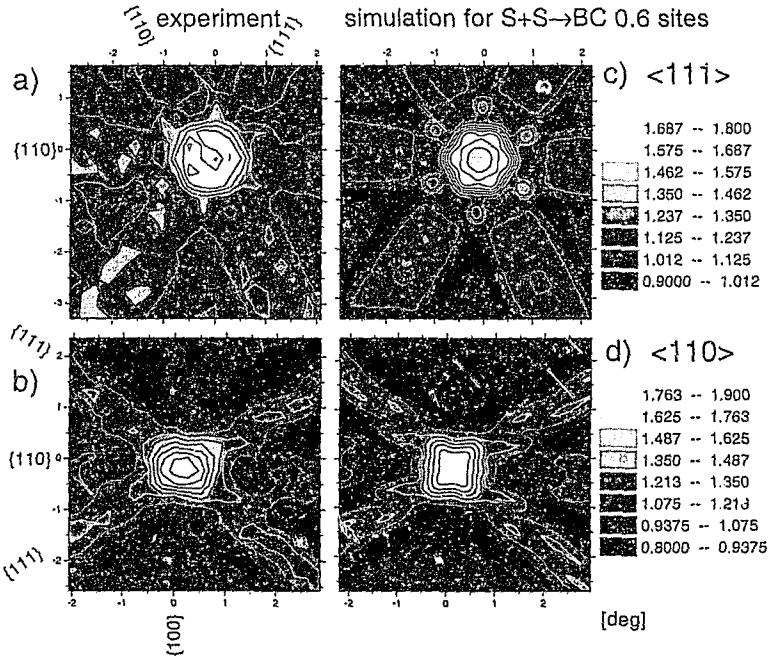

Figure 4.11: Calculated fits to the experimental data for the IIa H-implanted sample in two of the major axial directions, using a combination of substitutional and S-BC(0.6) sites.

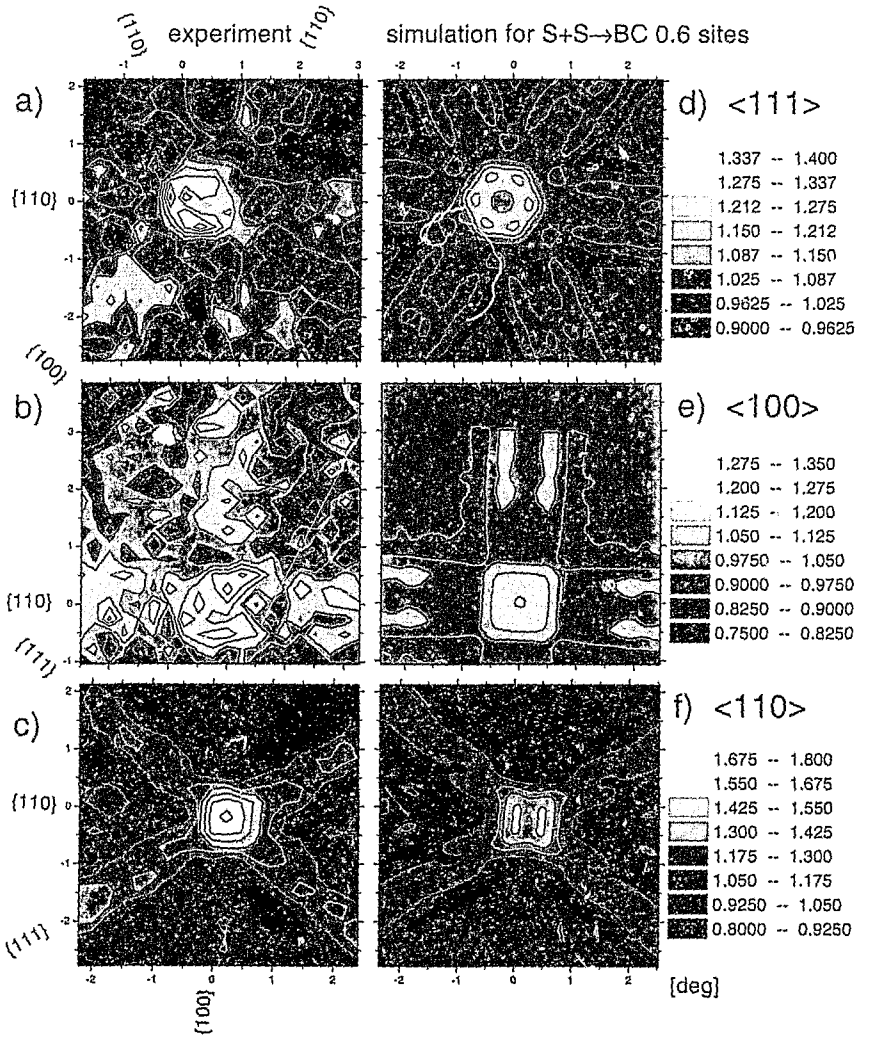

Figure 4.12: Calculated fits to the experimental data for the IIb pre-anneal sample in all three major axial directions, using a combination of substitutional and S-BC(0.6) sites. In (e) the effect of the axis not being centred with the detector is clearly visible in the fit.

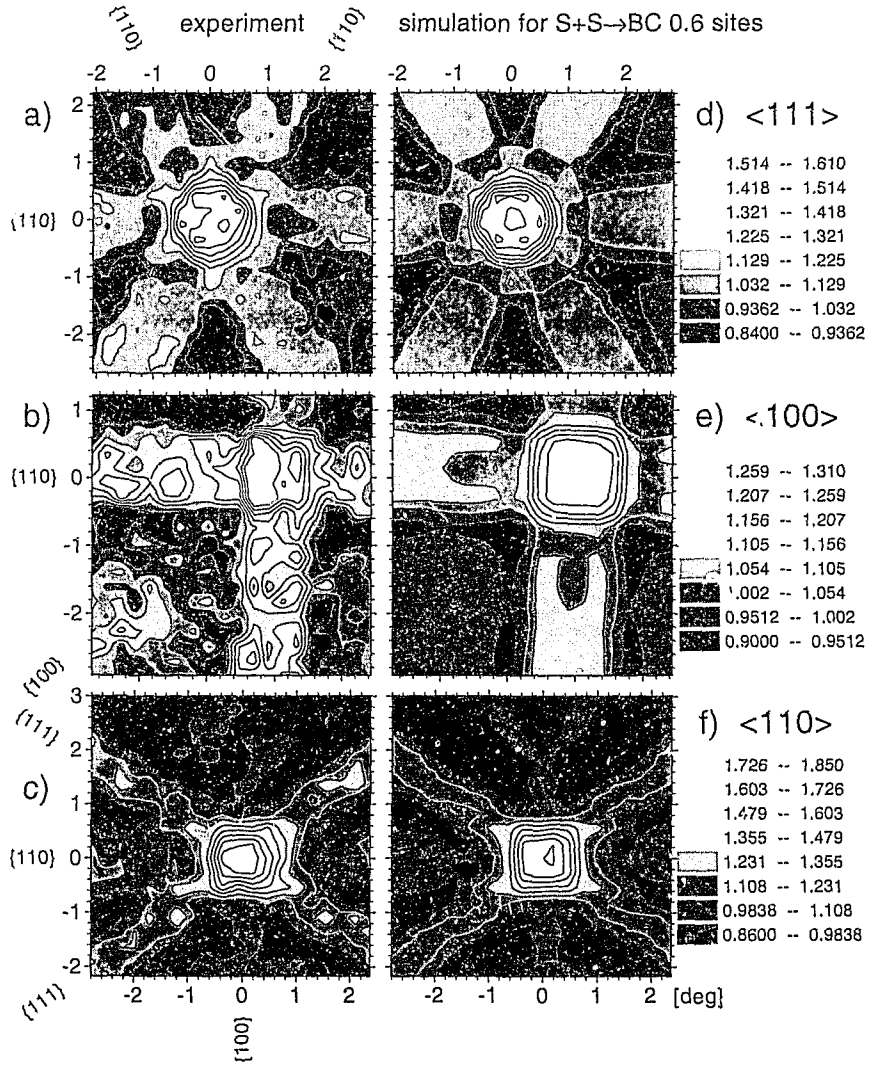

Figure 4.13: Calculated fits to the experimental data for the IIb post-anneal sample in all three major axial directions, using a combination of substitutional and S-BC(0.6) sites.

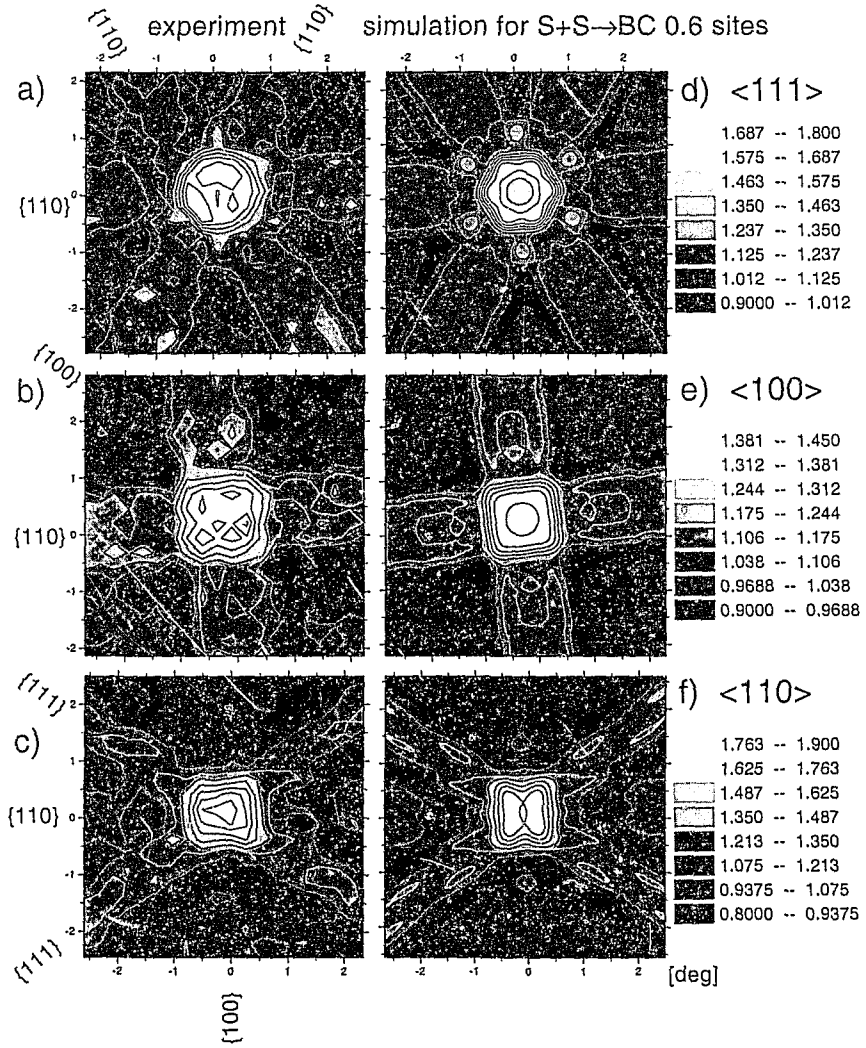

Figure 4.14: Calculated fits to the experimental data for the Ia "virgin" sample in all three major axial directions, using a combination of substitutional and S-BC(0.6) sites.

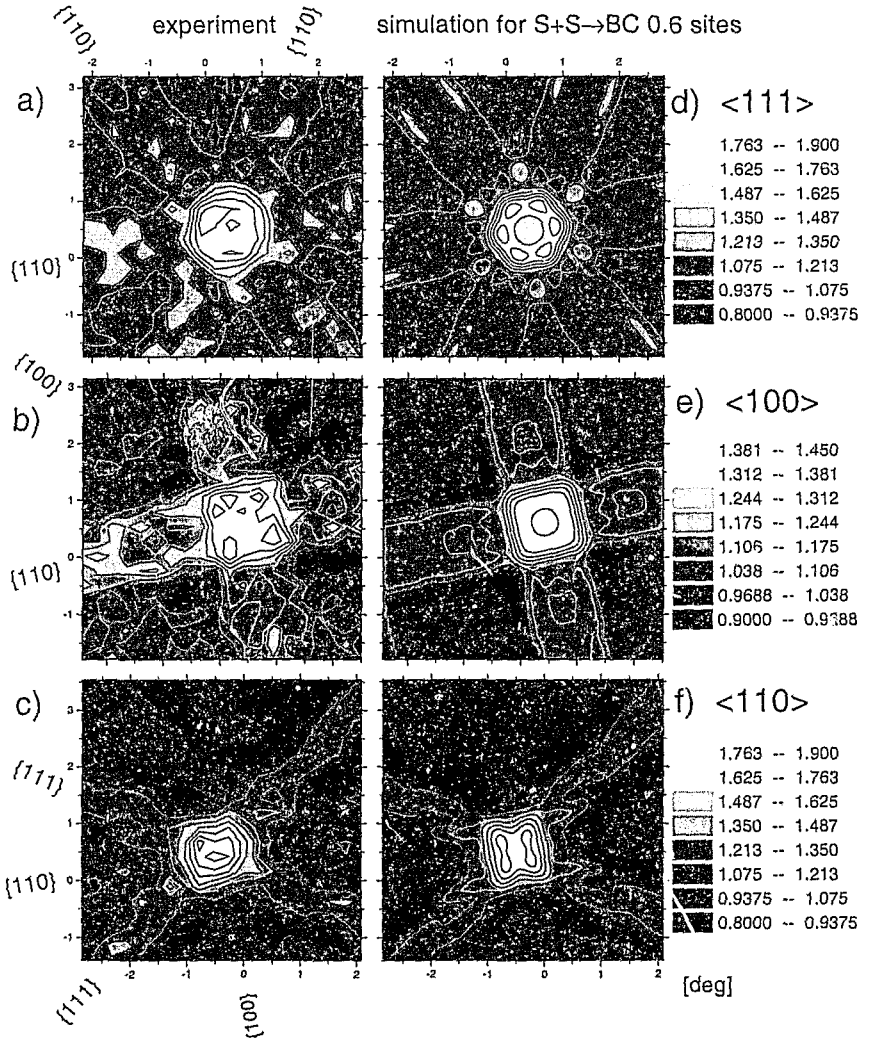

Figure 4.15: Calculated fits to the experimental data for the Ia H-implanted sample in all three major axial directions, using a combination of substitutional and S-BC(0.6) sites.

Chapter 5

Density Functional Theory Calculations

5.1 Introduction

Ever since the discovery of the Schrödinger equation and the realisation of its ability to theoretically predict any system there has been a drive towards the calculation of the parameters of many-body systems. Due to the intractability of the many-body problem mathematically, various approximation methods have been found. An example of these is Hartree-Fock theory. The approximations behind such methods are not however always very good and do not lead always to the correct result, see Jones and Gunnarsson p690 (Jones and Gunnarsson, 1989)[1]. Thus the development of Density Functional Theory (DFT), by Hohenberg and Kohn (Hohenberg and Kohn, 1964), and Kohn and Sham (Kohn and Sham, 1965), which allows one to reduce the calculation of many of the properties[2] of a many-body interacting system of particles *exactly* to

[1]The Hartree-Fock theory does not include correlation effects. This term is better discussed further on in this chapter.

[2]DFT involves loss of information on the phase of the wave-function. Thus properties which depend on the phase cannot be calculated.

the calculation of a number of single-particle equations, was of great importance.

We have used DFT to model various sites for indium in the diamond lattice, to establish the most stable site (Doyle *et al*, 1998). This is a basis for considering molecular complexation of the In atom. The electrostatic potential inside the diamond lattice was then calculated allowing the calculation of the Electric Field Gradient (EFG) sensed by the indium probe atom. This work is the result of a collaborative effort between the Schonland Research Centre and the Solid State Theory group of the University of the Witwatersrand. The computational work was performed by Prof. J.E. Lowther.

5.2 Density Functional Theory

The basic premise of Density Functional Theory is that it is possible to represent exactly some of the ground-state properties of a many-particle system in terms of the ground-state density alone - as functionals of the density (Hohenberg and Kohn, 1964). The total energy of the system can be expressed in terms of these functionals, and this energy satisfies a variational principle. This was carried further by Kohn and Sham (Kohn and Sham, 1965), whose equations allow one to map an interacting many-particle system onto a system of non-interacting particles moving in a potential due to all the other particles.

It should be noted that the majority of electronic structure calculations operate in the framework of the Born-Oppenheimer approximation (Born and Oppenheimer, 1927). Due to the large mass difference between the electrons and the nuclei, the electrons respond essentially instantaneously to any motion of the nuclei. This allows one to separate the electronic from the nuclear coordinates, resulting in a system of electrons moving within a "frozen" nuclear configuration.

The derivation of the basic theorems of the density functional formalism developed by Hohenberg and Kohn, and Kohn and Sham were later generalised by Percus (Percus,

1978), and Levy (Levy, 1979). If we consider an N electron system moving in an external potential $V_{ext}(r)$, then the Hamiltonian is

$$H = T + V_{ee} + \sum_{i=1}^{N} V_{ext}(r_i) \tag{5.1}$$

where T is the kinetic and V_{ee} is the electron-electron interaction operator. We define the functional

$$F[n] = \min_{|\psi|^2 \to n} \langle \psi | T + V_{ee} | \psi \rangle \tag{5.2}$$

for all "N-representable" densities, $n(r)$, those which can be obtained from some antisymmetric wave-function, $\psi(r_1, r_2, ..., r_N)$. We take the minimum over all ψ that give the density n. If we denote E_{GS}, ψ_{GS} and $n_{GS}(r)$ to be the ground-state energy, wave-function and density respectively then the two basic theorems of DFT are

$$E[n] \equiv \int dr V_{ext}(r) n(r) + F[n] \geq E_{GS} \tag{5.3}$$

for all N-representable $n(r)$, and

$$\int dr V_{ext}(r) n_{GS}(r) + F[n_{GS}] = E_{GS} \tag{5.4}$$

These are given here without proof. For a basic proof of these theorems see Jones and Gunnarsson (Jones and Gunnarsson, 1989). Equation (5.3) is the energy of the system as a functional of the density, obeying a variational principle with respect to the ground-state energy. Equation (5.4) shows that (5.3) will give the ground state energy if the ground state density is used. Both of these equations are to be used with the proviso that the external potential is known.

5.2.1 Exchange and correlation energy contributions

Due to the fact that electrons are fermions and thus obey Fermi-Dirac statistics, the wave-function of a many-electron system must be antisymmetric under exchange of any two electrons. This antisymmetry produces a spatial separation of same spin electrons

and thus reduces the total Coulomb energy of the system. This reduction of energy of the system due to the antisymmetry of the wave-function is known as the *exchange energy*, and a total-energy calculation containing this is the Hartree-Fock approximation.

The Coulomb energy can be again reduced if one also separates electrons of opposite spin. This is however at the cost of having to increase the kinetic energy of the system. The difference between the total energy of this system and one calculated using the Hartree-Fock approximation, is known as the *correlation energy*.

We have written the ground-state energy in terms of the density of the electron system, (see equation 5.4). The functional $F[n]$ is however still not known. We rewrite the total energy of the system as

$$E[n] = T_0[n] + \int d\mathbf{r} n(\mathbf{r})[V_{ext}(\mathbf{r}) + \frac{1}{2}\Phi(\mathbf{r})] + E_{XC}[n] \tag{5.5}$$

where $T_0[n]$ is the kinetic energy of a non-interacting system with density n, Φ is the classical Coulomb potential due to the electrons and $E_{XC}[n]$ is the exchange-correlation energy (and can actually be seen as one way of defining it). The use of $T_0[n]$ (which neglects interaction terms in calculation of the kinetic energy), is justified due to its comparable magnitude to the true kinetic energy, and can be corrected for (see for example, (von Barth, 1992)). This separation is due to Kohn and Sham (Kohn and Sham, 1965), and it divides the energy into a number of terms which can be calculated exactly (single particle terms) and the exchange-correlation term (many-body), which must be approximated.

5.2.2 The Local Density Approximation

As mentioned above DFT still requires an approximate method to describe the exchange-correlation energy as a function of the electron density, (if one knew the exchange-correlation energy functional exactly, then one could generate the exact exchange-correlation potential by taking the functional derivate with respect to the density).

The simplest method to do this is the local-density approximation (LDA), developed by Kohn and Sham (Kohn and Sham, 1965). The LDA assumes that the exchange-correlation energy per electron at a point r in the electron gas being studied, $\epsilon_{XC}(r)$, is equal to the exchange-correlation energy per electron in a homogeneous electron gas that has t' ' same density as the electron gas at point r, i.e.

$$E_{XC}[n(r)] = \int \epsilon_{XC}(r) n(r) d^3r \tag{5.6}$$

and

$$\frac{\delta E_{XC}[n(r)]}{\delta n(r)} = \frac{\delta[n(r)\epsilon_{XC}(r)]}{\delta n(r)} \tag{5.7}$$

with

$$\epsilon_{XC}(r) = \epsilon_{XC}^{hom}[n(r)] \tag{5.8}$$

Thus the LDA assumes that the exchange-correlation functional is purely local, ignoring corrections to the exchange-correlation due to nearby inhomogeneities in the electron density. Surprisingly, this approximation turns out to be a relatively good one for a large number of systems and is, for instance, the most common one used in total-energy pseudopotential calculations.

It should be noted that a number of improvements to the LDA exist. Among these is the generalised gradient approximation (GGA). In the GGA not only the electron density at various points in the system is taken into account, but the gradient in the electron density between them is also considered. For various parametrisations of this see for instance Perdew and Wang 1992, and Perdew *et al*, 1996.

5.3 Periodic systems

Despite the elegant formalism and approximations of the preceding section, we remain with the task of solving a system of an infinite number of non-interacting electrons

moving in a potential generated by an infinite number of ions. This is complicated by the fact that the basis set used to describe a wave-function extending over the whole solid is also infinite.

We solve this by applying Bloch's theorem and utilising a number of judicious approximations. Bloch's theorem has already been discussed in the many-beam formalism in Chapter 3. A slightly alternative derivation is given here for completeness.

5.3.1 Bloch's theorem

Bloch's theorem can be written as (see Kittel, 1986, p163),
The eigenfunctions of the wave equation for a periodic potential are the product of a plane wave $e^{i\mathbf{k}.\mathbf{r}}$ *times a function* $u_{\mathbf{k}}(\mathbf{r})$ *with the periodicity of the crystal lattice.*
or,

$$\psi_i(\mathbf{r}) = e^{i\mathbf{k}.\mathbf{r}} u_{\mathbf{k}}(\mathbf{r}) \tag{5.9}$$

We then expand the cell-periodic part of the wave-function using a basis set of discrete plane waves whose wave vectors are reciprocal lattice vectors of the crystal in question (this ensures rapid convergence),

$$u_{\mathbf{k}}(\mathbf{r}) = \sum_{\mathbf{G}} c_{i,\mathbf{G}} e^{i\mathbf{k}.\mathbf{r}} \tag{5.10}$$

where we have defined the reciprocal lattice vectors $\mathbf{G}$ by $\mathbf{G}.\mathbf{l} = 2\pi m$ for all $\mathbf{l}$ where $\mathbf{l}$ is a lattice vector of the crystal and m is integer. We then can write the electronic wave-functions as a sum of plane waves,

$$\psi_i(\mathbf{r}) = \sum_{\mathbf{G}} c_{i,\mathbf{k}+\mathbf{G}} e^{i(\mathbf{k}+\mathbf{G}).\mathbf{r}} \tag{5.11}$$

5.3.2 k-point sampling

Due to the boundary conditions that apply to a bulk solid, electronic states are only allowed at a set of $\mathbf{k}$ points in the solid. The density of these $\mathbf{k}$ points is proportional

to the volume of the solid. The infinite number of electrons in the solid is accounted for by having an infinite number of k points, with only a finite number of electronic states at each k point. Due to Bloch's theorem we now have a discrete plane wave expansion for each of these electronic states.

Wave-functions at k points that lie close to each other have very similar values, so it is possible to approximate the k points in a region by a single k point. Thus one only has to calculate the electronic states for a finite number of k points in a solid. Obviously one has to choose the correct set of k points in order to obtain an accurate approximation for the electronic potential in the solid. A number of methods have been devised to do this using specific sets of k points in the Brillouin zone (see for example, Evarestov and Smirnov, 1983). One can always test the accuracy of any k point sampling by extending the number of k points and checking for convergence of the electronic potential and energy of the system.

5.3.3 Plane wave basis sets

Although Bloch's theorem reduces the problem of calculating each electronic state to that of a discrete plane wave basis set, this set is still, in principle, infinite. However, the coefficients $c_{i,\mathbf{k}+\mathbf{G}}$ (see equation 5.11), for those plane waves with small kinetic energy $(\hbar^2/2m)|\mathbf{k}+\mathbf{G}|^2$ are typically more important than those with large kinetic energy. One can thus truncate the plane wave basis set below some particular cut-off energy, resulting in a finite basis set. As in k point sampling it is possible to check the validity of the approximation by increasing the cut-off energy to see how convergence is affected.

5.3.4 Supercells for non-periodic systems

One can however not apply the Bloch theorem to any system that contains a defect. The symmetry of such a system is broken. In such cases a continuous plane wave basis

set is chosen[3]. Thus this basis set once again contains an infinite number of states. This situation is overcome by the use of periodic supercells. Such a supercell for the calculation of a single point defect is shown schematically in Figure 5.1.

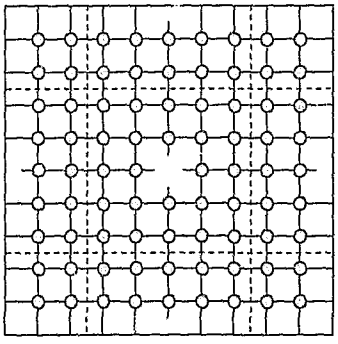

Figure 5.1: Schematic illustration of a supercell for a point defect (in this case a vacancy), in a bulk solid. The supercell is the area enclosed by the dashed lines, (from Payne *et al*, 1992).

This supercell contains the defect surrounded by a region of bulk crystal. One applies periodic boundary conditions to the supercell such that it is reproduced throughout space. This is indicated in Figure 5.1 by the dashed lines. Enough bulk crystal is included so as to avoid the defects in neighbouring cells from interacting appreciably with each other. This can be tested by computing the total energy of the system while increasing the volume of the cell. Once convergence is reached it can be assumed that there is no interaction between neighbouring defects. It should be noted that calculations involving surfaces or molecules also utilise the supercell method.

[3]Any complete set can be used.

5.4 Pseudopotential theory

So far we have concentrated on using a plane wave basis set to expand the electronic wave-functions. This is not well suited to dealing with the electronic wave-functions in the core region near the nucleus. This is due to the extremely large basis set that is needed to expand the tightly bound core orbitals and to follow the rapid oscillations of the valence electron wave-functions in this region. In order to reduce the number of plane wave basis states the *pseudopotential approximation* is used (Phillips, 1958, Cohen and Heine, 1970, and Yin and Cohen, 1982).

The basis of this approximation is that the core wave-functions of an atom are essentially independent of the environment that the atom is in. The importance of these electrons in determining the majority of the physical properties of the solid is substantially less than that of the valence electrons, their major contribution being to enforce the orthogonality of the valence wave-functions to the core states. This serves as a justification for replacing the potential due to the ion core and the core electrons with a much weaker *pseudopotential*, that effectively reproduces the effects of the core electrons/ion core potential. This can be seen schematically in Figure 5.2 where an ionic potential, a valence wave-function and the corresponding pseudopotential and pseudo-wave-function are shown, where r_c is the radius at which the all-electron and the pseudopotential values match. r_c ranges typically from one to two times the value of the core radius.

5.4.1 Properties of pseudopotentials

The phase-shifts due to and scattering properties of the ion core are angular momentum dependent. The pseudopotential must also have this dependency, the most general form being,

$$V_{NL} = \sum_{lm} |lm\rangle V_l \langle lm| \tag{5.12}$$

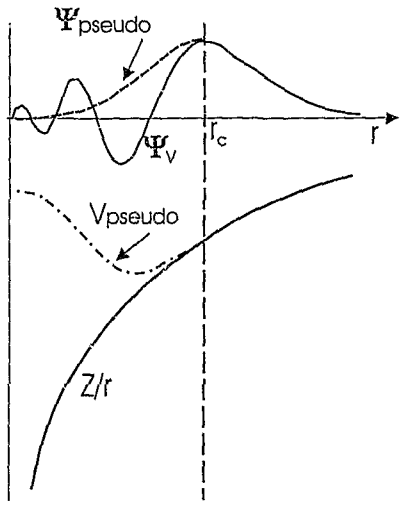

Figure 5.2: Schematic illustration of all-electron (solid lines) and pseudoelectron (dashed lines) potentials and their corresponding wave-functions, also showing the relevance of r_c, (from Payne et al, 1992).

where $|lm\rangle$ are the spherical harmonics and V_l is the pseudopotential for angular momentum l. A pseudopotential that uses the same potential for all angular momentum components of the wave-function, i.e. $V_l = V$, is known as a local pseudopotential and is only a function of the distance from the nucleus.

A match of the pseudo- and "real" wave-functions outside the core region insures that the first-order energy dependence of the scattering is correct, allowing it to be well described over a wide range of energies. If one constructs a pseudopotential that corrects for higher-order terms then these are termed *ab initio* or *norm-conserving*. Such pseudopotentials are able to describe scattering in a wide range of atomic environments, which is known as *transferability*. It should be noted that, in general, the smaller the value of r_c, the more transferable the potential.

A number of corrections and constraints have been used to improve the rapid con-

vergence of the total energy calculated in a system generated using pseudopotentials. We call pseudopotentials with this property *smooth*, (see for example, Troullier and Martins, 1991).

5.5 Ion-ion interactions

Although DFT deals efficiently with the electronic system, one still has to deal with the ion-ion interactions in order to completely describe the system. Due to the fact the Coulomb interaction is long ranged it is very difficult to compute the Coulomb energy of the pure ionic system using a direct summation in real space. The same applies to reciprocal space as the Coulomb interaction is again long ranged. One uses the Ewald method (see Kittel, 1986, p604-608), which is a rapidly convergent method for Coulombic summations in periodic lattices.

5.6 Calculations

Ab initio plane wave pseudopotential local density theory as implemented through a combination of the FHI94 and FHI96 code (Fritz Haber Institute, Berlin), was used to model various sites for In in the diamond lattice. A plane wave smooth pseudopotential approach was used throughout, as in Troullier and Martins for the C pseudopotentials (Troullier and Martins, 1991), and as in Fu and Zunger for the In pseudopotential (Fu and Zunger, 1997). The In based defect was placed within a 64 atom supercell. The cut-off radius for the plane waves was 64 Ry, which was necessary for good convergence (Li and Lowther, 1996). One **k** point was used within a local density procedure (as in Ceperley and Alder, 1980, and Perdew and Zunger, 1981), namely **k**=0, the reason for this being the computational time taken for more points was large. This included a self-interaction correction as devised by Perdew and Zunger. Spin polarisation effects were not included.

We defined the formation energy of the system as,

$$E_f = E_{C_nIn} - \frac{n}{n+1}E^0_C - \frac{1}{n+1}E^0_{In} \tag{5.13}$$

where E_{C_nIn} is the total energy per atom of the supercell and E^0_C and E^0_{In} are the energies of the carbon and indium pseudo-atoms respectively. We similarly define the defect binding energy as,

$$E_b = E_{C_nIn} - \frac{n}{n+1}E^0_{diamond} - \frac{1}{n+1}E^0_{In} \tag{5.14}$$

where $E^0_{diamond}$ is the energy of the 64-atom supercell. Thus E_b shows the relative defect stability in the lattice structure. The accuracy in our values was conservatively estimated to be approximately ± 0.025 eV. Lattice relaxation was included in the calculation using a standard self-consistent gradient technique. This was to allow realistic results.

5.7 Results

At first we considered two simple defects, namely simple substitutional and bond-centered In. As expected the formation energies for these defects turned out to be quite high (~9 eV). This correlates with earlier theoretical work on various extrinsic defects in diamond where values of 10.4 eV, 5.5 eV and 15.3 eV were found for substitutional phosphorus and tetrahedral lithium and sodium respectively (Bernholc *et al*, 1992). There was extensive relaxation in the case of the bond-centred In, its final position being between two vacant lattice sites along a <111> orientation. The two carbon atoms thus displaced, were each located in separate interstitial positions. The final relaxed structure is shown in Figure 5.3. The binding energies of the substitutional and bond-centred sites although small, were positive, indicating that the probability of these defects existing in a stable state is low.

In order to facilitate the relaxation of the In-diamond system and to provide stability for the resulting highly relaxed configuration we introduced a neutral vacancy (V_C)

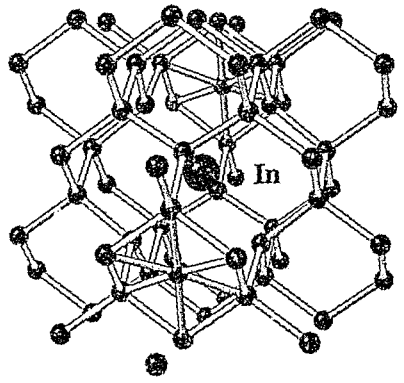

Figure 5.3: Metastable <111> In defect on a bond-centred position as viewed slightly away from the <110> channeling direction. The two adjacent C interstitial atoms are also shown.

into the system. As a starting configuration we placed the vacancy on an adjacent site to the substitutional In. Under relaxation the In atom moved off centre, leaving a V_C-In-V_C defect orientated along the <111> direction. The calculation was repeated with a different starting configuration, the In being situated bond-centred midway between two C vacancies. The final structure in both calculations was independent of the starting configuration. It is shown in Figure 5.4.

We also relaxed the system with In bond-centred between two vacancies in the <100> direction. This underwent (as again expected), large relaxation, but the resultant system had a significantly larger binding energy (positive).

All the calculated formation and binding energies of the various defects that we have

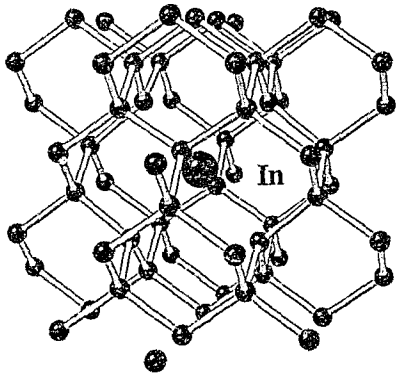

Figure 5.4: Stable <111> In defect on a bond-centred position between two lattice vacancies as viewed slightly away from the <110> channeling direction.

considered are given in Table 5.1. As can be seen from these the V_C-In-V_C defect orientated along the <111> direction is the most likely stable defect of those that we considered.

The electric field gradient tensor V_{ij} has been calculated from the charge density matrix $\rho(\mathrm{r})$, using

$$V_{ij} = \int \rho(\mathrm{r})(3\frac{x_i x_j}{r^5} - \frac{\delta_{ij}}{r^3})d\mathrm{r} \tag{5.15}$$

where the integral has been replaced by a finite summation over the charge density grid. This summation extends over several unit cells of the lattice to ensure radial convergence. From the electric field gradient tensor matrix we calculated the quadrupole coupling frequency in the usual way,

Defect	$E_f(eV)$	$E_b(eV)$
In substitutional	-9.752	0.027
In bond-centred <111>	-9.216	0.565
$V_C - In - V_C < 111 >^{(a)}$	-9.796	-0.020
$V_C - In - V_C < 111 >^{(b)}$	-9.797	-0.021
$V_C - In - V_C < 100 >$	-9.557	0.061

Table 5.1: Formation and binding energies of the various In based defects. $^{(a)}$ Starting from In on a substitutional site. $^{(b)}$ Starting from In on a bond-centred site.

$$\upsilon_Q = eQV_{zz}/\hbar \tag{5.16}$$

where Q is the electric quadrupole moment. This calculation suffers from error in that core polarisation has not been included and the very nature of the pseudopotential approximation precludes any of the core or inner valence states being considered. The resultant coupling frequency was about 100 MHz with a <111> high-symmetry direction.

Figure 5.5 shows the charge density contours of the V_C-In-V_C defect and surrounds, where vacancy character is observed in the directed bonds from the adjacent C atoms towards the In atom. The deep energy level of these bonds is 1.75 eV above the valence band, is doubly degenerate and doubly occupied by two electrons. As with vacancy related complexes the defect may exhibit amphoteric behaviour, so its electrical properties cannot be easily characterised.

The calculated configuration for In in pure diamond allows us to have a basis for considering the experimental results obtained in the previous chapter. This is done in the discussion in Chapter 8.

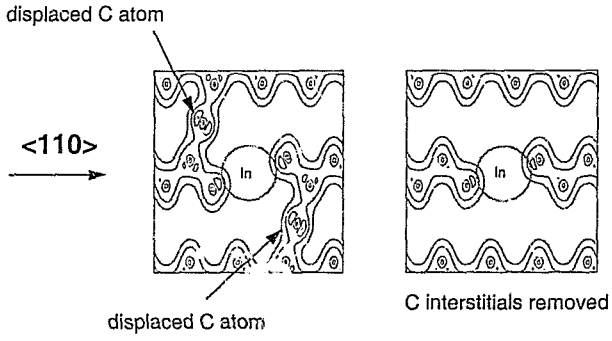

Figure 5.5: Charge-density contours of the bond-centred In defect before and after the C interstitials are removed.

Chapter 6

Theory of Elastic Recoil Detection Analysis

6.1 Introduction

In Elastic Recoil Detection Analysis (ERDA) the concentration and depth distribution of light elements in a material is determined by the detection of the elements of interest upon recoiling under MeV ion bombardment. For the case of hydrogen ERDA is one of the very few methods where quantitative distributions can be obtained. ERDA is analogous to Rutherford Backscattering Spectrometry (RBS) with the differences that the primary beam consists of particles heavier than those being profiled and that the ejectiles, not the projectiles, are detected in a forward scattering direction. The first such measurements were performed by L'Ecuyer *et al* at the University of Montreal (L'Ecuyer *et al*, 1976).

6.2 Fundamentals

A schematic diagram of the mechanisms involved in ERDA is shown in Figure 6.1. The energy of the detected recoil particle is essentially determined by two processes: the transfer of energy in the collision with the primary particle (which is obviously dependent on the energy of the incident particle), and the energy losses suffered by the primary and the recoil particles on the in- and outward paths respectively. Since the energies of the particles in ERDA are selected to be well below the Coulomb barrier, the collision is elastic and the energy transfer can be calculated using momentum and energy conservation. Thus the energy, E_2, of a recoiled particle scattered at an angle θ, immediately after impact is given as (Marion and Young, 1968),

$$E_2 = KE_1' \tag{6.1}$$

where K is the kinematic factor

$$K = \frac{4M_1M_2\cos^2\theta}{(M_1+M_2)^2} \tag{6.2}$$

and E_1' is the energy of the primary beam just prior to the collision.

6.2.1 Energy loss

The incident and recoiled particles lose energy traveling through the sample, through nuclear and electronic stopping,

$$E_1' = E_1 - \int_0^{d/sin\alpha} S_1(x)dx \tag{6.3}$$

where d is the depth at which the scattering occurs and S_1 is the stopping power of the incident ion in the material. Similarly

$$E_2' = E_2 - \int_0^{d/sin\beta} S_2(x)dx \tag{6.4}$$

where S_2 is the stopping power of the recoiling ion in the material. These stopping powers are usually obtained from a Monte Carlo program such as TRIM98 which uses

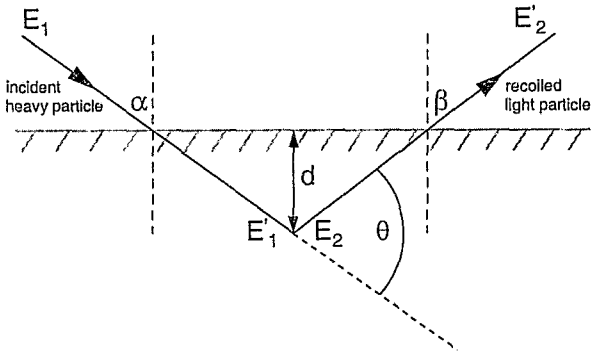

Figure 6.1: Kinematics of a simple ERDA set-up

both experimentally measured and calculated stopping powers (Ziegler *et al.* 1985).

The loss of energy by particles traveling through matter is a statistical process. Thus it is subject to statistical fluctuations which result in a spread of energy in the beam. This is known as *energy straggling* and is one of the fundamental limits in any ion beam analysis technique. Various models exist for the approximation of energy straggling, depending on the thickness of the absorber (Leo, 1994, Rauhala, 1995).

6.2.2 Scattering cross-section

The probability of a scattering event occurring is of obvious importance as it determines the sensitivity of the technique to a particular element as well as allowing the quantification of the concentration of the element in question. Since the collision is purely Rutherfordian the Rutherford differential cross-section is used, (Chu *et al*, 1978), which for ejectiles (M_2 being the ejectile), is

$$\frac{d\sigma}{d\Omega} = \left(\frac{Z_1 Z_2 e^2}{2E_1}\right)^2 \frac{(1 + M_1/M_2)^2}{\cos^3\theta} \tag{6.5}$$

This is the case where the energy of the incident ions is of the order of 1 MeV.amu^{-1} (Arnold Bik and Habraken, 1993). In both the low-energy case, where orbital electrons contribute significantly to the scattering potential, and the high-energy case where nuclear forces play a role, Equation 6.5 cannot be applied[1]. The use of heavy ions as projectiles has a greater sensitivity, due to the increased cross-section. Heavy ions, with their larger stopping powers, cannot probe as deeply as light ions however (using TRIM98 20 MeV ^{4}He is calculated to have a range of 113 μm, whereas ^{28}Si of the same energy has a range of only 4.0 μm), but this is compensated by better depth resolution.

In the case of heavy projectiles and light ejectiles we have $M_1 \gg M_2$. For the case of hydrogen $M_2 = 1$ and then $1 + M_1/M_2 \approx M_1$

$$\therefore \frac{d\sigma}{d\Omega} \approx \left(\frac{Z_1 Z_2 e^2}{2E_1}\right)^2 \frac{M_1^2}{\cos^3\theta} \tag{6.6}$$

Now $M \sim 2Z$ and we then obtain a Z^4 dependence for the scattering of hydrogen by heavy ions.

6.2.3 Depth resolution

For any ion beam analysis (IBA) technique that probes the bulk of a material, depth resolution is of obvious importance. This is defined in ERDA as (Turos and Meyer, 1984),

$$\Delta x = \frac{\Delta E}{S} \tag{6.7}$$

where ΔE, the energy spread, is the total energy resolution of the experimental set-up, and S is the effective stopping power,

$$S = \frac{\delta E_d}{\delta x} = \frac{\delta E_d}{\delta E_2'} \frac{\delta E_2'}{\delta x} \tag{6.8}$$

E_d being the energy of the detected recoil (which differs from E_2' when an absorber foil (detailed further on in this chapter), is placed in front of the detector - see 6.2.4). The energy spread arises from a number of factors:

[1]For 1.0 MeV He on a high-Z target (Bi), the scattering cross-section was found to deviate by approximately 4% (L'Ecuyer *et al*, 1980).

(i) the detector energy resolution, ΔE_d (for a normal surface barrier detector this is approximately 30 keV)

(ii) kinematic broadening, ΔE_g, due to the finite acceptance angle of the detector

(iii) energy straggling

(iv) multiple and double scattering , which result in an energy spread due to scattering kinematics

(v) surface roughness effects

(vi) straggling in the absorber foil, if one is present. For 2.5 MeV He scattering hydrogen into a 9 μm foil in a typical scattering geometry this is approximately 32 keV (Turos and Meyer, 1984). Any non-uniformity in thickness will have a pronounced effect

Values for some of the above factors have been calculated for our system and are given in Section 7.2.3. Usually one can neglect the energy and angular spread of the incident beam. For instance, the terminal voltage of the SRCNS tandem accelerator has variations of the order of 2-3 keV which, for a 25 MeV beam of ions, would result in an error in energy of the order of $\Delta E/E$ = 0.04-0.06%. In the case of our ERDA set-up, the beam is focussed onto the sample and the angle of convergence is $< 0.6^o$. In normal ERDA, using a surface barrier detector, depth resolutions of typically one to several hundred ångstroms are obtained (Doyle and Brice, 1988).

Kinematic broadening

The energy of the recoiled particles has a strong angular dependence ($\sim \cos^2\theta$, see Equation 6.2). Thus there is a geometrical contribution to ΔE arising from both the finite size of the beam spot and the acceptance angle of the detector. In the case of heavy recoils the kinematic energy spread is the dominant contribution to the depth resolution (Goppelt-Langer *et al*, 1996). If the detector aperture is narrow then

the depth resolution is reasonably better for heavier recoils than for light ones. The geometrical broadening is given by (Turos and Meyer, 1984),

$$\Delta E_g = \Delta\gamma\left[(E_1 - E_1')\frac{\delta k}{\delta\theta} + (kE_1' - E_2)\cot(\theta - \alpha)\right] \tag{6.9}$$

where the first term in the square brackets, the kinematical factor, is the energy spread due to the different scattering angles, and the second term is the result of the different path-lengths in the outgoing beam. $\Delta\gamma$ is the effective detector acceptance angle which can be approximated by (Williams and Möller, 1978),

$$\Delta\gamma = \frac{1}{D}\left[s^2 + w^2\sin^2\beta/\sin^2\alpha\right]^{1/2} \tag{6.10}$$

where D is the detector-sample distance, s is the width of the detector aperture and w is the incident beam width in the scattering plane.

Multiple and double scattering

Apart from energy straggling, which has already been described, the statistical nature of the energy loss process also results in a spread of ion direction. This accordingly causes a spread in energy, both through a change in recoil angle and through variations in the path-lengths traveled in the material. This is known as multiple scattering and forms a major contribution to the depth resolution in ERDA, unlike in the case of RBS (Wielunski, 1996, and Wielunski *et al*, 1998). This is due, in the case of change of recoil angle, to the high sensitivity of the method to the geometrical set-up (the $1/\cos^3\theta$ dependence of the cross-section in Equation 6.5), and the path-length variations are accentuated by the grazing incidences commonly used. As the depth probed increases, so does the influence of multiple scattering (Turos and Meyer, 1984). Its effects are also greater in high-Z materials, due to the higher scattering cross-sections (Wielunski, 1996, and Wielunski *et al*, 1998). The best depth resolutions have thus been shown to be for samples with the lowest atomic number and the smallest scattering angle (Wielunski, 1996).

The sensitivity of ERDA has been shown to be limited by a continuous, almost constant, low-energy background (Wielunski, 1996). This is thought to be due to double scattering events, such as hydrogen small angle scattered off heavy sample atoms, or possibly hydrogen recoils from secondarily scattered incident particles. The small high energy tails seen in some spectra well above the surface peak, can also be explained by this mechanism.

Related to these events, and a common limit to sensitivity in ERDA measurements are events due to hydrogen present on the sample surface in the form of hydrocarbons, water and the like (Wielunski *et al*, 1986). Multiple scattering of such recoils maps surface events into the bulk (through reduction of their energy), forming a lower bound to the detection limit. If the system is at a very low vacuum (10^{-10} Torr), and the surface is cleaned *in situ*, then sensitivities of 1 ppm (atomic) have been reported (Wielunski *et al*, 1986).

Surface roughness

It was first shown in RBS measurements that the smoothness (or alternatively the roughness), of the sample surface influenced both the shape and the depth resolution of spectra (Schmid and Ryssel, 1974, and Edge and Bill, 1980). These effects were found to become important as target orientations approached grazing emergence (where both the shape and amplitude of the spectra were affected), or incidence (where mainly the amplitude was modified), (Knudson, 1980). Thus ERDA, with its extremely large incident and exit angles, is particularly susceptible to surface roughness effects (Doyle and Brice, 1988).

6.2.4 Detectors in ERDA

The detector used in an ERDA measurement is very much dependent on the type and the number of different recoils being detected. The two most important properties of any detector are its intrinsic energy resolution, which is a limiting factor of the

experimental depth resolution, and the detector solid angle, which affects both the deterioration in depth resolution due to kinematic spread, and increases the number of detected recoils and thus the count rate for a given incident beam flux.

The simplest and most common detector set-up is that of a silicon surface barrier detector (SSB) with an *absorber foil* (range/stopper foil), typically a few micron thick mylar foil or the like, placed in front of the detector to stop usually all but the lightest recoils (and thus the incident heavy particles and the heavy matrix do not interfere[2]). This absorber foil degrades the depth resolution, both through energy straggling , as well as multiple scattering in the foil. The thickness uniformity of this foil, if present, is considered to be the single most important factor in the depth resolution of the system (Doyle and Brice, 1988), due to the large amount of energy that is lost by transmitted ions. This is the major reason for the use of polymers such as mylar as absorber foils, because of their superior thickness uniformity. The thickness of this foil must also be known to the greatest possible accuracy for correct analysis of the spectra. The effect of the absorber foil is greatest for recoils originating at or near the surface of the sample, as the energy straggling contributions from the sample are minimal in this case.

Particle identification

In many cases it is desirable to measure a number of different elements within a sample. It is then necessary to identify the recoiled particles. This identification is commonly based on the determination of one characteristic parameter of the recoil in combination with its kinetic energy. One can measure the velocity of the particle in time-of-flight (TOF) spectrometry (Groleau *et al*, 1983, and Thomas *et al*, 1983), momentum-over-charge in magnetic spectrometry (Gossett, 1986), or the stopping power in dE-E measurements (Yu and Gustafsson, 1986, and Stoquert *et al*, 1989). These methods do not usually utilize an absorber foil and thus do not suffer from the deterioration in depth

[2]The geometrical set-up of an ERDA system also often kinematically precludes the heavier between the incident particles and the matrix being scattered into the detector.

resolution inherent in its use, although in some cases it is still prudent to use a foil if the count-rate due to recoiled primary ions is too high (for the counting system), (Yu and Gustafsson, 1986). Other methods also exist for particle identification, such as pulse shape discrimination (Klein and Rijken, 1992), based on the differential in stopping power leading to a different shape in the pulse generated in the detector; or an $E \times B$ filter (Ross *et al*, 1984), which replaces the absorber foil and allows the identification of various recoils.

Position sensitive detectors

In ERDA there is always a trade-off between count-rate and depth resolution. The larger the solid-angle of the detector the larger the count-rate (and thus the less the radiation damage to the sample), but the depth resolution is worsened due to kinematic broadening. This problem can be mostly overcome using 2-dimensional position sensitive detectors, where not only the energy of an incoming particle, but the position at which it strikes the detector (and thus its recoil angle), are recorded. Such systems are usually magnetic spectrographs or gas ionization detectors. Using a complex Q3D magnetic spectrograph atomic depth resolution has been achieved (Dollinger, 1993). Sensitivities of the order of 10-100 ppm have also been achieved (Assmann *et al*, 1996). The development of a simple system using a 2-dimensional position sensitive SSB by our group is detailed in the next chapter.

6.2.5 Secondary nuclear reactions

Although the incident ions in ERDA have energies of 1-2 MeV.amu^{-1} which are lower than the Coulomb barrier, it is possible for enough energy to be transferred to the light recoils such that they will have energies well above it. In the case of 130 MeV Ni on diamond the detection of high energy He recoils has been shown to be as a result of nuclear reactions between recoiled carbon atoms and the carbon atoms of the matrix (Assmann *et al*, 1996). The possibility of inelastic sub-barrier reactions does exist and should be checked for in each measurement.

6.3 Radiation damage

Radiation damage is one of the fundamental limits for any IBA technique. The ability to measure the elemental profile of a sample before it is altered by the irradiating beam is crucial. This is especially important for the lighter elements which are in general more mobile under irradiation (Dollinger *et al*, 1996). At first one would assume heavy-ion ERDA to create more damage than if one used a light, for example helium, beam to interrogate the sample. However, in the case of electronic energy loss (which is the major contributor to energy loss for almost the entire depth range analysed), the energy loss scales with Z of the incident beam, compared to the cross-section which scales as Z^2 or Z^4 (see Equations 6.5, 6.6 and the corresponding discussion). Thus, for the same number of detected recoils, the radiation damage is in fact smaller. The same is the case for sample heating (Ross and Terreault, 1980), which again scales as Z while the cross-section scales as Z^2 or Z^4. Certain materials however, including some insulators, semiconductors and metals, have a strong nonlinear dependence of radiation damage on electronic stopping power (Wang *et al*, 1994, and Toulemonde *et al*, 1994). When nuclear stopping has to be taken into account, it is found to be roughly independent of the projectile used (Dollinger *et al*, 1992).

Another process which occurs during irradiation is the diffusion of mobile species by various electronic processes (Dollinger *et al*, 1996). Volatiles, such as hydrogen, can become activated and diffuse within the sample (or to the surface and are lost). This process and any other radiation damage effects can be monitored by performing dose-dependent measurements on the samples of interest.

6.4 Summary

This chapter has described the physical processes involved in the ERDA technique, such as scattering and energy loss. The most important equation to note is Equa-

tion 6.5, the Rutherford cross-section, which is used to describe scattering below the Coulomb barrier. Evident from this equation is the greater sensitivity of heavy ions as probes, due to the increased scattering cross-section. Equation 6.6 is a special case for heavy ion projectiles and hydrogen as the ejectile of interest. In this scenario the sensitivity is even more increased. The greater sensitivity of heavy ions, especially for hydrogen, as described by these two equations, are the reason for the heavy ion beams used in the experiments described in the following chapter.

The factors which limit the depth resolution (and sensitivity) of ERDA have been given and detailed. These factors have been important experimental parameters in the ERDA measurements undertaken in this thesis. One of them, kinematic broadening, was the reason for the development of the 2-D PSD system detailed in Section 7.2.3. Finally further benefits of using heavy ions, in this instance due to reduced radiation damage of the sample, have been discussed.

Chapter 7

Elastic Recoil Detection Analysis Measurements

7.1 Introduction

As mentioned earlier the importance of hydrogen as an impurity in diamond cannot be overstated. Its abundance in both natural and synthetic, particularly CVD, diamond has been confirmed. In silicon and germanium it is known to form complexes with various dopants and the formation of In-H pairs in these materials has been well documented (Wichert *et al*, 1987, Deicher *et al*, 1989, Skudlik *et al*, 1992a, and Skudlik *et al*, 1992b). It is thus the most likely impurity candidate for complexation with indium. In order to facilitate the study of such In-H interactions, if they occur, it is necessary to further study the behaviour of hydrogen in diamond, about which a great deal is still unknown. This has been accomplished through the ERDA technique outlined in Chapter 6. Along with studies on hydrogen mobility, a necessary mechanism for In-H formation, various different hydrogen distributions have been studied, for the added information on synthetic and natural diamond genesis that they provide.

The ERDA measurements performed at the Schonland Research Centre for Nuclear

Sciences in the last few years have served a dual purpose: the development of a sophisticated 3-dimensional ERDA system, and the imaging of hydrogen at trace levels in diamond in order to gain further insight into its dynamics within the diamond lattice. This is a natural progression from the laboratory's successful NRRA and conventional ERDA work on hydrogen in diamond (Sellschop *et al*, 1980, Madiba *et al*, 1983, Madiba *et al*, 1988, and Smallman *et al*, 1996). As mentioned the primary goal has been to understand the hydrogen in diamond system further as a basis for interpreting and observed In-H interactions. A large number of publications have resulted from this work: (Connell *et al*, 1996, Connell *et al*, 1997, Connell *et al*, 1998, Doyle *et al*, 1997, Machi *et al*, 1997, Machi *et al*, 1999, Maclear *et al*, 1998, and Maclear *et al*, 1999), and those from 1997 onwards form the basis of this chapter.

7.2 Experimental set-up

All measurements were conducted at the Schonland Research Centre for Nuclear Sciences, using the 6 MV EN Tandem Van de Graaff accelerator facility. A schematic of the facility is shown in Figure 7.1. Negative ions, both $^{35}Cl^-$ and $^{28}Si^-$, were obtained from a model 860A Cs-sputter ion source. These were directed and focussed into the high voltage accelerator where they were accelerated to 25 MeV in the case of ^{35}Cl and 21.6 MeV in the case of ^{28}Si. The required beam energy was selected by the analyser magnet and a switcher magnet steered the beam into the microprobe beamline. The energy is determined by both the terminal voltage of the accelerator and the charge state selected by the magnets, being 5 MV and +4 for ^{35}Cl, and 5.4 MV and +3 for ^{28}Si, respectively. These energies were confirmed by directly measuring the beam energy using a SSB detector. Other beam energies were also used, namely 30 MeV ^{35}Cl and 15 MeV ^{28}Si. These beams all have comparable ranges in diamond: these have been calculated using TRIM98, and are given in Table 7.1. The magnetic rigidity of the beam was decreased by using a gas post-acceleration stripper which increased the charge state, to enable the beam to be bent by the analysing magnet and to be focussed by the quadrupole lenses of the microprobe. Maximum transmission of the

beam through the facility was achieved using magnetic quadrupole lenses and electrostatic steerers to focus and direct the beam.

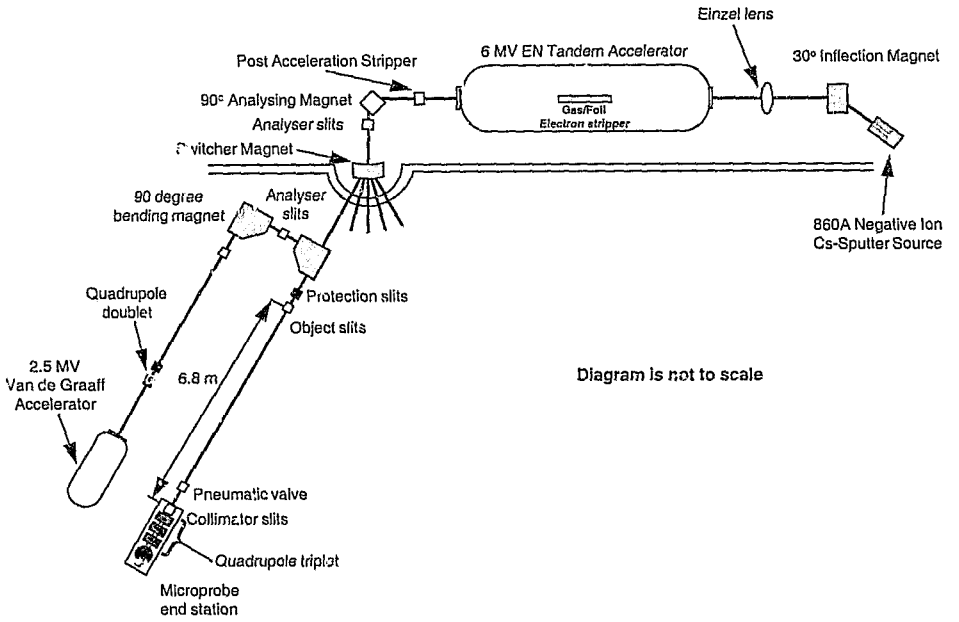

Figure 7.1: A schematic of the Schonland tandem accelerator facility, showing the attached microprobe system and 2.5 MV single-ended Van de Graaff accelerator

The ERDA sample is usually set at an angle ((90°-α) - see Figure 6.1), of approximately 15° to the beam, with the centre of the detector at approximately 35° to the beam (i.e. 180°-($\alpha+\beta$)). This detector angle kinematically excludes all but a few low energy ^{12}C ions from the diamond samples from scattering into the detector. ^{28}Si is kinematically forbidden to scatter at angles greater than 26° off ^{12}C and ^{35}Cl is forbidden at angles greater than 21°. In Figure 7.2 the energy spectrum of an ERDA measurement is

Ion	Energy	Range in diamond	Effective range at 15^o
^{35}Cl	25 MeV	4.02 μm	1.04 μm
^{35}Cl	30 MeV	4.63 μm	1.20 μm
^{28}Si	15 MeV	3.30 μm	0.854 μm
^{28}Si	21.6 MeV	4.24 μm	1.10 μm

Table 7.1: Ranges of various energy ^{35}Cl and ^{28}Si ions in diamond. The effective range is due to the fact that the sample is positioned at 15^o to the incident beam in our ERDA set-up.

shown as a function of detector angle. Note the appearance of low energy ^{12}C recoils at decreasing angles.

The number of counts recorded in the ERDA detector is a function of the flux of particles incident upon the sample. In order to measure this beam current as a function of time a gold-plated carbon fibre is swung through the beam path at a constant rate. Backscattered recoils off this fibre are measured striking an annular SSB situated at a large angle of nearly 180^o. These counts serve as a measure of the dose a particular sample receives. This particular method of target current measurement was used due to direct current measurement from the sample being complicated by the massive secondary electron emission that one obtains from diamond under irradiation, especially when using heavy ions. On average the dose used in an ERDA run was 2×10^{15} ions/cm^2.

All diamond samples are prepared using the following method: the sample is cleaned in a 3:2:1 mixture of sulphuric, nitric and perchloric acids, rinsed in Contrad (an industrial chelating cleaner, Decon Laboratories, Brighton, England), and finally rinsed in deionised water.

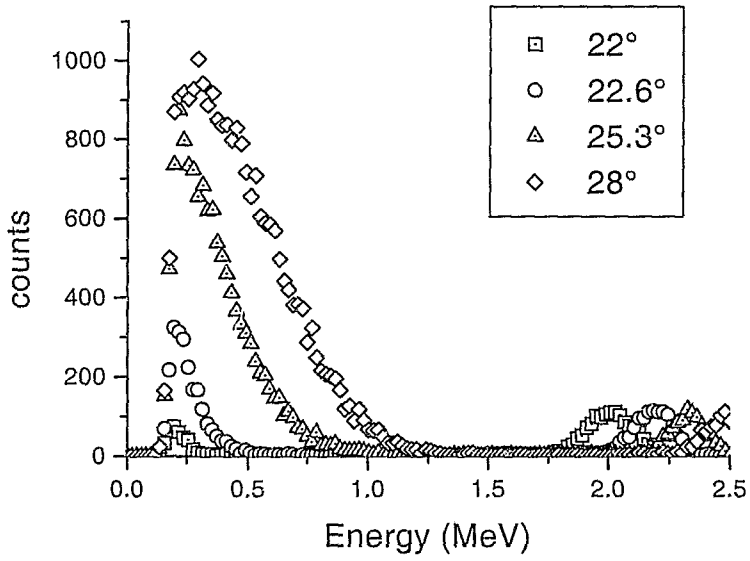

Figure 7.2: Raw ERDA energy spectrum showing the kinematic exclusion of scattered ^{12}C ions as a function of scattering angle. The ^{12}C ions in the spectrum are those with lower scattering angles, and thus have sufficient energy to completely penetrate the mylar absorber foil. Note also the shift of the high energy surface peak.

7.2.1 Nuclear microbeams

ERDA allows one to determine the 1-dimensional depth profile of light impurities in a material. In order to obtain a fully 3-dimensional picture of the light impurity distribution one must also scan the interrogating beam across the sample. One is then able to either select an area from the 2-dimensional surface scan and view the corresponding depth distribution or alternatively view the entire depth distribution and select the depth range of interest. The 2-dimensional distribution at that depth is then displayed. It is desirable to have as small a beam-spot as possible in order to provide as high a position resolution as possible. This is achieved by use of a nuclear microprobe which is, in its simplest form, a set of lenses which focus the beam down to a spot of the order of a few microns in diameter. Thus one is able to speak about 3-dimensional micro-ERDA or 3-D μERDA.

The SRCNS nuclear microprobe facility (Andeweg *et al*, 1997), is coupled to both the 6 MV Tandem accelerator and a 2.5 MV single-ended Van de Graaff accelerator, as can be seen in Figure 7.1. It consists of a quadrupole triplet lens system, object and collimator slits (6.8 m apart), and pre-lens deflection coils, all purchased from Oxford Microsystems (Grime *et al*, 1991). Water-cooled pre-collimator slits are in place before the object slits in order to protect them from damage due to excessive beam dose.

The microprobe chamber itself contains a $XYZ - \theta\phi$ manipulator with attached stepper motors and control system, allowing the sample position and tilt to be adjusted. The entire beam line, from ion source to target chamber is under high vacuum, the microprobe chamber itself being serviced by a turbo pump with an accompanying liquid nitrogen cooled baffle and cryotrap. This enables vacuums of better than 1×10^{-7} Torr to be achieved.

As discussed in Chapter 6, the finite size of the beam spot causes a geometrical contribution to the energy and thus the depth resolution of the system. Use of a few micron sized spot greatly reduces this contribution. There is a contribution to the energy resolution due to the beam convergence in the microprobe, but this is negligible because of the distance over which the focusing occurs. The depth resolution of our system is estimated to be 300 Å.

7.2.2 Non-position-sensitive detector system

Before the development of the 2-D PSD system at the SRCNS, and as a test of the system, a normal non-position-sensitive SSB detector was used (Connell *et al*, 1996). This was equipped with a 1 mm collimator, considered a suitable compromise between count rate and energy resolution. A 10.5 μm aluminium foil was used to stop heavy recoils.

7.2.3 Development of 2-D PSD system

The reasons for utilising a position sensitive detector have been detailed in Section 6.2.4, i.e. greater count rate with equal or increased energy resolution. Our group has pioneered the use of a simple 2-dimensional position sensitive surface barrier detector for ERDA measurements (Doyle *et al*, 1997). The detector works on the principle of resistive charge division where the position of a particle striking a detector is calculated from the ratios of the charge collected on either side of the detector to the total charge collected. The particular detectors used were obtained from Messrs. Q-Par Angus of Herefordshire, United Kingdom. A comparison of the solid angle of these with those of the detectors used in various ERDA laboratories is given in Table 7.2. Our detector enjoys the second largest solid angle of all the ERDA systems found in the literature. The only greater is the ionisation counter at Munich which is also 2-D position sensitive.

A schematic of our detector-sample configuration is shown in Figure 7.3. A 14.75 μm mylar absorber foil is used to stop the heavy recoils. In order to lower the leakage current and thus the noise of the detector, it is mounted on a Peltier device which exhausts to a chilled water circuit. This enables the detector to be operated at -20°C, which substantially reduces the noise. There are three energy outputs from this detector, namely E_X_L, E_Y_T and E_Y_B. These must be recorded along with the RBS energy signal from the beam current measurement system and the X, Y coordinates from the deflector coils which scan the beam across the sample surface. Thus one is required to use a multi-parameter Data Acquisition System (DAS). Event-by-event capability is also required in order to calculate various parameters (for instance the total energy of an incoming ion in the PSD is $E\_Y_T + E\_Y_B$), and to investigate time/dose dependent effects. The development of this ERDA system was one of the driving forces for the development of the *Collect* DAS discussed in the next section.

Institute	Solid angle (msr)	Detector	Reference
SRCNS	2.7	2-D PS SSB	Doyle *et al*, 1997
Munich	6.5	Ionization counter	Assmann *et al*, 1994
New Delhi	0.65 and 0.15	SSB	Avasthi *et al*, 1995
McMasters	0.73	E-ΔE	Siegele *et al*, 1996
INRS	0.066	SSB	Schiettekatte *et al*, 1996
Garching	1.73	SSB	Behrisch *et al*, 1996
Arizona State	1.07$\pm$ 0.05	SSB	Bair *et al*, 1996
Eindhoven	0.16	SSB	Maas *et al*, 1996
Typical system (1% energy resolution)	0.5	SSB	Assmann *et al*, 1996

Table 7.2: Detector solid angles of various ERDA laboratories. All but ours and that used by the Munich group are non-position-sensitive detectors. That used in Garching is actually an ionization chamber with a greater solid angle, but it is limited by a SSB (Silicon Surface Barrier) detector at the back of the detector which is used for energy measurement.

Some factors must be considered with respect to the energy resolution of the 2-D PSD:

- the acceptance angle of the PSD at 50 mm from the target is 4 mrad = 0.229^o (using the 0.2 mm position resolution of the detector). If we use Equations 6.1 and 6.2, for a 1.5 MeV hydrogen ion striking the detector positioned at 35^o to the beam, we obtain a geometrical broadening of $\Delta E_g = 8$ keV
- according to the detector manufacturers the thickness variation in the Mylar foil is $\pm$0.5% (i.e it is uniform to 1%). Using stopping tables generated by TRIM98 the energy broadening due to the foil is $\Delta E_f = 4$ keV
- we assume a nominal detector resolution (also according to manufacturers specifications), of $\Delta E_d = 30$ keV.

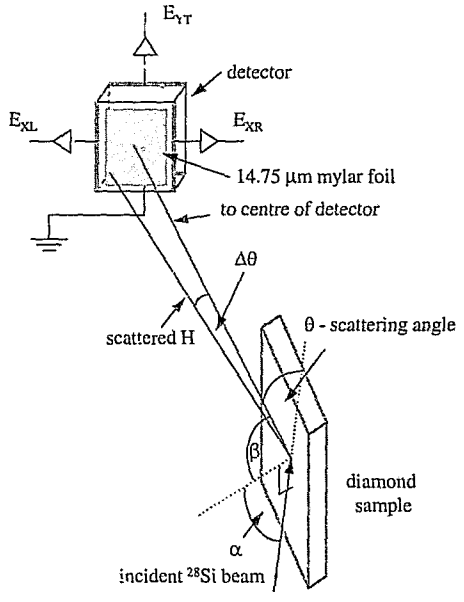

Figure 7.3: A schematic of the detector-sample configuration for the 2D-PSD showing scattering processes at different angles.

These factors contribute to a total energy resolution of the system of

$$\Delta E_{tot} = \sqrt{\Delta E_g^2 + \Delta E_f^2 + \Delta E_d^2} \tag{7.1}$$

which gives $\Delta E_{tot} = 31$ keV. It should be noted that not all factors have been taken into account, such as surface roughness, which varies from sample to sample, and is one of the most important contributions.

7.2.4 The *Collect* data acquisition system and *PAW*

The collection of multi-parameter data sets required the development of a multi-parameter data acquisition system. Such a system was developed by S. Ballestrero and tested by members of the SRCNS ERDA group (Ballestrero *et al*, 1999). The system, *Collect*, front-ends the Physics Analysis Workstation (PAW/PAW++), developed by CERN. PAW is a data presentation and manipulation program, originally developed for use in a high-energy physics environment. *Collect* is the first port of this software to a small laboratory environment. It is a single threaded program written in C++.

At the SRCNS *Collect* is used to collect data from a CAMAC system, which in turn accepts signals from standard NIM (Nuclear Instrumentation Methods) electronics. Before use one configures the source code to reflect the modules present in the CAMAC crate, a minimum of a crate controller (CC), list sequencer (LS) and a data capture module, usually an analog to digital converter (ADC). The LS buffers incoming data, so that data transfer to the computer only occurs when the buffer is half-full (8 kb). This removes continuous computer-CAMAC communication, which greatly reduces the dead-time of the system. In principle any CAMAC module can be implemented in the system. A bit pattern module and a scaler have already been successfully tested. *Collect* initialises the CAMAC and its various modules through NAF commands[1], controls the transfer of data via a General Purpose Interface Board (GPIB) situated within the computer and writes the data into a so-called hbook ntuple, a set of ordered (cyclically) data in the format used by PAW. The data can then be visualised in PAW both on-line and after the experiment.

PAW allows one to reread the data event-by-event under various user-defined conditions, known as cuts. Thus one can select signals in certain energy ranges, or from

[1]NAF stands for the CAMAC station number (N) i.e. the slot that the particular module is in, the sub-address (A) e.g. the 3rd input of an ADC, and (F) is the function code, such as that to read the value of that input.

a particular detector etc. This is particularly useful for removing low-energy noise, selecting regions of interest on the the sample (by making cuts on the voltages to the beam scanner), and the like. One can also plot data as a combination of signals. The 2-D PSD has three outputs E_X_L, E_Y_B and E_Y_T (see Figure 7.3). The total energy of a detected particle is given by $E\_Y_T + E\_Y_B$. This is easily visualised using PAW. Manipulated data from PAW can then be output, either in hbook or ASCII format, for use by other more specific data manipulation programs.

The CAMAC system used for the ERDA measurements consisted of a Kinetic Systems 3988 crate controller with a GPIB interface, a National Instruments 438.2 GPIB card, a Kinetic Systems 3982 List Sequencer and an Ortec AD811 Octal ADC. The performance of the system has been tested at 4 kHz with 15% dead-time (when 6 analog signals are being collected).

7.2.5 Silicon standards

The use of hydrogen-implanted silicon standards serves a dual purpose in ERDA measurements. Their primary function is to be used as a calibration standard in order to determine the absolute concentration of hydrogen within the samples being studied. They serve the same purpose in other ion beam analysis techniques, such as NRRA. The secondary function is, in cases where the sample or detector angles are not precisely known, to determine these angles. This is accomplished through knowledge of the depth of the implant (through TRIM98 calculations). The angles are varied until both the surface peak, and that of the implant, are at the correct depths on the spectrum. Thus both the geometry of the experimental set-up and the depth scale of the spectrum are now calibrated. An analysed silicon standard is shown in Figures 7.4 and 7.5. The implants are also performed through a collimator of known dimensions. This allows one to calibrate the $X - Y$ lateral dimensions of the spectrum.

These standards are prepared through low energy ion implantation of the hydrogen,

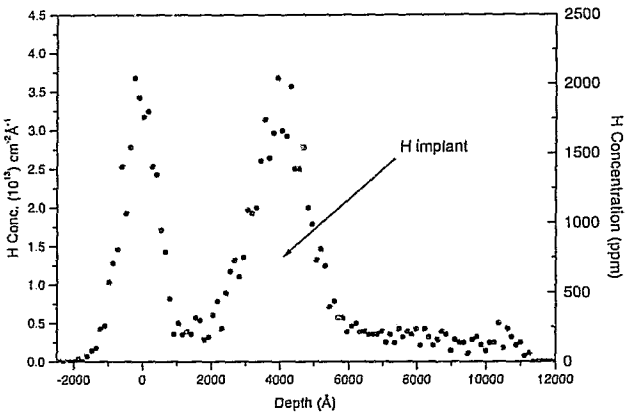

Figure 7.4: ERDA spectrum of the hydrogen-implanted silicon standard.

at typically of the order of 35 keV and around a dose of $5 \times 10^{16}\text{cm}^{-2}$. To prevent diffusion of the hydrogen the implant region is pre-damaged using silicon ions. This damage serves as traps for the hydrogen. Such silicon standards have been proven to be radiation and thermally stable (up to 250°C), (Whitlow *et al*, 1984).

7.2.6 Data analysis

The analysis of ERDA data consists of two primary steps. Firstly, one must determine the depths at which the hydrogen recoils originated from, that is, one must convert one's spectrum from an energy to a depth scale. Secondly, one must determine the concentration of the hydrogen present in the sample, in our case by use of a silicon standard and measurement of the integrated beam current. The 2-D PSD system requires a further step - the kinematic broadening due to the large solid angle of the detector must be eliminated through knowledge of the position on the detector at which the ion struck.

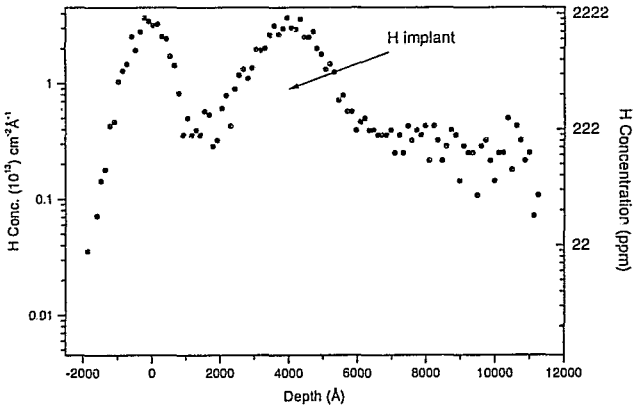

Figure . ' . ERDA spectrum of the hydrogen-implanted silicon standard on a log scale.

Mapping the 2-D events to a simple energy scale

The analysis of 2-D ERDA data involves the reconstruction of all events striking the detector to the energy that would have possessed if they had struck the centre of the detector. We rewrite Equation 6.1 for a recoil from a certain depth if it strikes the detector at both the centre and at a point P. We have respectively,

$$E_{centre} = \frac{4M_1M_2\cos^2\theta}{(M_1+M_2)^2}E \tag{7.2}$$

and

$$E_P = \frac{4M_1M_2\cos^2(\theta+\Delta\theta)}{(M_1+M_2)^2}E \tag{7.3}$$

where E is the energy of the incident particle just prior recoiling the hydrogen, θ the angle to the centre of the detector and $\theta+\Delta\theta$ the angle to the position P on the detector. From Equation 7.3 we have

$$E = \frac{E_P}{\cos^2(\theta+\Delta\theta)}\frac{(M_1+M_2)^2}{4M_1M_2} \tag{7.4}$$

and substituting this into Equation 7.2 gives

$$E_{centre} = \frac{E_P\cos^2\theta}{\cos^2(\theta+\Delta\theta)} \tag{7.5}$$

Previous to this the energy detected is corrected for energy loss in the absorber foil using stopping power tables generated by TRIM98. The angles are also corrected for the slight deviation due to the scan position on the sample. A plot of an uncorrected and a corrected energy spectrum is shown in Figure 7.6

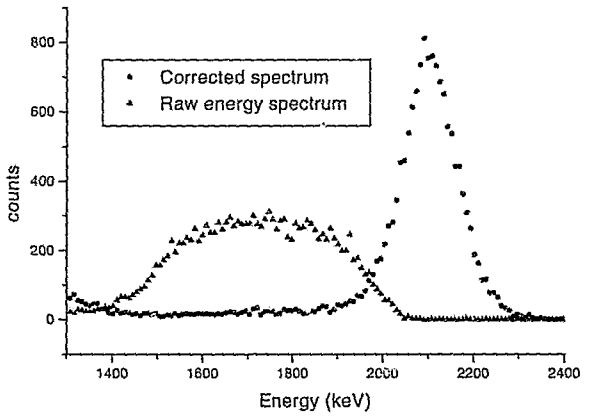

Figure 7.6: Energy spectrum of both the raw energy recoils on the detector and the corrected spectrum after "software collimation".

The deviation in angle when an event is detected at P as opposed to the centre of the detector also results in a change in the cross section. Similarly to the derivation above and using the Rutherford differential cross-section, Equation 6.5, we obtain,

$$\left(\frac{d\sigma}{d\Omega}\right)_{centre} = \left(\frac{d\sigma}{d\Omega}\right)_{P} \frac{\cos^3(\theta + \Delta\theta)}{\cos^3\theta} \tag{7.6}$$

This correction turns out to be negligible ($\approx 0.1\%$), but would be important if one was to move to a larger detector, or if improved position resolution in the manufacture of the detector allowed one to move it closer to the sample.

Converting from energy to depth

A number of processes determine the energy of the ions striking the ERDA detector. These have been detailed in Chapter 6. Essentially the incident ion loses energy penetrating the sample. Then the ion of interest is recoiled towards the detector with an energy dependent on both the scattering angle and the energy of the incident ion. This recoiled ion also loses energy exiting the sample.

The analysis of ERDA data looks at these processes in reverse. One knows the energy of the detected hydrogen ion and the angle at which it was scattered (either from the experimental set-up or through use of a silicon standard). The energy of the ion before traversing the absorber foil is calculated using interpolation from stopping powers generated by TRIM98. This energy is taken as the energy of the scattered ion at the depth d at which the scattering interaction occurred[2]. Equations 6.1 and 6.2, that is,

$$E_2 = KE_1' \tag{7.7}$$

and

$$K = \frac{4M_1M_2\cos^2\theta}{(M_1+M_2)^2} \tag{7.8}$$

allow us to determine the energy of the incident heavy ion just before scattering. The energy of the incident beam before entering the sample is known and thus gives the energy lost by the incident ion in the sample. We integrate over the relevant part of the TRIM stopping power tables (generated for the particular heavy ion, ^{28}Si or ^{35}Cl, in the material, whether diamond or silicon). This yields the length traversed by the ion in the sample, and the geometry of the set-up allows one to calculate the depth at which the hydrogen was located.

[2]The energy loss of the hydrogen traversing the sample is neglected. This introduces an error of about 1% in the depth, due to the large difference in stopping powers between hydrogen and that of the incident ^{28}Si or ^{35}Cl beam (Connell *et al*, 1996).

Concentration determination

The yield of hydrogen recoils originating from a depth x is given by,

$$Y(x) = N(x)\frac{d\sigma}{d\Omega}[E(x)]n_i\Delta\Omega \tag{7.9}$$

where $N(x)$ is the concentration of hydrogen in the sample at depth x, n_i the number of ions incident on the sample and $\Delta\Omega$ the detector solid angle. In Equation 6.5 we see that the scattering cross-section, and thus the yield, has a $1/E^2$ dependence. Thus the cross-section and the yield, and hence the sensitivity of the ERDA technique, increases with depth, due to the decreasing energy of the incident projectiles. Measurement of the silicon standards detailed previously, with known hydrogen concentration as a function of depth, allows one to use Equation 7.9 to determine the hydrogen concentration at the position in the sample in question.

7.3 Results

7.3.1 2-D PSD system

Use of the 2-D PSD detector has resulted in a dramatic increase in count rate beyond the earlier non-position-sensitive detector system. This increase is a factor of approximately 30. Apart from the obvious reduction in radiation damage to the sample, the improved counting rate allows one to reduce the microprobe object slits to achieve a 10 μm beam spot while still, even with the resultant decrease in beam current, maintaining sufficient intensity to perform statistically accurate 3-D ERDA microscopy.

7.3.2 Determination of the detection limit of the system

As discussed in Chapter 6, the lower bound to the detection limit of ERDA is determined by multiple scattering from the surface hydrogen peak. In order to measure the detection limit of our ERDA set-up a 10 μg.cm^{-2} (~300 Å) carbon foil was measured.

The 20 MeV ^{28}Si ions are transmitted through the foil, so any events appearing in the spectrum at depths corresponding to greater than the foil thickness must be due to multiple scattering. The ERDA spectrum of the carbon foil is shown in Figure 7.7. From this we conservatively estimate our detection limit to be 100 ppm (atomic) or 1.8×10^{11} atoms.cm^{-2}.Å^{-1}.

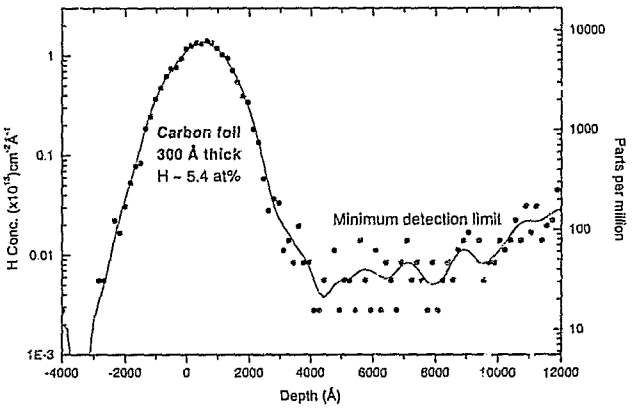

Figure 7.7: ERDA spectrum of the 10 μg.cm^{-2} (~300 Å) carbon foil, showing a detection limit of at least 100 ppm.

7.3.3 Reduction of the surface peak

In an attempt to reduce the lower limit of detection of the ERDA system one must reduce the amount of hydrogen present on the surface of the sample. Various cleaning methods do reduce the hydrogen on the surface but hydrogen accretes rapidly onto a clean surface, even at high vacuum. Thus various improvements have been made to the target chamber in order to lower the vacuum even further. These are the cryotrap and baffle mentioned earlier in this chapter. This has resulted in a vacuum of below 1×10^{-7} Torr being achieved and a hydrogen surface peak with a height of 1×10^{13} atoms cm^{-2}.Å^{-1}, the lowest yet in the microprobe chamber, being measured. Forthcoming

improvements involve sample heating to reduce the surface hydrogen even further.

7.3.4 Hydrogen diffusion studies

Our studies on the mobility of hydrogen in the diamond lattice have had two main thrusts: the investigation of the diffusion of deeply implanted hydrogen at high doses and attempts to diffuse hydrogen into the diamond bulk through exposure to a hydrogen plasma. These are both possible mechanisms to introduce hydrogen into diamond in order to see if defect interactions with indium or any other dopant do occur.

High dose hydrogen implantation

This is a continuation of the previous NRRA and ERDA work of our laboratory where high dose (3.0×10^{16} cm^{-2} or $\approx 4\%$) hydrogen implants in a natural type Ia and a synthetic (HPHT) Ib diamond were found to trap in their own range distributions up to anneals of 1473 K (Smallman *et al*, 1996, and Connell *et al*, 1996). These samples were both nitrogen rich. Thus we studied a pure nitrogen free (to the limits of IR detection) diamond in order to investigate the possibility of different hydrogen diffusion mechanisms.

The sample was a natural type IIa diamond, which was cut and polished along (100) faces. The dimensions were $8.1 \times 3.6 \times 1.6$ mm. The sample was pre-damaged using 50 keV ^{12}C ions at a dose of 1.0×10^{16} cm^{-2}. This was done to see if the implanted hydrogen would diffuse into the vacancy-rich region. Monte Carlo calculations using TRIM98 give a mean depth of 740 Å for this layer. Hydrogen was implanted at a dose of 5.0×10^{16} cm^{-2} and an energy of 25 keV. The mean depth of this implant was similarly calculated to be 1440 Å. Using TRIM98 it was calculated that, in the pre-damaged layer, there were approximately 18 vacancies available to each hydrogen atom. These were mostly as a result of the ^{12}C implantation, but some vacancies also resulted from the implanted hydrogen. The implantations were performed at room temperature. After measurement the sample was annealed at 1473 K for 30 minutes. This experiment was

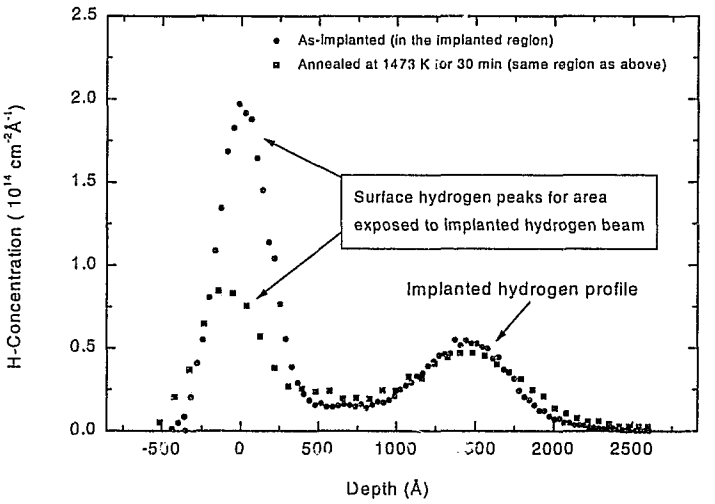

Figure 7.8: Hydrogen depth distribution by ERDA in the type IIa diamond, both before and after the 1473 K anneal. No diffusion of hydrogen is visible.

originally performed using the non-position-sensitive detector and was later repeated with the 2-D PSD. Pre- and post-anneal depth distributions of both the hydrogen implanted and a "clean" area of the diamond surface are shown in Figures 7.8 and 7.9. There is no evidence of any diffusion of the implanted hydrogen after annealing. We can conclude that hydrogen traps in its own range distribution. This self-trapping configuration is stable up to anneals of 1473 K. This concurs with the studies performed on the Ia and Ib samples. This is of great interest as implantation was the method used to introduce hydrogen into the samples in the CEEC measurements in Chapter 4. A tailing effect can be seen in the "clean" sample, which diminishes slightly on annealing,

possibly due to a slightly increased level of subsurface hydrogen. The surface peak is seen to drop substantially upon annealing, due to hydrogen being driven off the surface.

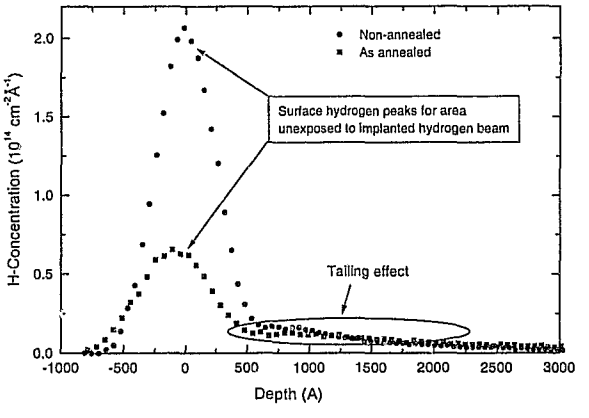

Figure 7.9: Hydrogen depth distribution in an implant-free region by ERDA in the type IIa diamond, both before and after the 1473 K anneal. A tailing effect from the surface into the bulk is clearly visible.

Hydrogen plasma treatment

A type IIa diamond sample, dimensions 10 × 10 × 5 mm, was subjected to a number of treatments. These are detailed below. The (100) surface was used for the measurements. A vacuum of 10^{-7} Torr was used throughout and a silicon standard was analysed after each treatment, just in case of any deviation in the experimental parameters. The hydrogen plasma was generated in a microwave plasma oven, modified from a commercially built microwave oven.

Experimental procedure (treatments preceding each ERDA measurement):

- *none* i.e. freshly cleaned, virgin diamond

- plasma treatment: 300 Torr, 1100 K, 40 min.
- damage creation through neon implantation: 170 keV (calculated using TRIM98 to result in a mean depth distribution of vacancies at 1450 Å), 2×10^{16} ions cm^{-2}, room temperature
- plasma treatment: 300 Torr, 900 K, 20 min.
- anneal: 1473 K, argon atmosphere, 15 min.

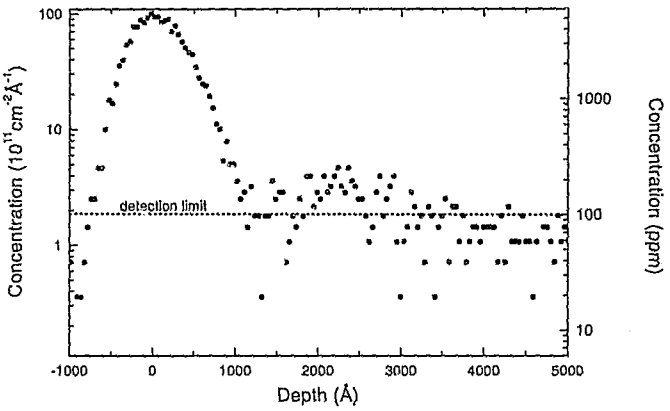

Figure 7.10: ERDA spectrum of the pure, virgin IIa diamond. The estimated detection limit of 100 ppm is indicated.

The virgin sample is used to determine the amount of hydrogen already present in the sample. The plasma treatments were performed both before and after the damage creation, to see if diffusion will occur in either the virgin diamond, or in the presence of created vacancies. The ERDA spectra for these are shown in Figures 7.10 through 7.14. A number of interesting features in these data are noted. The detection limit of 100 ppm (atomic) of our system must be stressed here. Fluctuations in the hydrogen concentration below the detection limit are observed in the spectra, but these cannot

be considered. One cannot differentiate between a hydrogen concentration measured at 100 ppm and one measured well below. Points of interest in the data are:

- the surface peak is found to broaden significantly after the first hydrogen plasma treatment
- the second hydrogen plasma treatment, after the neon damage, results in an increase of hydrogen in the bulk. This peaked just after the calculated damage peak
- annealing the diamond reduces the bulk hydrogen level, but the peak, although diminished, remains.

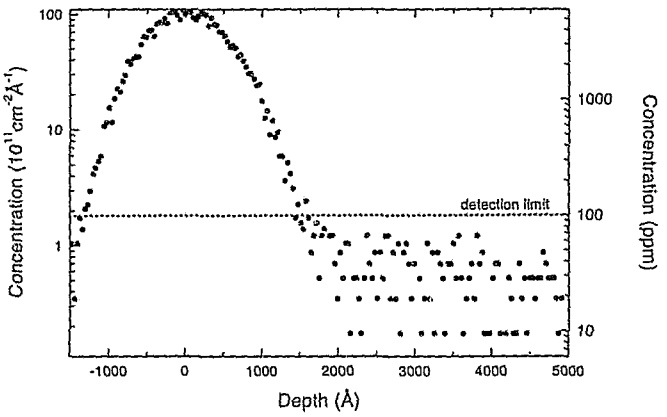

Figure 7.11: ERDA spectrum of the IIa diamond after the first hydrogen plasma treatment. The estimated detection limit of 100 ppm is indicated.

The origin of the increase in the width of the surface peak after the first hydrogen plasma treatment is unknown. The possibility of hydrogen being deposited on the surface by some mechanism, such as a vacuum fluctuation, or during the in-air transport to and from the plasma oven is small but cannot be discounted. It appears as if

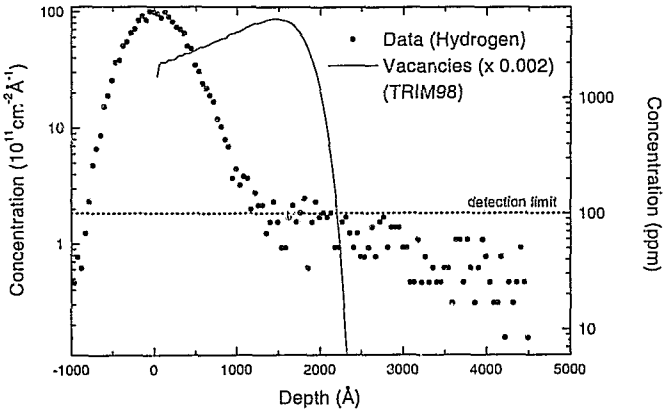

Figure 7.12: ERDA spectrum after implantation with 170 keV, 2×10^{16} ions cm^{-2} neon at room temperature to cause vacancy creation. The vacancy distribution due to the neon implantation, as calculated by TRIM98, is also shown. The estimated detection limit of 100 ppm is indicated.

plasma loading of hydrogen into the bulk is possible, but only with the assistance of pre-damage. Whether the hydrogen diffuses via the created vacancies, whether they affect the Fermi level, making diffusion possible, or contribute in some other way is still to be determined. Vacancies are postulated to be deep lying donors (Dyer and Ferdinando, 1966, Collins *et al*, 1969, and Vermeulen and Farrer, 1975). Vacancy clusters or sub-lattices are also proposed as donors in implanted diamonds (Prins, 1989). After annealing the hydrogen leaves the bulk, probably through the same vacancy-assisted mechanism. Vacancy-self-interstitial recombination, due to the anneal, limits this process, leaving the remaining, diminished hydrogen peak. The validity of a vacancy-assisted diffusion hypothesis is discussed in Section 8.1.1. It should be kept in mind that the observed diffusion was only a small effect in terms of the detection limit of this technique. Further measurements still need to be done to confirm and quantify it.

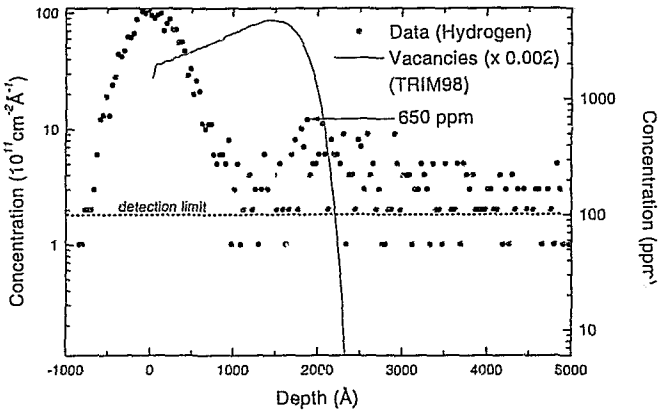

Figure 7.13: ERDA spectrum of the IIa diamond after the second hydrogen plasma treatment. Note the increase in bulk hydrogen. The estimated detection limit of 100 ppm is indicated.

7.3.5 Hydrogen distributions in natural diamond

The environment surrounding, and processes involved in, the genesis of natural diamond are of much interest to geologists. As such the mapping of hydrogen distributions is of great value. To prove the value of the ERDA technique in this field, a natural diamond known to be hydrogen rich, with microscopic inclusions, has been measured. In any material that is to be doped, be it with In or any other dopant, the initial hydrogen concentration and distribution is of interest. The inclusions are visible as zoned cloud-like areas of a gray colouration. These have been studied by optical microscopy and been found to contain sub-microscopic, light-scattering inclusions. Smaller pockets containing these inclusions have also been identified. The colour zoning due to these areas of inclusions seem to be limited by planar boundaries. The sample was a natural type Ia diamond. A map of the bulk hydrogen distribution is shown in Figure 7.15. Various regions of high hydrogen density are visible. Cuts on two of the grey fleck-like inclusions were made and the depth distributions of these, and that on a

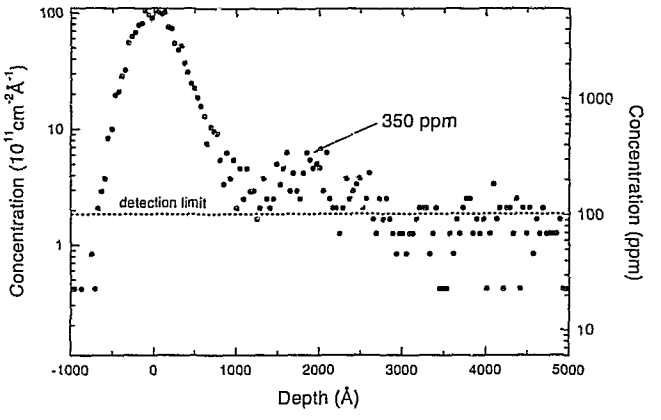

Figure 7.14: ERDA spectrum of the IIa diamond after the 1500 K anneal. The bulk hydrogen still remains. The estimated detection limit of 100 ppm is indicated.

visible inclusion free area, are shown in Figure 7.16. The concentration of hydrogen in the near-surface-bulk region of the sample was found to be quite large, up to 500 ppm (atomic), but inhomogeneously distributed. In the regions of the grey zoning the near surface concentration was found to increase to approximately 5000 ppm near the surface. We deduce that these cloudy regions are hydrogen rich. One is however unable to, using ERDA, determine the complexes that the hydrogen exists in, although hydrogen, methane and other hydrocarbons are likely candidates.

7.3.6 Hydrogen distributions in CVD diamond

As discussed in Chapter 2, the hydrogen in CVD diamond appears to lie on grain boundaries and other extended defects. We have investigated this using a large grained polycrystalline (PC) CVD diamond (~200 μm grain size). The diamond (sample NRL 5K051), was grown, under typical growth conditions, at the Naval Research Laboratories, Washington D.C. In addition the role of oxygen in the CVD growth process was studied by introduction of oxygen into the growth mixture after the diamond had

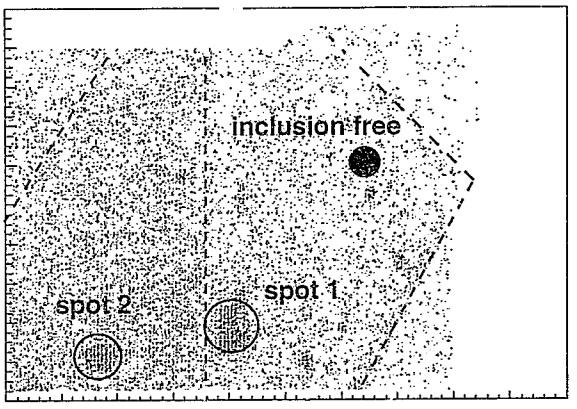

Figure 7.15: Bulk hydrogen distribution of the natural type Ia diamond. The diagonal line indicates the boundaries of the diamond. The area to the left of the vertical line is that which exhibits the grey zoning. The areas selected for the ERDA spectra in Figure 7.16 are indicated.

grown for some time. The layer grown with oxygen was found to have a lower defect concentration and larger grains (i.e. the 200 μm grains). The sample was polished both parallel to and perpendicular to the growth face. Measurements were made on both these polished surfaces. An optical photograph of the polished edge, showing the two different growth regions and the ERDA scan is shown in Figure 7.17.

A 2-dimensional scan of the bulk hydrogen distribution is shown in Figure 7.18. The layer without oxygen in the growth mixture is found to have a substantially higher hydrogen concentration. This is also shown in Figure 7.19 where a linear projection of the bulk hydrogen content is shown. Our results indicate that oxygen in the growth

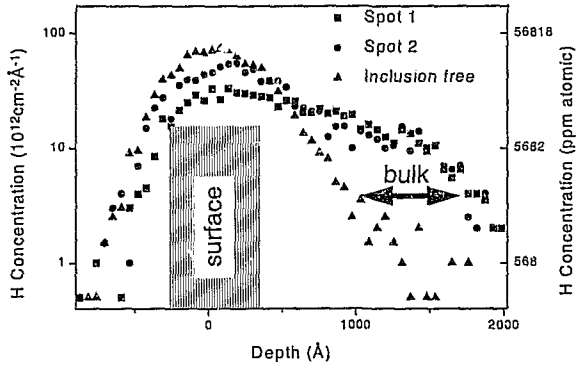

Figure 7.16: ERDA depth spectra of the areas selected in Figure 7.15 for the natural type Ia diamond.

mixture is a viable method for severely limiting the concentration of hydrogen in the resultant CVD diamond. This is thought to be due to oxygen's superior ability to scavenge defects during growth, thus limiting possibilities for hydrogen incorporation. The 2-dimensional bulk hydrogen concentration measured on the growth surface is found to be inhomogeneous, as shown in Figure 7.20. Within our experimental limits it is not seen to correlate with grain boundaries, although the possibility exists that it is still present at them. Efforts are underway to further decrease the beam-spot of the microprobe system, as it is possible that inadequate spatial resolution is limiting our ability to fully determine the details of the hydrogen distribution within such samples.

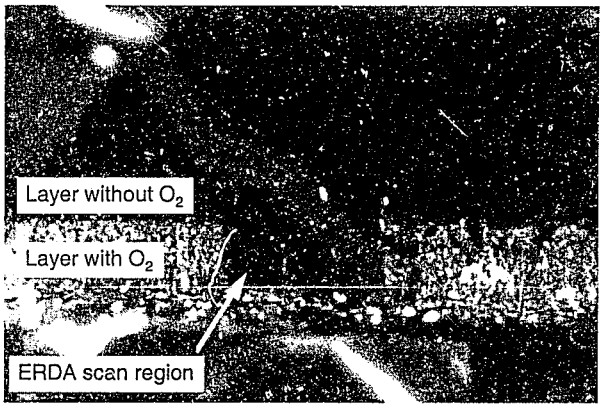

Figure 7.17: Optical photograph of the polished side of the 5K051 sample. The two growth sectors are clearly visible.

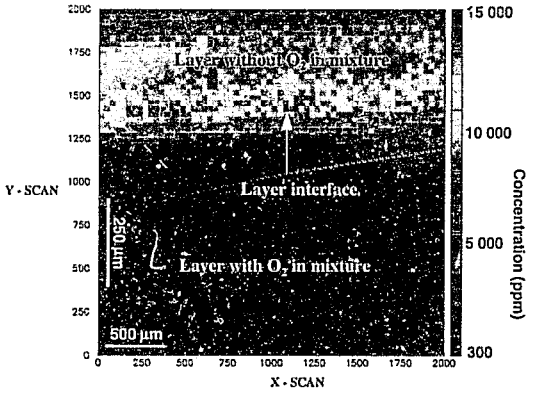

Figure 7.18: Bulk hydrogen concentration of sample 5K051.

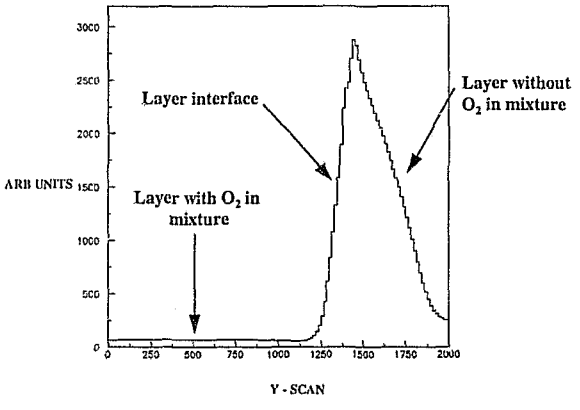

Figure 7.19: Bulk hydrogen concentration of sample 5K051 projected onto the y-axis.

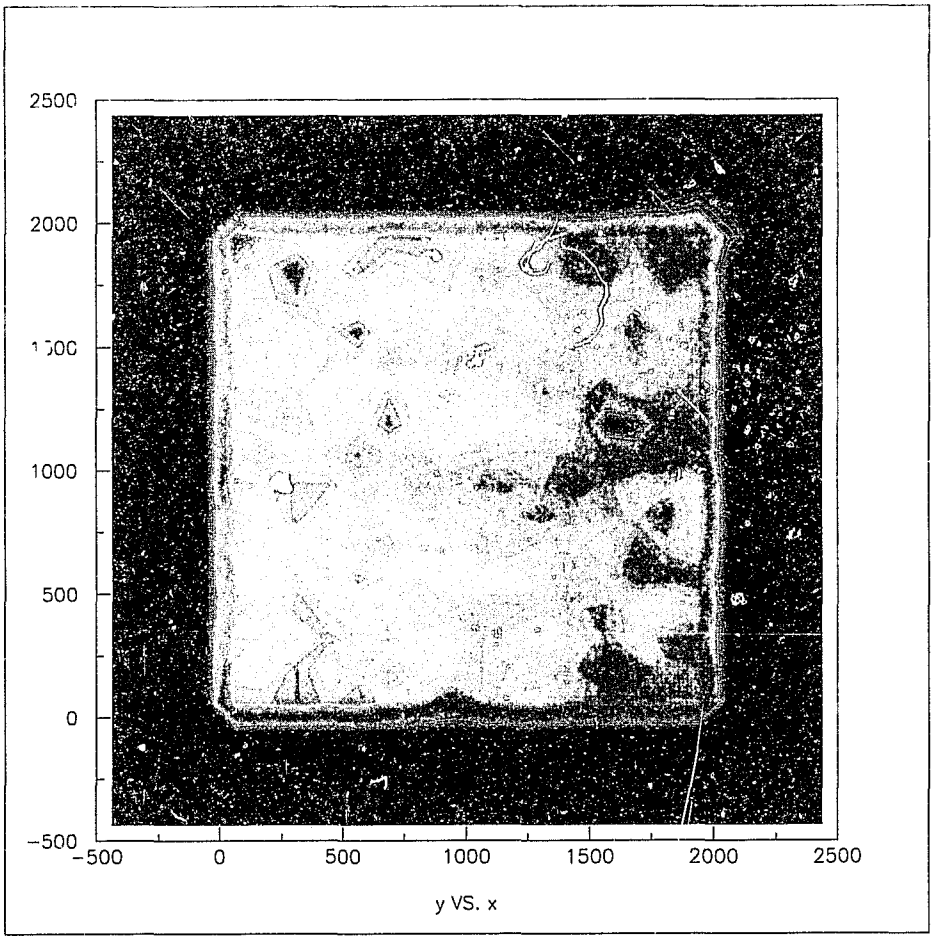

Figure 7.20: 2-dimensional bulk hydrogen distribution of a large grain ($\sim$ 200 μm) PC-CVD diamond (sample NRL 5K051). The inhomogeneity of the hydrogen content can be easily seen. The scale is in μm.

Chapter 8

Discussion

8.1 Hydrogen in diamond

Although the indium studies form the primary thrust of this thesis the hydrogen work is discussed first. This is to lay the groundwork for the later discussions on In-H complexes. Obviously the mobility of hydrogen is an important factor when considering the formation of In-H pairs or complexes.

8.1.1 Hydrogen mobility in diamond

All the experimental work on hydrogen diffusion in diamond in this thesis has dealt with single crystal samples. It is necessary to emphasise this because there are many pos ble diffusion mechanisms for hydrogen in polycrystalline diamond, using various defect pathways such as sp^3 defects and grain boundaries. The previous studies on implanted hydrogen in our laboratory will also be extensively discussed as they form an integral part of this work.

I will briefly review the literature on hydrogen in diamond, emphasizing pertinent

points and omitting work on polycrystalline CVD diamond for the reason given above. This literature has been more extensively covered in Chapter 2 and the reader is referred there for further details.

Theoretically the most stable site for atomic hydrogen (without any pre-existing defects in the lattice), is the bond-centred site (Claxton *et al*, 1986, Estle *et al*, 1987, and Briddon *et al*, 1988), with the H_2^* site (H at a bond-centred site with another H on the corresponding anti-bonding site), being the energetically most favourable configuration for hydrogen in diamond (Briddon *et al*, 1988, and Mehandru *et al*, 1992). It should be noted that molecular hydrogen, although higher in energy, was found to be stable at the tetrahedral interstitial site (Briddon *et al*, 1988), and thought to be important at higher temperatures or in the presence of defects (Mainwood and Stoneham, 1984). Hydrogen species that have been calculated to be particularly mobile in diamond are H^+ with an activation energy of 0.1 eV (Mehandru *et al*, 1992) and H_2 at a tetrahedral interstitial site (0.37 eV - Mainwood and Stoneham, 1984). Calculated activation energies for the diffusion of various hydrogen species are given in Table 8.1. Another point of interest is that the vacancy is calculated to be a trap for up to four hydrogens with an initial binding energy of 5.3 eV for the first, with approximately 1 eV less for each extra hydrogen added (Mehandru *et al*, 1992). Previous experimental results on hydrogen were mentioned in Chapter 2 and will be raised when pertinent in the following discussions.

The mobility of implanted hydrogen

The results presented in Chapter 7, deal with implanted hydrogen in type IIa diamond, which was annealed at 1473 K for 30 minutes. The hydrogen was found to be immobile under these conditions. Both in this work, and in previous studies at the SRCNS (Smallman *et al*, 1996, and Connell *et al*, 1996), implanted hydrogen, at high doses from 3.0×10^{16} to 5.0×10^{16} cm^{-2} at energies between 25 and 50 keV, has been found

Species	Activation energy (eV)	Reference
$H^+_{BC} \rightarrow H^+_{BC}$	0.1	Mehandru and Anderson, 1994
H_2 at a tetrahedral site $\rightarrow$ H_2 at a tetrahedral site	0.37	Mainwood and Stoneham, 1984
$H_T \rightarrow H_T$	1.1	Estreicher *et al*, 1986
$H_{BC} \rightarrow H_{BC}$	1.9	Mehandru *et al*, 1992
$H_T \rightarrow H_{BC}$	2.4	Estle *et al*, 1987
$H^-_{BC} \rightarrow H^-_{BC}$	2.5	Mehandru and Anderson, 1994

Table 8.1: Calculated activation energies for the diffusion of various hydrogen species in diamond in increasing order. H_T is atomic hydrogen at a tetrahedral interstitial site and H_{BC} is bond-centred hydrogen. Unless indicated all species are in a neutral charge state.

to be stable in a number of different diamond types, under anneals of up to 1473 K. This has been seen to be so also when the hydrogen is in the presence of a nearby pre-damaged layer ($\sim$ 700 Å peak to peak in this work and $\sim$ 1600 Å peak to peak in the previous work), which provides a defect-rich region to provide traps with a different shape from the range and damage distribution. The question that remains is, what is (are) the self-trapped configuration(s) that the hydrogen is in?

Very little other experimental work on implanted hydrogen has been performed. This is with the exception of the ESR studies on hydrogen implanted diamond performed by Isoya *et al* (Isoya *et al*, 1993). A possibly significant difference in the ESR work was that the implantations were performed at much higher energies, namely 10 and 45 MeV. Nevertheless the primary defects thought to have been created during implantation were mono-vacancies, as in our low energy implantation work. There must thus also be an equal amount of self-interstitials created. Isoya and co-workers found the

implanted hydrogen to most probably exist in a non-paramagnetic form. In our case, we are then most likely too to be dealing with hydrogen in the same and thus some non-paramagnetic species (even though the hydrogen enters the crystal at a higher energy in the work of Isoya *et al* it loses energy until it is of comparable energy to our work). This immediately rules out simple atomic hydrogen, such as H_T or H_{BC}. We thus firstly concentrate on hydrogen in paired form, be it molecular hydrogen or otherwise. Six possibilities suggest themselves, being molecular hydrogen, H_2^*, the $\{V,H_n\}$ complexes and the $\{I,H_n\}$ complexes with n=2,4 in both cases. Each possibility will be discussed in turn. It must be kept in mind that the depth resolution of our system is approximately 300 Å, so any diffusion of hydrogen less than this distance would not be observed. This is a sufficient distance for individual hydrogen atoms to bond into other hydrogen pairs, with defects or the like.

Molecular hydrogen is thought to be important at high temperatures or in the presence of defects (see previous section). Implantation satisfies one of these criterion: within the implant area there is local heating and we are dealing with a system at elevated temperatures. Before the implanted hydrogen has lost all its energy to the crystal lattice it still has enough energy to form such a complex. It is not very difficult to imagine the creation of H_2 during implantation. As mentioned earlier in this chapter H_2 in a pure diamond lattice is most stable (with regards dissociation), at the tetrahedral site (Mainwood and Stoneham, 1984, and Briddon *et al*, 1988). As also mentioned earlier in this chapter tetrahedrally situated H_2 is calculated to be extremely mobile in this configuration (0.37 eV). Also, upon cooling to room temperature, one would expect the H_2 to dissociate to the more stable atomic form, in the absence of defects. In order for H_2 to exist after cooling, it must then bind to a defect. We will presently only consider extrinsic defects. Intrinsic defects will be discussed later in this section. We look at the two cases:

$$H_2 + V \rightarrow ? \tag{8.1}$$

and

$$H_2 + I \rightarrow ? \tag{8.2}$$

where V is a vacancy and I is a self-interstitial. The only work which has been done with either of these in diamond is that of Mehandru *et al*, where the vacancy was found to trap (and attract) interstitial hydrogen. In the case of two hydrogen atoms the binding energies are 5.3 and 4.4 eV. The C-H bond length is calculated to be 1.05 Å, whereas the H$\cdots$H distance is 1.22 Å, i.e. the H atoms are closer to the carbon atoms than each other and we are no longer dealing with H_2 as a complex (the H-H distance in gaseous H_2 is 0.75 Å). This complex is known as {V,H_2} or {V,H,H}. Calculations on silicon, to which we must refer in this discussion[1], due to the small amount of information known on this system in diamond, have shown the vacancy to dissociate interstitial H_2 to form this complex with a substantial gain in energy (Estreicher *et al*, 1998),

$$V + H_2 \rightarrow \{V, H, H\} + 4.0\,\text{eV} \tag{8.3}$$

The dissociation is caused by the lattice strain associated with the vacancy. A similar effect is seen with the self-interstitial,

$$I + H_2 \rightarrow \{I, H, H\} + 1.7\,\text{eV} \tag{8.4}$$

It is also possible for the two hydrogen atoms to diffuse away and form other complexes, such as H_2^*. As already mentioned H_2^* has been calculated to be the most stable configuration for hydrogen in diamond and is thus a prime candidate for the self-trapping species[2]. The case of two H_2 molecules reacting was also modelled, with the

[1]It is important to remember that calculations on silicon do not always yield results applicable to diamond. They do however serve as a guide. Various calculations also differ from each other so the validity of these calculations must always be carefully considered.

[2]H_2 should be optically active, and is thought to have been observed in proton and deuterium implanted silicon (Holbech *et al*, 1993). Optical (infrared) measurements have as of yet not been carried out on hydrogen implanted diamond, but remain a priority. Apart from H_2, H_2^* should also be optically active.

result

$$H_2 + H_2 \rightarrow \{V, H_4\} + I + 0.06\,\text{eV} \tag{8.5}$$

which led the authors to deduce that such defect generation was unlikely to occur, due to the small amount of energy released. In the presence of a vacancy the formation of $\{V,H_4\}$ i.e.,

$$\{V, H, H\} + H + H \rightarrow \{V, H_4\} \tag{8.6}$$

does not seem to be prohibited, the binding energy of the final hydrogen atom being 2.5 eV (Mehandru *et al*, 1992). Work on the similar system for the self-interstitial (resulting in $\{I,H_4\}$) has not been performed, but seems less likely, just as reaction 8.3 is favoured over 8.4 above.

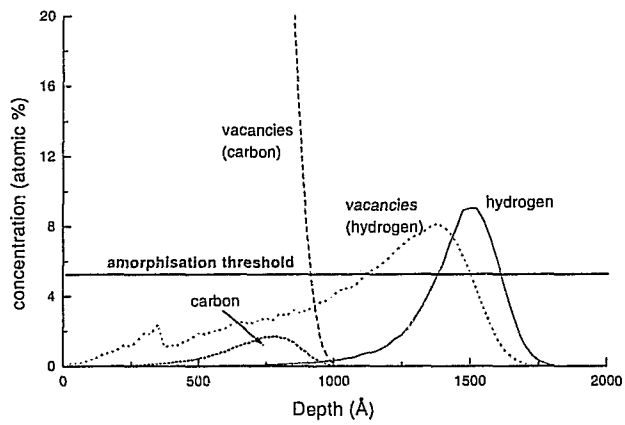

Figure 8.1: TRIM98 simulation of the resultant hydrogen, carbon and vacancy distributions after a 1×10^{16} ions.cm^{-2} 50 keV ^{12}C and a 5×10^{16} ions.cm^{-2} 25 keV ^{1}H implant. The amorphisation threshold is at 10^{22} vacancies.cm^{-3}.

TRIM98 calculations for hydrogen implantation energies of 25 and 50 keV, the energies used in the various experiments, along with the corresponding carbon implants

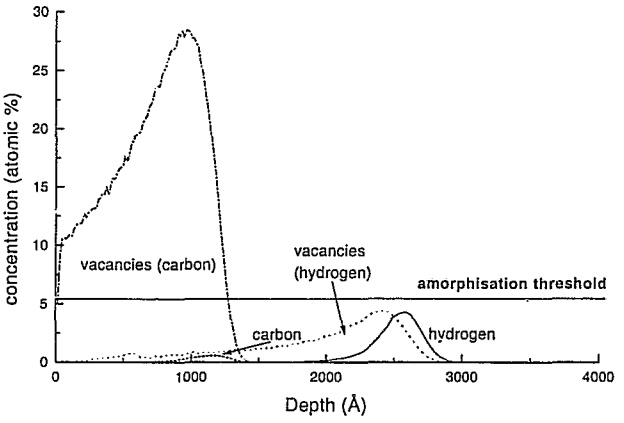

Figure 8.2: TRIM98 simulation of the resultant hydrogen, carbon and vacancy distributions after a 4×10^{15} ions.cm^{-2} 80 keV ^{12}C and a 3×10^{16} ions.cm^{-2} 50 keV ^{1}H implant. The amorphisation threshold is at 10^{22} vacancies.cm^{-3}.

at 50 and 80 keV respectively, have been made and are shown in Figures 8.1 and 8.2. These implants yield 2.0 and 2.4 vacancies per implanted ion respectively. However, vacancy-self-interstitial recombination is a common process, even at room temperature (see Chapter 2). This loss in the number of vacancies and interstitials favours the formation of paired hydrogen complexes over single hydrogen ones (at the annealing temperatures ~1473 K used in this work), as the {V,H,H} and {I,H,H} complexes require half as many vacancies or interstitials as single-hydrogen-vacancy and single-hydrogen-interstitial complexes respectively, and H_2^* requires none. What also must be considered is the possibility that either the created vacancies or the interstitials could possess some net charge. They would thus more easily attract the implanted H^+, unless the hydrogen was able to capture an electron from the crystal lattice.

In the measurements performed in this work a shallow pre-damaged layer was created in order to see if diffusion to this layer occurred i.e. if the vacancies or the self-interstitials

provided a sink for diffusing hydrogen. This proved not to be the case. Another possibility not previously considered is that the vacancies or the interstitials (we recall that the activation energy of the interstitial is reported at 1.3 eV and that of the vacancy at 1.7 or 2.3 eV), become mobile before the hydrogen in the anneal, diffuse to the hydrogen and form immobile species. The damage was made using carbon ions, which also increases the interstitial concentration. This hypothesis is discounted by the previous work in our laboratory (Smallman *et al*, 1996, and Connell *et al*, 1996), where a control measurement without a pre-damaged layer was made. Again no diffusion of hydrogen was observed. The pre-damaged layer is thus not a necessary condition for the hydrogen immobility.

We now consider various possible impurity-hydrogen complexes that could form. Apart from hydrogen a major impurity in diamond, both natural and synthetic HPHT, is nitrogen. Thus it is a prime candidate for a hydrogen trap. The previous work on implanted hydrogen used nitrogen-rich samples, namely a type Ia and a type Ib. We used a type IIa diamond which is nitrogen free, to the limits of IR detection (< 1-2 ppm (atomic)). However, Sellschop and co-workers showed that the total nitrogen content of diamond samples, as determined by nuclear methods which are independent of bonding configuration and thus yield the entire nitrogen content, was found to be higher than that measured by IR spectroscopy (Sellschop, 1992). In the case of a suite of type IIa samples the nitrogen content was found to be in the range 4-40 ppm (atomic). This is adequate to be considered as a possible major trapping site for hydrogen. The three diamond types in question, type Ia, Ib and IIa will now be discussed in turn. Unfortunately data on hydrogen implanted type IIb diamond does not yet exist.

In type Ia diamond the primary nitrogen defects are the A and B centres, discussed in Chapter 2, and whose proposed structures are shown in Figure 2.2. Theoretical calculations have shown the A centre to be a trap for hydrogen, with H^+ having a binding energy of 4.2 eV and neutral hydrogen having a lower binding energy of around 2.4 eV

(Goss *et al*, 1997). The hydrogen atom is found to sit on the trigonal axis, midway between the two nitrogens, with a N-H separation of approximately 1.1 Å. Most recently μSR measurements, along with theoretical calculations, have indicated that muonium, which one treats as a chemical isotope of hydrogen, is trapped at a nitrogen centre, thought to be an A centre (Machi *et al*, 1999). In these calculations the muonium was found to lie approximately 9° off the N-N axis. The species found experimentally was however in a paramagnetic state, which conflicts with that of implanted hydrogen. One can also consider the possibility of H_2 forming in an A centre or, more likely a complex {2N,2H} where each hydrogen is more closely bound to the respective nitrogen atoms than each other. The stability of such a configuration is still to be calculated. No theoretical work has been done on the stability of hydrogen in the B centre. However, as can be seen in Figure 2.2, the B centre is thought to consist of four nitrogen atoms surrounding a vacancy. Thus it seems probable that species similar to the $\{V,H_n\}$ configurations could occur, which we shall denote as $\{4N,H_n\}$. Another fraction detected in the μSR measurements of Machi and co-workers was the muon in a diamagnetic, positive charge state. H^+ bonding with either an A or a B centre would form such a complex.

Type Ib diamond is that which contains nitrogen in the form of single substitutional centres. Calculations have shown hydrogen in all charge states to bind strongly to substitutional nitrogen (Mehandru and Anderson, 1994). Hydrogen was calculated to have a binding energy of 1.49 eV when occupying the BI (bond-inserted) site. This configuration is shown in Figure 8.3. The BI site was found to to be the most stable of those considered in the calculations.

It has been established that type IIa diamond has a certain (4-40 ppm) concentration of nitrogen. However, this nitrogen is optically inactive, and the configuration(s) that it occupies is (are) unknown. At present it has not been determined, neither experimentally nor theoretically, whether it does act as a hydrogen trap or not.

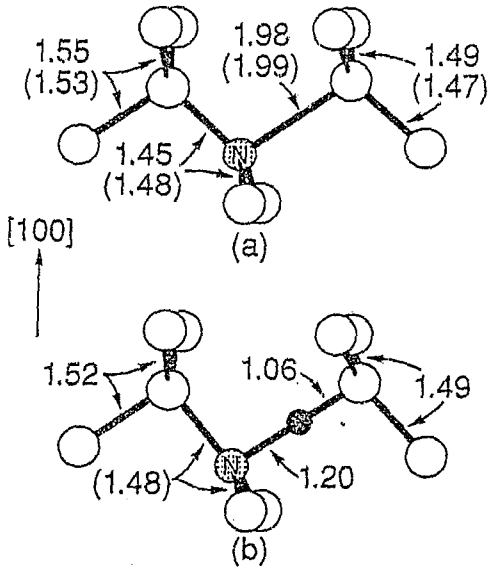

Figure 8.3: (a) Calculated structure around a substitutional nitrogen atom in diamond (from Mehandru and Anderson, 1994). The numbers in parentheses are for a different cluster size. (b) The most stable configuration for atomic hydrogen near a substitutional nitrogen atom. The hydrogen occupies the bond-inserted (BI) site.

Optical studies on type Ia diamonds discovered two absorption peaks at 3107 cm^{-1} and at 1405 cm^{-1} (Chrenko *et al*, 1967, and Runciman and Carter, 1971). These peaks were found not to exist in type II diamonds. Their existence has been interpreted as being due to a C-H stretch vibration (Woods and Collins, 1983)[3]. The 3107 cm^{-1} peak was thought not be due to nitrogen, as doping with ^{15}N did not cause any shift in wavenumber. A recent paper (Kiflawi *et al*, 1996), found the occurrence of this peak in HPHT type Ib diamonds after high temperature annealing (2100 °C with a 9 GPa stabilising pressure). In diamonds with nitrogen content (as measured by op-

[3]As mentioned in Chapter 2 the strength of the 3107 cm^{-1} peak was found not to correlate with the total hydrogen concentration.

tical methods) < 150 ppm the peak was not detected. In one of the samples studied the strength of the peak was found to correlate with the nitrogen content at various parts of the sample. No definite correlation between nitrogen concentration and peak strength between the samples was found. Kiflawi and co-workers speculated that the correlation found in the particular sample was due to the same conditions favouring the incorporation of nitrogen and hydrogen into the sample during genesis. What has not however been considered is that this optical centre could involve carbon, hydrogen and nitrogen (and vacancies). This would better explain the observed facts[4]. In Figure 8.4 two possible configurations involving hydrogen and the A and B centres respectively are shown. For nitrogen present in single substitutional form the hydrogen could go bond-inserted (BI) between the nitrogen and one of the four carbon atoms surrounding it. The samples used in the Woods and Collins study were mostly type Ia, although some showed Ib characteristics. Kiflawi *et al* used type Ib samples, but annealing at high temperatures is known to cause the aggregation of single substitutional nitrogen to form A and B centres (Evans *et al*, 1981). Thus one can not be certain of which centre, possibly coupled with hydrogen, is responsible for the 3107 cm^{-1} peak.

The third possibility, after paired hydrogen (with or without vacancies), and hydrogen-nitrogen complexes, for a sink for hydrogen, is dislocations. These are often ignored as defects in single crystal diamond, but a network of dislocations and defects are known to be common in diamond crystals (see Field, 1979). Other methods which yield information on the quality of the crystals, such as high energy (few hundred GeV) channeling, do not detect these dislocations, a possible reason for their dismissal in the literature until now. In Chapter 2 the presence of hydrogen at grain boundaries and extended defects has been discussed. Such defects, present in single crystal diamonds, would thus provide a barrier to hydrogen diffusion.

[4]Kiflawi *et al* also observed the 3107 cm^{-1} peak in electron irradiated samples. Since hydrogen and nitrogen are present in the Ib samples studied this irradiation may have introduced energy to allow hydrogen-nitrogen-carbon complexes to form. The possibility of this peak being vacancy related must also be considered.

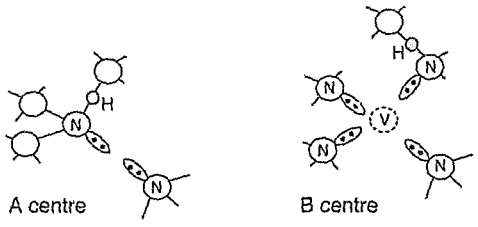

Figure 8.4: Proposed models for the defect responsible for the 3107 cm^{-1} absorption line in nitrogen-rich diamonds. The B centre contains a vacancy, which agrees with the observation of this absorption line in electron irradiated diamonds.

What must be kept in mind is that in all probability the implanted hydrogen exists in a few different species, the majority of which are immobile. An overriding factor in the measurements is that the hydrogen implants were **high dose**. In Figure 8.5 the measured hydrogen content is seen to have a maximum of nearly 5% (atomic), (which equates to 50 000ppm). This immediately discounts nitrogen as a major trapping centre in this system[5]. Dislocations can also be ruled out as primary trapping centres since, although plentiful, large scale aggregation of hydrogen at these should lead to structure in the 3-dimensional ERDA measurements (within the limits of the technique), which has not been observed. The only defects of sufficient number to trap the very high concentrations of implanted hydrogen must be the extrinsic defects introduced during implantation: the vacancies and interstitials. This conclusion is given weight by the experimental depth distribution, which in Figure 8.5 is seen to correlate

[5]The range of nitrogen concentrations found in diamond is listed in Section 2.2 and has been found to have a maximum of 5000 ppm.

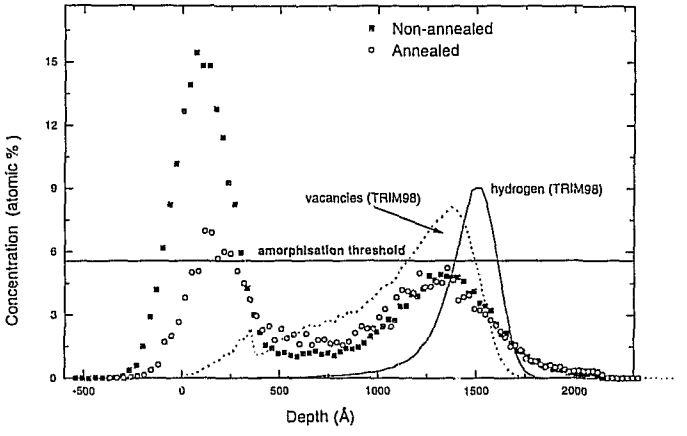

Figure 8.5: The hydrogen depth distribution of the implanted type IIa diamond by ERDA, along with the TRIM98 simulation of the implant. The measured implant is seen to correlate with the calculated vacancy distribution.

with the calculated vacancy peak due to the hydrogen implantation. The experimental data is seen to extend deeper than the vacancies into the bulk. This is for two reasons. Firstly the effect of energy straggling and multiple scattering, which are detailed in Chapter 6, is to broaden the measured peak and to lower the energy of some hydrogen recoils to appear as if they originated from deeper in the bulk. Secondly the other, lower dose trapping mechanisms discussed in this section would contribute to this "tailing" of the peak (through rendering immobile some of the implanted hydrogen before it could diffuse to the vacancies/interstitials).

Thus it would appear as if the hydrogen is being trapped in high concentrations of vacancies or interstitials. Such high concentrations could result in the formation of complex agglomerates which would then it seems be massive traps for hydrogen. Such agglomerates, if present beyond a certain concentration, result in the irreversible amorphisation of the diamond in that region i.e. the carbon transforms into an amorphous

or graphitic phase. A number of studies have focussed on what this *amorphisation threshold* might be, implanting diamond with different ions at various energies to establish a critical dose, for example see Spits *et al*, 1994. More recently, Uzan-Saguy and co-workers, using both their work and published literature, have deduced a general amorphisation threshold independent of ion species or energy (Uzan-Saguy *et al*, 1995). This threshold is given as 10^{22} vacancies.cm^{-3}. The amorphisation threshold is indicated for these and the previous measurements in Figures 8.1, 8.2 and 8.5. Of importance is that the 25 keV implant exceeded the amorphisation threshold between 1100 and 1500 Å and the 50 keV implant was approximately 80% of the amorphisation threshold at the vacancy peak. In the case of the 25 keV implant the hydrogen is seen to primarily occupy the area with damage above the amorphisation threshold, with the usual broadening due to kinematical mechanisms (as mentioned in the previous paragraph). It is possible that the diamond was amorphised during implantation and the hydrogen has occupied this graphitised area. However, in the above paper, variation in the values determined for the amorphisation threshold was seen, with values up to 4 $\times$ 10^{22} vacancies.cm^{-3} being obtained. It cannot then be assumed that amorphisation did occur[6]. Upon annealing (1473 K, normal pressure), the sample, which was visibly discoloured after implantation, was seen to lose this discolouration. In the lower dose 50 keV implants it is similarly not clear whether amorphisation occurred and the vacancy/self-interstitial models discussed in this chapter must not be discounted. These as well as the other trapping mechanisms discussed, namely nitrogen and dislocations, remain probable trapping sites at lower doses.

[6]It would be most useful to employ a technique such as Electron Spectroscopy for Chemical Analysis (ESCA) or Raman spectroscopy to measure whether amorphisation has occurred.

Plasma-assisted diffusion of hydrogen

The ERDA measurements performed to investigate plasma induced diffusion of hydrogen into diamond, outlined in Section 7.3.4, were on a type IIa diamond[7]. This is an important fact to note as other workers have shown the mobility of plasma loaded H^+ in p-type semiconducting type IIb diamond (Chevallier *et al*, 1998). In a non-semiconducting diamond we assume that we are dealing with neutral hydrogen. Even if it enters the lattice as H^+, capture of an electron should be rapid. The only previous study of neutral hydrogen diffusion which measured the resultant hydrogen profile after exposure to a plasma was the work of Popovici *et al* (Popovici *et al*, 1995). As earlier discussed some doubts have been cast on this work, due to the sample having a low crystal quality i.e. a large number of imperfections. The data taken after the various treatments is again shown in Figures 8.6 to 8.10 (now in linear form), along with the data obtained by Popovici and co-workers. These treatments were 1) freshly cleaned, virgin diamond, 2) hydrogen plasma exposure, 3) damage through ion implantation, 4) hydrogen plasma exposure and 5) high temperature anneal. The steps are fully detailed in Section 7.3.4. As also noted in that section the data exhibited the following interesting features:

- the surface peak width increased significantly after the first hydrogen plasma treatment. This broadening was not observed neither after the other plasma treatment nor after any of the other steps that the diamond underwent. Thus it does seem most likely that some unexpected event that deposited hydrogen on the surface did occur. Of these the most likely would be either a vacuum fluctuation in which pump oil or the like was deposited on the surface[8], or perhaps the sample surface was accidentally contaminated during transport to or from the plasma

[7]The (100) surface was used. Although the different surfaces have different atomic configurations this is not thought to be a deciding factor in the diffusion process. Theoretical calculations of the barrier to hydrogen diffusion for the different surfaces would greatly illuminate the situation.

[8]As mentioned in Chapter 7 hydrogen, in various forms such as water and hydrocarbons, is known to ~rete onto the surface of samples, even under high vacuum $\sim 10^{-6}$ Torr.

oven or during mounting

- plasma treatment of the clean diamond does not result in any observable movement of hydrogen into the bulk. The ion-damaged diamond was exposed to atmosphere for several minutes before being measured (prior to the second plasma treatment). No increase in bulk hydrogen was measured. Measurement after the second plasma treatment, after the damage via ion implantation, showed a definite indication of hydrogen loading of the bulk. This hydrogen distribution was found to peak slightly deeper than the damage peak calculated by TRIM98, as can be seen in Figure 8.9. This is discussed below

- annealing of the hydrogen-loaded diamond (1473 K, normal pressure), caused a reduction in the amount of bulk hydrogen. The peak diminished but was still visible. This fact is also part of the discussion below.

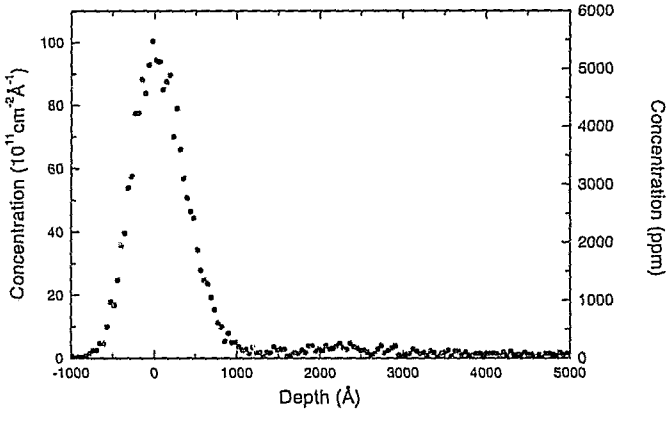

Figure 8.6: ERDA spectrum of the pure, virgin IIa diamond.

The data thus indicates that may be possible to load hydrogen into type IIa diamond under the conditions discussed earlier, but only in the presence of a pre-damaged layer (since this measurement is part of a preliminary study and has not yet been repeated it

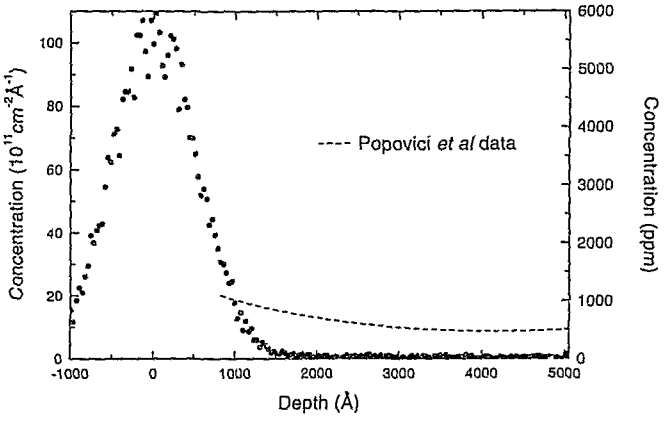

Figure 8.7: ERDA spectrum of the IIa diamond after the first hydrogen plasma treatment. The data of Popovici *et al* is also indicated.

is important to note that the following discussion does contain a speculative element). By a pre-damaged layer (as in the previous section), we refer to the presence of vacancies and self-interstitials, both singly and in complexes, as well as of the implanted atoms which were the cause of this damage, in this case neon. In Figure 8.11 the measured hydrogen distribution after the second plasma treatment is shown, along with the calculated implanted neon distribution. Although the measured hydrogen correlates better with the calculated neon distribution than with the calculated vacancy peak, the formation of Ne-H pairs or complexes is deemed unlikely. This is due to the chemical stability of neon, being a group VIII element. It is important to remember that we are using a technique with a detection limit of approximately 100 atomic ppm. Thus we can only detect mechanisms which singly or in combination result in a movement of hydrogen above this level.

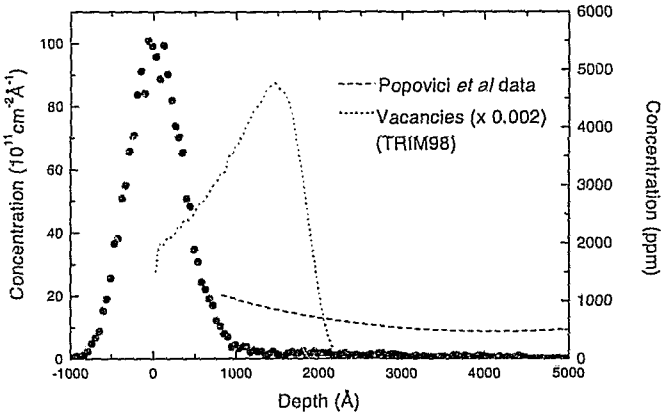

Figure 8.8: ERDA spectrum after implantation with 170 keV, 2×10^{16} ions cm^{-2} neon at room temperature to cause vacancy creation. The vacancy distribution due to the neon implantation, as calculated by TRIM98, is also shown, as is the data of Popovici *et al.*

The damage layer created by the implantation does exceed the amorphisation threshold calculated in the previous section, from very near the surface[9] to approximately 2200 Å. This is of great interest as one would expect amorphised diamond to allow the diffusion of hydrogen. We deduce this from the work of Vainonen and co-workers which showed the mobility of hydrogen (both implanted and co-deposited during growth), in diamond-like carbon (DLC) films (Vainonen *et al*, 1997). The carbon bonding ratio in this case was sp^3/sp^2=70%, which would most probably not be dissimilar to that of the amorphised carbon. ESCA measurements of the damaged diamond would again prove most useful to determine the bonding ratios in the damaged layer. We must thus consider the possibility that irreversible amorphisation of the diamond might well not have occurred, in conflict with the work of Uzan-Saguy *et al* cited in the previous section. This issue is not however of vital importance in this discussion as plasma loaded

[9]Near surface TRIM98 simulations give this value at 1.8 Å. The importance of the accuracy of this value, which is of the order of the lattice spacing, will be discussed further on.

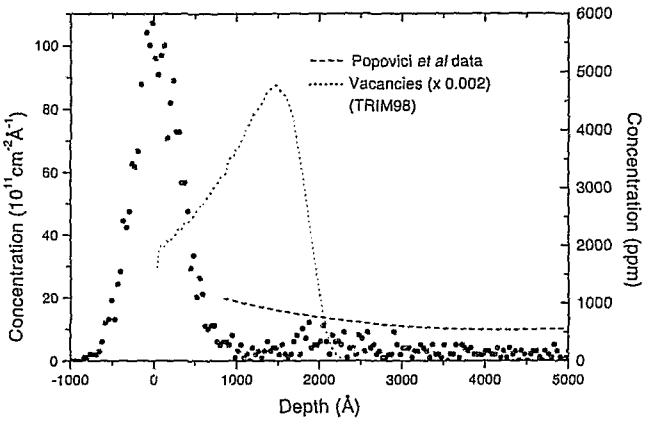

Figure 8.9: ERDA spectrum of the IIa diamond after the second hydrogen plasma treatment. Note the increase in bulk hydrogen, peaking just below 2000 Å. The data of Popovici et al is also indicated, as is the vacancy distribution calculated by TRIM98.

hydrogen was detected after the second plasma treatment at depths much greater than the 2200 Å calculated to be the limit of the amorphisation. This was the case up to 5000 Å (see Figure 7.13), the maximum depth that was probed in these measurements (low-energy carbon recoils striking the detector limited us to this depth). This is also outside the limit of any errors expected in the range calculated by TRIM98.

In fact the data raises suspicion that the vacancy peak calculated by TRIM98 is at too shallow a depth, as evidenced by the observed hydrogen peak in Figure 8.9 just below 2000 Å (even considering the 300 Å depth resolution of the system). In the previous section on implanted hydrogen the hydrogen distribution was found to correlate with that of its own damage layer. The other damage layer in that case was by carbon ions. TRIM98 uses tables of stopping powers from the literature in its Monte Carlo simulations. In order to check for any possible errors in these it would be advantageous to perform both the hydrogen implant and plasma work using the same ion to create the

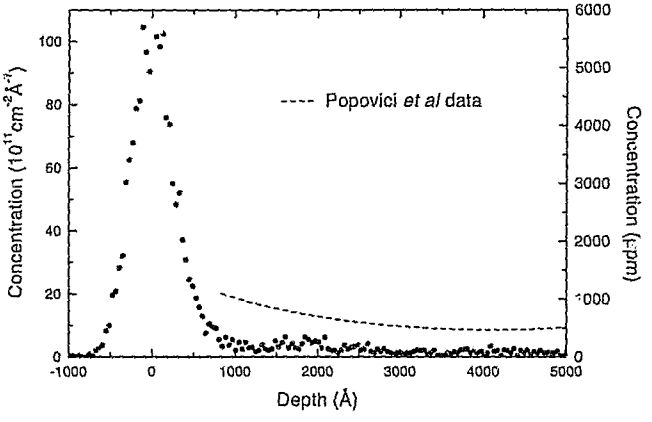

Figure 8.10: ERDA spectrum of the IIa diamond after the 1500 K anneal. The bulk hydrogen still remains.

damage at the same depths. This fact has only been realised after the detailed analysis of the measurements. Reference of the literature has revealed that stopping powers can often be out by 10-20% (Sigmund, 1997, Sigmund and Glazov, 1998, and Ziegler, 1998).

If one looks at the logarithmic plots of the hydrogen distributions of the virgin sample and the sample after the first hydrogen plasma treatment (Figures 7.10 and 7.11), it is noticed that the virgin sample has a noticeably higher hydrogen concentration than after the plasma treatment. It is thought that the measured hydrogen concentration in the virgin diamond is the naturally occurring hydrogen from genesis (Sellschop, 1979). The heating of the diamond during the plasma treatment could cause this hydrogen to become mobile depending on the configurations that the hydrogen is in. If we assume that the surface barrier to diffusion is lower for out-diffusion than in-diffusion then the hydrogen could escape from the diamond.

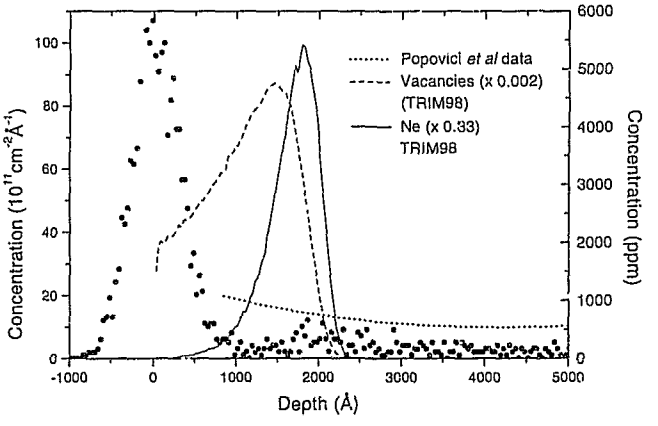

Figure 8.11: ERDA spectrum of the IIa diamond after the second hydrogen plasma treatment, showing the calculated neon distribution.

The surface of diamond is damaged, just as the bulk is, by ion implantation. Similarly to the bulk it also has an amorphisation threshold. We can assume that if the near surface bulk and the surface are amorphised, then the surface atoms will not be able to reform into the diamond structure. Thus, in this study, where we have calculated a near surface vacancy concentration well above the amorphisation threshold, we deduce a resultant amorphised surface. TRIM98 results have been presented which indicate amorphised diamond up to the layer of atoms just below the surface. As long as these TRIM98 values are correct sufficiently close to the surface, say three or four atomic layers, then we assume an amorphised surface (or at least partially so). Three or four atomic layers from the surface we deal basically with the bulk, so there is no reason not to believe the validity of the TRIM98 calculations. Even if irreversible amorphisation hasn't occurred, the possibility of which was raised earlier in this section, the surface has been extensively damaged and this damage can only be reversed by high temperature annealing (1473 K, normal pressure is sufficient).

Another cause of surface damage is sputtering, which should also be kept in mind. Apart from this the effect of sputtering would be to "move" the position of the surface inwards, thus effectively decreasing the depth of the implant over time. TRIM98 simulations were made in order to measure this effect. For the neon energy and dose used in these measurements the diamond layer remove by sputtering was found to be less than 4 Å.

Exposure of this damaged surface to atmosphere results in the accretion of hydrogen in its various forms, as discussed. This hydrogen is not seen to noticeably diffuse into the bulk. Hydrogen plasma treatment is thought to remove the hydrogen off the surface, leaving a clean atomic carbon layer, terminated by a monolayer of hydrogen atoms (Butler, 1996). The second plasma treatment caused this cleaning of the surface (as did the first). In the case of the second treatment a perfectly constructed diamond surface did not remain, but rather a mass of surface defects resulting from the damage. It is easy to think of this surface being more permeable to in-diffusing hydrogen than the normal diamond surface, with some of the created defects forming pathways into the bulk. This theory is backed up by the study of the 3-dimensional ERDA measurements on the hydrogen-implanted diamonds. In both this work and earlier studies (Connell *et al*, 1996), ERDA measurements have shown the presence of a hydrogen-rich region corresponding to the implant area on the surface of the diamond. This hydrogen is not implanted hydrogen, as the region between the surface and the implant does not show any such hydrogen-rich region. It must thus be due to damage of the surface which allows a little hydrogen to (once past the accreted hydrocarbon layers), move into the first few atomic layers of the diamond. In this work the sample was not annealed, so the damage caused by the hydrogen implantation was not annealed out.

If surface hydrogen can diffuse into the subsurface of damaged diamond, why does it not then appear to move deeper into the bulk? This immobility is opposite to the plasma treatment, where the hydrogen continues to diffuse further into the diamond.

There are a number of differences between these two systems. The major ones are kinetic energy, charge state and concentration. The hydrogen ions of the plasma have a high kinetic energy. Passage into the diamond does not remove this energy, allowing them to pass over potential energy barriers. Before capture of a lattice electron the positive ion is as calculated, extremely mobile, especially when compared to its neutral form. The plasma is also a source of a many orders of magnitude higher concentration of hydrogen which strikes the surface (than that which accretes). We thus have a highly energetic, high flux of mobile hydrogen incident on a damaged surface. The resultant diffusion (if real), is perhaps not that surprising.

We also consider the differences between the plasma loading of hydrogen and its implantation. What is the differentiating factor? Implanted hydrogen, once it has lost enough energy to be incapable of creating damage in the lattice (we recall the displacement energy of 35±5 eV), still has enough energy to move freely around the crystal until this energy is lost. In this way it should be very similar to plasma loaded hydrogen which has permeated the surface barrier. Unfortunately it is very difficult to compare the results of the implanted work with those of the plasma loaded work. This is because, as stressed in the previous section, the implant work was high dose ($\sim$ 50 000 ppm). Thus an effect of the order of 550 ppm (above the detection limit), as observed after the second plasma loading (see Figure 7.13), would be very unlikely to be observed.

In Section 7.3.4 the hypothesis of a vacancy-assisted mechanism for the incorporation of hydrogen deep into the bulk was proposed. Vacancies have been nominated as deep-lying donors by a number of authors (Dyer and Ferdinando, 1966, Collins *et al*, 1969, and Vermeulen and Farrer, 1975). Donors however give electrons, thus converting H^+ into neutral H and lowering the mobility. In the previous section it was also extensively discussed how vacancies were traps for diffusing hydrogen. There is no solid evidence that the vacancies are needed for the plasma loaded diffusion. The purpose of the pre-damage is thought to be only to lower the surface barrier to diffusion. It was pos-

tulated in Section 7.3.4 that, upon annealing, hydrogen left the diamond through the same vacancy assisted mechanism. Due to vacancy-self-interstitial recombination the process was limited and some hydrogen remained in the bulk. Since vacancies are no longer thought to be involved in the diffusion process it seems likely that the hydrogen that remains after annealing is trapped at some stable configuration(s), probably those discussed in the previous section. That which diffuses out occupied some less stable configuration(s) prior to annealing.

At first glance it appears difficult to reconcile our results with those of Popovici *et al.* In Figure 8.9 the diffusion measured by Popovici and co-workers is seen to be measurably higher. Not only this but the Popovici sample was not pre-damaged in any manner. There are however three points which allow our result not to conflict with that of Popovici *et al.* Firstly, although not pre-damaged, the sample used by Popovici and co-workers was, as already discussed in Chapter 2, considered to be of poor crystal quality, that is rich in dislocations and other extended defects. These defects, some of which would be incident to the surface, would serve as a mechanism to bypass the surface barrier to diffusion, as well as serving as diffusion pathways through the crystal. Secondly, the Popovici diamond was not measured before exposure to the plasma. Thus the results include the baseline of hydrogen already present in the diamond. Natural diamond has been determined to have an intrinsic hydrogen concentration from 500-3600 ppm (atomic) with no type dependence (Connell *et al*, 1998). This result has been made by studying a number of diamond samples, some of which were part of this thesis. Thirdly, the Popovici sample was exposed to the plasma for an hour, whereas our second plasma exposure was only 20 minutes. The exact conditions of the individual plasmas would also have differed somewhat. One can conclude that the two sets of results may indeed correlate.

8.1.2 Hydrogen distributions in diamond

We mentioned in the previous section that the diffusion results obtained by Popovici *et al* were too high because the sample was not measured before plasma exposure. Thus the intrinsic hydrogen concentration of the sample was not known. The measurement of a number of natural diamond samples over many years in our laboratory, such as the IIa diamond used in the plasma work, has yielded the range of intrinsic hydrogen concentrations mentioned above : 500-3600 ppm. As mentioned this range was found to have no type dependence. Beyond this the hydrogen distributions were found to sometimes be inhomogeneous. The sample discussed in Section 7.3.5 is an extreme example of this, with optically visible "clouds" being apparent. The concentration in these clouds was found to increase up to approximately 5000 ppm close to the surface.

In the CVD sample studied in Section 7.3.6 and in similar samples also studied the hydrogen concentration was found to be inhomogeneous. Hydrogen content is very dependent on growth conditions in CVD diamonds. For the part of the 5K051 sample grown with oxygen in the mixture the hydrogen concentration was found to be below the detection limit of the system i.e. < 100 ppm. This is an important result as the reduction of hydrogen content is a goal of the CVD diamond growth community. The oxygen is thought to serve two purposes. In the form of OH it converts sp^2 to sp^3 bonds. It also scavenges sp^2 impurities in a superior manner to atomic hydrogen, as well as reducing hydrocarbons on the surface which may be incorporated into the bulk.

The importance of intrinsic hydrogen distributions must be noted. Any doping of diamond runs the risk of passivation of the donors/acceptors by this reservoir of hydrogen. Even if the hydrogen is present in a stable trapped form the damage and energy introduced in the implantation spike may liberate it to interact with the dopant. This important consideration will be further discussed in the indium in diamond discussion later in this chapter.

8.2 Indium in diamond

The 2-dimensional CEEC measurements performed in this thesis are the first to investigate ^{111}In in defect-rich diamonds, and thus also the possibility of complexation of the In with any these defects. Coupled with the theoretical investigations we are able to deduce new information on the configurations involved in the In in diamond system. The fractions obtained for the best fits to the experimental data are shown in Table 4.3. The most favoured sites were a combination of substitutional (with a 0.034 Å vibrational amplitude[10]), and a site approximately 60% of the way (~0.45 Å), from substitutional to bond-centred along the ⟨111⟩ axis (which we previously defined as S-BC(0.6)). In previous results the majority of In atoms were found to favour near-substitutional sites. We have been able to distinguish two distinct fractions, one the ideal substitutional site and the other the S-BC(0.6) site. This new insight is due to the added information in the 2-dimensional data collected. Combinations of pure substitutional and random fractions (as in previous work), were fitted, but did not yield as good a fit. This is shown in Figure 8.12 for the IIb post-anneal sample (the experimental data and the best fits are in Figure 4.13). The low yield of planar (100) channeling effects seen in this data as opposed to the other axial directions is also a good indication of a population of the emitters moving off-substitutional.

The basis for the errors for the obtained fractions is given in Section 4.4. Within these errors the fractions are seen to be nearly identical for all samples, independent of defect concentration, and therefore diamond type. This does not exclude specific In-defect complexation with boron, nitrogen or hydrogen. Rather if such complexation does occur, it does not affect the In lattice site enough to influence its channeling spectra i.e. less than 0.1 Å displacement of the In lattice site from sample to sample takes place. If the In was forming different complexes then different sites would be occupied and these different fractions would be detected. The tendency for a significant

[10] As detailed in Chapter 4 the vibrational amplitude is an isotropic distribution around the given site, and must be differentiated from an off-site displacement in a given direction.

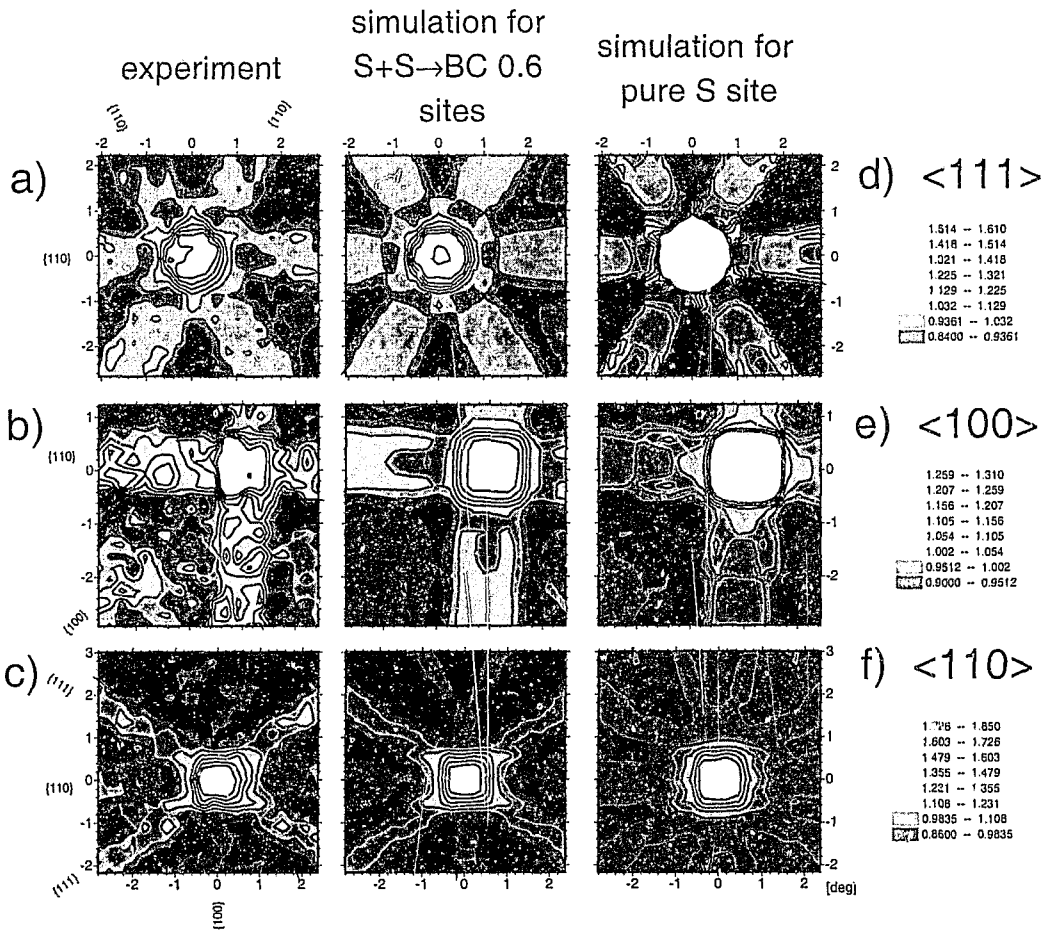

Figure 8.12: Calculated fits to the experimental data for the IIb post-anneal sample using firstly a pure substitutional fraction plus a random component, and secondly a purely bond-centred fraction plus a random component.

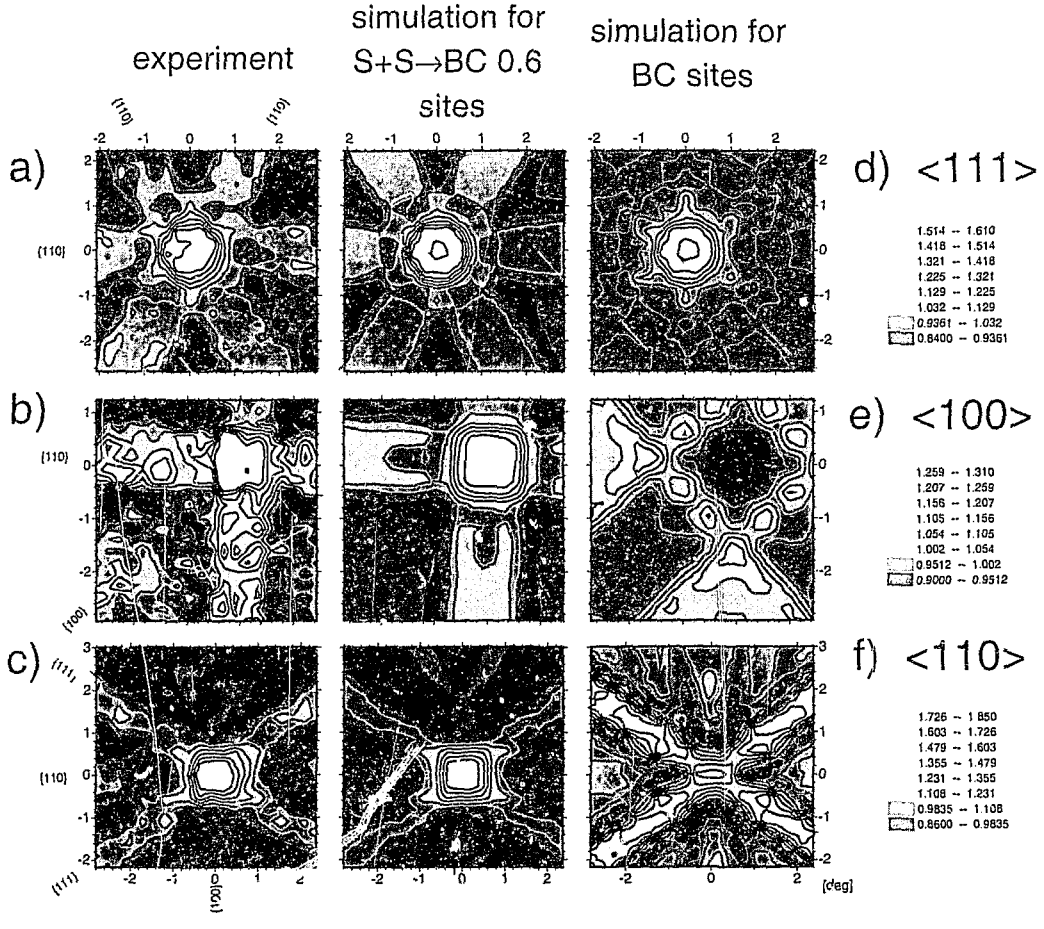

Figure 8.13: Calculated fits to the experimental data for the IIb post-anneal sample using firstly a pure substitutional fraction plus a random component, and secondly a purely bond-centred fraction plus a random component.

fraction of the In to be off-substitutional concurs with earlier observations of defects near the In lattice site (Burchard *et al*, 1993, and Bharuth-Ram *et al*, 1996), which have the effect of breaking the symmetry of the lattice, thus generating an off-centre equilibrium In position. However, in order for the S-BC(0.6) site to exist, some sort of defect must be present to create this asymmetrical configuration. No theoretical modelling of this site has ever been performed. A distinct possibility is that the In forms complexes with implantation-induced defects involving vacancies, self-interstitials or possibly both. These could then dominate the In-defect formation process. It is known that large ions which are not charged (and thus the Coulombic interaction is absent), are prone to attract vacancies through elastic interaction, whereas small ions attract self-interstitials (Frank, 1991). Therefore In-vacancy complexes are probably favoured over self-interstitial ones. In the case of the IIb sample the difference in Fermi level is seen not to have a measurable effect. In silicon, Cd-H pairs (the method used measured the structural properties after the transmutation from ^{111}In), were found to exist in different charge states, the populations of which were found to depend on the Fermi level and the free hole concentration (Skudlik *et al*, 1992b). The charge state was implied not to affect the In/Cd lattice site in silicon.

The importance of vacancies in the doping of diamond has been previously documented (Prins, 1988, and Prins, 1993a). Theoretical studies have indicated that these might limit the ability to dope diamond with heavy n-type ions, through the formation of dopant-vacancy acceptor complexes (Jones *et al*, 1996). Studies on In in germanium have shown the formation of both In-vacancy and In-self-interstitial complexes (Feuser *et al*, 1990, Haesslein *et al*, 1994, and Haesslein *et al*, 1998), with acceptor and donor properties respectively being suggested (Haesslein *et al*, 1998). The existence of different charge states of the In-vacancy complex in germanium is also proposed (Haesslein *et al*, 1994). The authors of these papers have all suggested that single vacancies were involved, although no reasons were given for two or more vacancies not being constituents of the complex.

We now consider the vacancy-In-vacancy complex calculated in Chapter 5. This is a bond-centred site between two vacancies. To first order we treat this site purely as bond-centred. This is because the emitted electrons in the CEEC technique are relatively insensitive to the local atomic configuration and are dominantly dependent on the geometric location of the emitter atom. The bond-centred site was tried in the fitting procedure and was found not to fit the data, except as a very small fraction ($\sim$ 2%), in combination with other sites. Fits to the experimental data for the IIb post-anneal sample using only a bond-centred (plus random) fraction can be seen in Figure 8.13. A likely configuration, which satisfies both the theoretical and experimental results, is the In in a divacancy (as in the calculated system), with a vacancy or interstitial at next-nearest neighbour position or the like, which breaks the symmetry, allowing the In to relax along the $\langle 111 \rangle$ direction. More than two vacancies being present in the system was not considered in the theoretical calculations and is a possibility, due to the large amount of vacancies introduced in implantation. An important point to note about the calculations is the calculated quadrupole coupling frequency of approximately 100 MHz with a <111> high-symmetry direction. A number of authors have reported an In fraction occupying a site with <111> symmetry and a corresponding coupling frequency of 117 MHz (see Table 2.1). It does thus seem likely that the calculated V_C-In-V_C complex is that which has been observed in previous studies (the calculated coupling frequency does suffer from errors due to the exclusion of the effects of core polarisation and the use of the pseudopotential approximation). The observed defect was only found after annealing of the diamond samples in the previous studies. Similarly in our calculations the total energy of the V_C-In-V_C complex was found to be significantly lower after the removal of the self-interstitials (6.59 eV and the configuration changed from metastable to stable). This is the expected effect of annealing, the high mobility of interstitials under annealing being well known (see Chapter 2). Further support for the existence of the V_C-In-V_C complex was the discovery of an identical structure (probe atom bond-centred in a divacancy), for nickel in HPHT di-

amond (Nadolinny *et al*, 1997). Nickel is a common catalyst in the HPHT growth of diamond.

The effect of annealing the sample can clearly be seen in the IIb pre- and post-anneal fractions. After annealing the fraction of emitters on substitutional sites increased as expected, at the expense of the emitters at both the S-BC(0.6) and the random sites. This is in agreement with the previous work done on this system (Burchard *et al*, 1993, Quintel *et al*, 1996, and Hofsäss *et al*, 1993). Since annealing at the temperatures we used (1473 K, normal pressure), is known to heal the lattice through the recombination of vacancies and self-interstitials, this suggests that In at the S-BC(0.6) site involves these defects, and that In at the substitutional site does not. After annealing recombination of vacancies and self-interstitials decreased this fraction.

As mentioned earlier previous measurements have yielded a random or irregular fraction, the origin of which is unknown. The random fraction could (partially) contain In bonded in various different multi-vacancy complexes, which yield a variety of different low fraction In lattice positions. The random sites are those of low enough concentration (less than a few percent of probe atoms occupy them), so that they cannot be individually distinguished. If complexation with boron, hydrogen or nitrogen or any other defect such as oxygen occurs at a very low level (less than a few percent), then this would also form part of the random fraction.

The existence of a substantial substitutional fraction, in both these and previous measurements, is perhaps harder to explain. In Chapter 5 - see Table 5.1, substitutional In was found to be at best a metastable state. Ballistic considerations just slightly above thermal equilibrium near the end of the implantation cascade may lead to this configuration. Annealing may restore damage in such a way as to increase the substitutional fraction.

In silicon a particular relationship was found to exist between group-III and group-V dopants (Mayer *et al*, 1970). If a group-III dopant was implanted into a crystal that already had a group-V dopant then the group-III atoms occupied a much greater fraction of substitutional sites than if they were implanted alone into the pure crystal, and in addition no interstitial sites were discernible. This has been explained in terms of the formation of local chemical bonds between the acceptor and the donor atoms (Antoncik, 1986). The charge states of the Frenkel defects resulting from the implantation are of importance in determining the Fermi level and the resultant defect reaction kinetics. Perturbed angular correlation measurements on silicon doped with In and As showed the formation of In-As pairs (Wichert *et al*, 1986). It was hypothesised that the formation of these pairs "pulled" the In atoms onto substitutional sites. We implanted In atoms into diamond containing another group-V element, namely nitrogen. In this case the nitrogen was naturally occurring in the form of A and B centres. A centres have been speculated to be deep-lying donors in diamond (Davies, 1977). We also implanted In into type IIb diamond which naturally has a group-III dopant already in place, namely boron (type IIb diamond has typically of the order of 0.25 ppm uncompensated boron (Field, 1979)), to see if any competition for substitutional sites or any other defect-defect interaction occurred. This also served to investigate whether the p-type semiconducting nature of this sample, and thus the resultant differing Fermi level, influenced the In lattice site. None of the above effects were observed, lending weight to the argument that complexation with only one defect, common to all the samples, occurred.

Previously in this section we stated that the probability of In-vacancy complexes was greater than that of In-self-interstitial complexes, in the absence of any Coulombic interaction. It is not however always possible to rule out the occurrence of a charged In ion encountering a self-interstitial of opposite charge. In germanium, as mentioned, the formation of In-self-interstitial complexes has been reported and thus in their study the authors postulate a Coulombic interaction (Haesslein *et al*, 1998). In our DFT calcula-

tions the V_C-In-V_C complex did involve self-interstitials (with a higher total energy of the complex), until these were removed, as they would be in annealing (see Figure 5.3). We expect In-self-interstitial complexes to form in diamond after implantation but, due to the high mobility of the self-interstitials and the calculated metastable nature of the V_C-In-V_C complex while the self-interstitials are present, for such complexes not to be stable under annealing.

A number of authors have observed the formation of In-H pairs in silicon (Wichert *et al*, 1987, Deicher *et al*, 1989, and Skudlik *et al*, 1992a), and germanium (Deicher *et al*, 1989). In silicon, two In-H complexes are known to form, with <111> axial orientation (Wichert *et al*, 1987), thought to be In bonded to a single hydrogen in either a neutral or a negative charge state (Skudlik *et al*, 1992a). Only one stoichiometry of this In-H complex was shown to be formed (Skudlik *et al*, 1992a). Assuming In on a substitutional site the hydrogen has been hypothesised to lie on either the bond-centred (BC), anti-bonding (AB) or tetrahedral (T) sites, in order to give the observed <111> symmetry. These pairs were found to dissociate at approximately 420 K with an energy of 1.3 eV. The population of these complexes was found to depend on the Fermi level and the concentration of free holes (Skudlik *et al*, 1992a). In germanium only one In-H complex was found to form, also with <111> symmetry (Deicher *et al*, 1989). An upper limit for the dissociation of this complex was set at 1.1 eV. In order to discover whether similar interactions occur in diamond we pre-implanted hydrogen into two of the diamond samples under study. As reported no differences in the site fractions were obtained (within the given errors), between the samples implanted with hydrogen and those without, which suggests that the complexes do not involve hydrogen.

The lack of any apparent effect due to the formation of In-H pairs can be correlated to similar work in silicon (Skudlik *et al*, 1992b). In this study the number of such pairs formed was found to have a strong dependence on implantation energy. The number of In-H pairs for a 200 eV H^+ implant was found to be approximately ten times greater

than if the implant was done at 1 keV. This was postulated to be because of vacancies caused during implantation (at 200 eV less than 0.5 vacancies are created per ion, whereas approximately 1.15 are created per hydrogen ion at 1 keV). The vacancies were thought to provide strongly competitive traps for the hydrogen. It should be noted that the detection of In-H pairs in silicon was via PAC, not CEEC. PAC measurements on In in diamond found no complexation with hydrogen (Deicher, 1998). Our studies on hydrogen implantation into diamond at similar energies and doses to that used in the CEEC work have shown it to strongly trap in its own range distribution (see previous section). We expect this to have been the case for the hydrogen implantations in the indium work.

We have postulated in this discussion that a vacancy or self-interstitial, located at next-nearest neighbour or the like, is the defect responsible for pulling the In in the V_C-In-V_C complex off centre into the S-BC(0.6) site. As mentioned in the discussion on hydrogen distributions in diamond all diamonds have been found to have an intrinsic hydrogen concentration. The In implantation cascade is likely to liberate such hydrogen to allow it to interact with the In. A distinct possibility is then for the hydrogen to bond to the V_C-In-V_C complex. This could then pull the In away from its bond-centred position. Since the hydrogen is in all the samples we studied this would result in the identical site fractions obtained[11]

In summary, the experimental results together with the theoretical calculations, indicate that the In finds itself either at a defect-free substitutional position, at a position between substitutional and bond-centred (60% towards BC), or at various other low fraction, irregular sites which may involve vacancies. The S-BC(0.6) site is thought to be a divacancy plus another, more distant defect. The previously determined substitutional or near-substitutional fraction has thus been differentiated into an exactly

[11]The quadrupole frequency of 117 MHz measured in previous PAC studies (see Table 2.1), could thus also involve hydrogen. This could be an explanation of why the work of Deicher saw no evidence of hydrogen complexation.

substitutional site plus one (S-BC(0.6)) approximately 0.45 Å away. Another possibility for a symmetry breaking defect is hydrogen, liberated during implantation and bonded to the calculated V_C-In-V_C complex. The possibility of the formation of In-self-interstitial complexes before annealing has not been excluded by this work.

Chapter 9

Conclusions

The technique of 2-dimensional Conversion Electron Emission Channeling (CEEC) has been applied to the study of ^{111}In in diamond. The aim of this research was to investigate the formation of indium-defect complexes in the diamond bulk. The experiments were performed on a carefully chosen suite of diamonds containing various defect systems including nitrogen in various configurations, boron, hydrogen and vacancies. We have made the first such investigations of ^{111}In implanted into defect-rich diamonds and obtained fractions for the sites occupied. This comprehensive 2-dimensional work is a significant improvement over earlier measurements. The experimental studies have been directly compared to density functional theory calculations of the ^{111}In in pure diamond system. These calculations were made in collaboration with the Physics department at the University of the Witwatersrand.

One of the defects studied as a possible partner for indium in defect complexes was hydrogen. In silicon (a structural (crystal) analogue of diamond), the passivation of indium and other dopants by hydrogen is well documented. It was necessary to acquire knowledge on the mobility of hydrogen and its distributions to fully interpret any indium-hydrogen complexation which might be observed. Thus Elastic Recoil Detection Analysis (ERDA) measurements were performed on a number of diamond

samples under differing conditions. These included diffusion studies on hydrogen introduced into diamond through implantation and plasma loading. The bulk hydrogen distributions of both natural and CVD diamonds were also measured.

Previous experimental results on indium implanted into type IIa diamond indicated a large (between 35 and 60%), substitutional or very near-substitutional (less than 0.2 Å away), fraction. Our results indicate that the In finds itself either at a defect-free substitutional position, at a position between substitutional and bond-centred (60% towards BC), or at various other low fraction, irregular sites which may involve vacancies. The S-BC(0.6) site is thought to be a divacancy plus another, more distant defect. The previously determined substitutional or near-substitutional fraction has thus been differentiated into an exactly substitutional site plus one (S-BC(0.6)) approximately 0.45 Å away. Complexation with any of the defects, including boron (p-type), hydrogen and nitrogen, although not excluded, is not detected. The possibility of hydrogen being the defect that breaks the symmetry of the calculated complex to form the S-BC(0.6) site is suggested. Indium-self-interstitial complexes may also form prior to annealing.

The importance of vacancies, single and multiple, produced during implantation, on the final In-host configuration in diamond has been suggested in this study. Future work should concentrate on this defect which in many cases is thought to dominate over other impurities, whether intrinsic to or introduced into the sample during implantation. It is thought to play a major role in the random fraction detected in these and earlier measurements. Theoretical modelling of impurities such as In in diamond should be extended to include single- and multi-vacancy configurations, as well as hydrogen together with the already calculated V_C-In-V_C configuration. Further experimental work is needed to confirm the nature of the sites in question. PAC studies would be helpful as any differences in bonding partners of the In probe can be identified with this technique.

The stability of implanted hydrogen under annealing has been confirmed in this the-

sis. Possible plasma loading of pre-damaged diamond has been indicated (however not of the order expected considering the amounts of traps and hydrogen present). Measurements on a number of diamonds have shown that all natural diamonds have an intrinsic hydrogen concentration. This result is of importance when considering the In complexes that are formed in the diamond bulk. Many different trapping sites for the hydrogen were discussed in the previous chapter. These include vacancies, paired hydrogen complexes, amorphised diamond, nitrogen centres and dislocations. Similarly a number of diffusion pathways were suggested, the importance of a surface barrier to diffusion being postulated. It is important to note that further work is needed to test these hypotheses. This includes ERDA measurements of low dose, low energy (below the vacancy creation threshold), hydrogen implanted diamond. Improvement of the detection limit of our system is presently underway, which will aid such investigations. The utilisation of other techniques, such as Raman spectroscopy of the implanted hydrogen would further illuminate the situation.

The study of the doping of diamond is presently of great interest as a candidate for a new generation of electronic devices. It is hoped that this thesis has led to a greater understanding of the behaviour of heavy dopants in diamond. In particular we have concentrated on the formation of complexes in the diamond bulk. The mobility and intrinsic content of hydrogen in diamond has also been investigated to complement this work.

References

Andersen, J.U., Andersen, S.K. and Augustyniak, W.M., (1977) *K. Dan. Vidensk. Selsk. Mat.-Fys. Medd.*, **39**, No. 10

Andersen, J.U., Eriksen, K.R. and Lægsgaard, E., (1981) *Phys. Scri.*, **24**, 588-600

Andersen, J.U., Bonderup, E., Lægsgaard, E., Marsh, B.B. and Sørensen, A.H., (1982a) *Nucl. Instr. and Meth.*, **194**, 209-224

Andersen, J.U., Datz, S., Lægsgaard, E., Sellschop, J.P.F. and Sørensen, A.H., (1982b) *Phys. Rev. Lett.*, **49**, 215-218

Andersen, J.U., Bonderup, E. and Lægsgaard, E., (1985) in *Coherent Radiation Sources*, eds. Sáenz, A.W. and Überall, H., Springer, Berlin, p127

Andeweg, A.H., Ballestrero, S., Beer, J.U.M., Butler, J.E., Breese, M.B.H., Connell, S.H., Dini, L., Doyle, B.P., Drummond, M.L., Formenti, P., Hart, R.J., Machi, I.Z., Maclear, R.D., McQueen, I.D., Schaaff, P., Sideras-Haddad, E., Sellschop, J.P.F. and Wernick, G., (1997) *Nucl. Instr. and Meth. B*, **130**, 37-44

Antoncik, E., (1986) *Nucl. Instr. and Meth. B*, **17**, 325-330

Appel, H., Raudies, J., Thies, W.-G., Hanser, A. and Sellschop, J.P.F., (1981) *Hyperfine Interact.*, **10**, 735-740

Arkiphov, I.I., Spitsyn, B.V., Gorodetsky, A.E., Zakharov, A.P., Popovici, G., Sung, T., Prelas, M.A. and Khasawinah, S. ,(1996) *Diamond and Relat. Mater.*, **5**, 121-123

Arnold Bik, W.M. and Habraken, F.H.P.M., (1993) *Rep. Prog. Phys.*, **56**, 859-902

Assmann, W., Hartung, P., Huber, H., Staat, P., Steefens, H. and Steinhausen, Ch., (1994) *Nucl. Instr. and Meth. B*, **85**, 726-731

Assmann, W., Davies, J.A., Dollinger, G., Forster, J.S., Huber, H., Reichelt, Th. and Siegele R., (1996) *Nucl. Instr. and Meth. B*, **118**, 242-250

Avasthi, D.K., Kabiraj, D., Jaipal, Mehta, G.K., Barshilia, H.C., Somna Sah, Mehta, B.R. and Vankar, V.D., (1995) *Vacuum*, **46**, 633-636

Bair, A.E., Atzmon, Z., Russell, S.W., Barbour, J.C., Alford, T.L. and Mayer, J.W., (1996) *Nucl. Instr. and Meth. B*, **118**, 274-277

Ballestrero, S., Connell, S.H., Doyle, B.P. and Maclear, R.D., (1999) *Nucl. Instr. and Meth. A*, to be submitted

Behrisch, R., Prozesky, V.M., Huber H. and Assmann, W., (1996) *Nucl. Instr. and Meth. B*, **118**, 262-267

Bernholc, J., Kajihara, S.A., Wang, C., Antonelli, A. and Davis, R.F., (1992) *Mater. Sci. Eng.*, **B11**, 265-272

Bharuth-Ram, K., Burchard, A., Deicher, M., Freitag, K., Hofsäss, H., Jahn, S.G., Magerle, R., Quintel, H., Restle, M., Ronning, C. and the ISOLDE Collaboration, (1996) *Proc. 10th Int. Conf. on Hyperfine Interactions*, ed. Rots, M., Vantomme, A., Dekoster, J., Coussement, R. and Langouche, G., Baltzer, Basel, 211-214

Born, M. and Oppenheimer, R., (1927) *Ann. d. Phys.*, **84**, 457-484

Bourgoin, J.C. and Massarini, B., (1976) *Phys. Rev. B*, **14**, 3690-3694

Briddon, P., Jones, R. and Lister, G.M.S., (1988) *J. Phys. C.*, **21**, L1027-1031

Burchard, A., Restle, M., Deicher, M., Hofsäss,H., Jahn, S.G., König, Th., Magerle, R., Pfeiffer, W. and Wahl, U., (1993) *Physica B*, **185**, 150-153

Butler, J.E. and Woodin, R.L., (1993) *Phil. Trans. R. Soc. Lond. A*, **342**, 209-224

Butler, J.E., (1996), private communication

Butler, J.E., (1998), private communication

Ceperley, D.M. and Alder, B.J., (1980) *Phys. Rev. Lett.*, **45**, 566-569

Chang, K.J. and Chadi, D.J., (1989) *Phys. Rev. Lett.*, **62**, 937-940

Chevallier, J., Theys, B., Lusson, A., Grattepain, C., Deneuville, A. and Gheeraert, E., (1998) *Phys. Rev. B*, **58**, 7966-7969

Chrenko, R.M., McDonald, R.S. and Darrow, K.A., (1967) *Nature*, **213**, 474-476

Chrenko, R.M., Strong, H.M. and Tuft, R.E., (1971) *Philos. Mag.*, **23**, 313-318

Chrenko, R.M., (1973) *Phys. Rev. B*, **7**, 4560-4567

Chu, W.-K., Mayer, J.W. and Nicolet, M.-A., (1978) *Backscattering Spectrometry*, Academic Press, New York

Clark, C.D. and Palmer, D.W., (1960) *Proceedings of the 4th Symposium on Reactivity of Solids*, Elsevier, Amsterdam, 436

Clark, C.D., Dean, P.J. and Harris, P.V., (1964) *Proc. R. Soc. London*, Ser. A **277**, 312-329

Claxton, T.A., Evans, A. and Symonds, M.C.R., (1986) *J. Chem. Soc. Faraday. Trans. II*, **82**, 2031-2037

Cohen, M.L. and Heine, V., (1970) Solid State Physics, **24**, 37-248

Collins, A.T., Lightowlers, E.C. and Dean, P.J., (1969) *Phys. Rev.*, **183**, 725-730

Connell, S.H., Sideras-Haddad, E., Smallman, C.G., Sellschop, J.P.F., Machi, I.Z. and Bharuth-Ram, K., (1996) *Nucl. Instr. and Meth. B*, **118**, 332-337

Connell, S.H., Sellschop, J.P.F., Maclear, R.D., Doyle, B.P., Machi, I.Z., Nilen, R.W.N., Butler, J.E. and Bharuth-Ram, K., (1997) *Mat. Sci. For.*, **258-263**, 751-756

Connell, S.H., Sellschop, J.P.F., Butler, J.E., Maclear, R.D., Doyle, B.P. and Machi, I.Z., (1998) *Diamond and Relat. Mater.*, **7**, 1714-1718

Davies, G., (1976) *J. Phys. C*, **9**, L537-542

Davies, G., (1977) in *Chem. Phys. Carbon*, eds. Walker, P.J. and Thrower, P.A., **13**, p1-143

Davies, G., Lawson, S.C., Collins, A.T., Mainwood, A. and Sharp, S.J., (1992) *Phys. Rev. B*, **46**, 13157-13170

Davies, G., (ed.) (1994a) *Properties and Growth of Diamond*, INSPEC, the Institution of Electrical Engineers, London

Davies, G., (1994b) in *Properties and Growth of Diamond*, ed. G. Davies, INSPEC, the Institution of Electrical Engineers, London, p135-138

Davies, G. and Manson, N.B., (1994) in *Properties and Growth of Diamond*, ed. G. Davies, INSPEC, the Institution of Electrical Engineers, London, p159-165

Deicher, M., Keller, R., Pfeiffer, W., Skudlik, H., Steiner, D., Recknagel, E. and Wichert, Th., (1989) *Mater. Sci. & Eng.*, **B4** 25-29

Deicher, M., (1998), private communication

DeWames, R.E. and Hall, W.F., (1968) *Acta Cryst.*, **A24**, 206-212

Dollinger, G., Faestermann, T. and Maier-Komor, P., (1992) *Nucl. Instr. and Meth. B*, **64**, 422-427

Dollinger, G., (1993) *Nucl. Instr. and Meth. B*, **79**, 513-517

Dollinger, G., Boulouednine, M., Bergmaier, A., Faestermann, T. and Frey, C.M., (1996) *Nucl. Instr. and Meth. B*, **118**, 291-300

Domeij, B. and Björkvist, K., (1965) *Phys. Lett.*, **14**, 127-128

Doyle, B.L. and Brice D.K., (1988) *Nucl. Instr. and Meth. B*, **35**, 301-308

Doyle, B.P., Maclear, R.D., Connell, S.H., Formenti, P., Machi, I.Z., Butler, J.E., Schaaff, P., Sellschop, J.P.F., Sideras-Haddad, E. and Bharuth-Ram,K., (1997) *Nucl. Instr. and Meth. B*, **130**, 204-210

Doyle, B.P., Dewhurst, J.K., Lowther, J.E. and Bharuth-Ram, K., (1998) *Phys. Rev. B*, **57**, 4965-4967

Doyle, B.P., Storbeck, E.J., Wahl, U., Connell, S.H. and Sellschop, J.P.F., (1999) *J. Phys.: Condens. Matter*, submitted

Doyle, P.A. and Turner, P.S., (1968) *Acta Cryst.*, A24, 390-397

Dyer, H.B. and Ferdinando, P., (1966) *Br. J. Appl. Phys.*, **17**, 419-420

Edge, K.D. and Bill, U., (1980) *Nucl. Instr. and Meth.*, **168**, 157-162

Estle , T.L., Estreicher, S. and Marynick, D.S., (1987) *Phys. Rev. Lett.*, **58**, 1547-1550

Estreicher, S., Ray, A.K., Fry, J.L. and Marynick, D.S., (1986) *Phys. Rev. B*, **34**, 6071-6079

Estreicher, S.K., (1995) *Mater. Sci. Eng.*, **R14**, 319-412

Estreicher, S.K., Hastings, J.L. and Fedders, P.A., (1998) *Phys. Rev. B*, **57**, R12663-R12665

Evans, T., (1979) in *The Properties of Natural and Synthetic Diamond*, ed. J.E. Field, Academic Press, London, p408-418

Evans, T., Qi, Z. and Maquire, J., (1981) *J. Phys. C*, **14**, L379-384

Evarestov, R.A. and Smirnov, V.P., (1983) *Phys. Status Solidi B*, **119**, 9-40

Farrer, R.J., (1969) *Solid State Commun.*, **7**, 685-688

Feuser, U., Vianden, R. and Pasquevich, A.F., (1990) *Hyperfine Interact.*, **60**, 829-832

Field, J.E., (ed.) (1979) *The Properties of Diamond*, Academic Press, London

Field, J.E., (ed.) (1992) *The Properties of Natural and Synthetic Diamond*, Academic Press, London

Frank, W., (1991) *Defect Diffus. Forum*, **75**, 121-148

Fu, H. and Zunger, A., (1997) *Phys. Rev. B*, **56**, 1496-1508

Gavrilenko, V.I., (1993) *Phys. Rev. B*, **47**, 9556-9560

Gemmell, D.S., (1974) *Rev. Mod. Phys.*, **46**, 129-227

Gippius, A.A., (1995) *Mat. Sci. For.*, **196-201**, 85-90

Goodwin, D.G. and Butler, J.E., (1997) in Prelas, M.A., Popovici, G. and Bigelow, L.K. (ed.), *Handbook of Industrial Diamonds and Diamond Films*, 1st edition, Marcel Dekker Inc.

Goppelt-Langer, P, Yamamoto, S., Aoki, Y., Takeshita, H. and Naramoto, H., (1996) *Nucl. Instr. and Meth. B*, **118**, 251-255

Goss, J., Jones, R., Briddon, P.R. and Öberg, S., (1997) *Proceedings of the Diamond Conference*, unpublished

Gossett, C.R., (1986) *Nucl. Instr. and Meth. B*, **15**, 481-485

Grime, G.W., Dawson, M., Marsh, M., McArthur, I.C. and Watt, F., (1991) *Nucl. Instr. and Meth. B*, **54**, 52-63

Groleau, R., Gujrathi, S.C. and Martin, J.P., (1983) *Nucl. Instr. and Meth.*, **218**, 11-15

Haesslein, H., Sielemann, R., Brüßler, M. and Metzner, H., (1994) *Hyperfine Interact.*, **84**, 65-68

Haesslein, H., Sielemann, R. and Zistl, C., (1998) *Phys. Rev. Lett.*, **80**, 2626-2629

Hayashi, K., Yamanaka, S., Watanabe, H., Sekiguchi, T., Okushi, H. and Kajimura, K., (1997) *J. Appl. Phys.*, **81**, 744-753

Hofsäss, H., Lindner, G., Recknagel, E. and Wichert, Th., (1984) *Nucl. Instr. and Meth. B*, **2**, 13-18

Hofsäss, H., Lindner, H., Winter, S., Besold, B., Recknagel, E., Weyer, G. and Petersen, J.W., (1986) *mater. Sci. Forum*, **10-12**, 1183

Hofsäss, H., Besold, B., Lindner, G., Winter, S., Recknagel, E. and Weyer, G., (1987) in *Relativistic Channeling*, eds. Carrigan Jr., R.A. and Ellison, J.A., Plenum, New York, p483-491

Hofsäss, H. and Lindner, G., (1991) *Phys. Rep.*, **210**, 121-183

Hofsäss, H., Winter, S., Jahn, S.G., Wahl, U., Recknagel, E. and the ISOLDE Collaboration, (1992) *Nucl. Instr. and Meth. B*, **63**, 83-90

Hofsäss, H., Restle, M., Wahl, U. and Recknagel, E., (1993) *Nucl. Instr. and Meth. B*, **80/81**, 176-179

Hofsäss, H., Wahl, U. and Jahn, S.G., (1994) *Hyperfine Interact.*, **84**, 27-41

Hofsäss, H., (1996) *Hyperfine Interact.*, **97/98**, 247-283

Hohenberg, P. and Kohn, W., (1964) *Phys. Rev.*, **136**, B864-B871

Holbech, J.D., Bech Nielsen, B., Jones, R., Sitch, P. and Öberg, S., (1993) *Phys. Rev. Lett.*, **71**, 875-878

Howie, A., (1978) in *Diffraction and Imaging Techniques in Materials Science*, 2nd edition, eds. Amelinckx, S. and Gevers, R., North-Holland, Amsterdam, p457-509

Isoya, J., Wakoh, S., Matsumoto, M. and Morita, Y., (1993) *JAERI TIARA Annual Report*, **3**, 21-23

Jia, H., Shinar, J., Lang, D.P. and Pruski, M., (1993) *Phys. Rev. B*, **48**, 17595-17598

Jones, R.O. and Gunnarsson, O., (1989) *Rev. Mod. Phys.*, **61**, 689-746

Jones, R., Lowther, J.E. and Goss, J., (1996) *Appl. Phys. Lett.*, **69**, 2489-2491

Kalish, R., Deicher, M., Recknagel, E. and Wichert, Th., (1979) *J. Appl. Phys.*, **50**, 6870-6872

Kanda, H., Ohsawa, T. and Yamaoka, S., (1990) in *Science and Technology of New Diamond*, eds. Saito, S., Fukunaga, O. and Yoshikawa, M., KTK, Tokyo, p339-344

Kiflawi, I., Fisher, D., Kanda, H. and Sittas, G., (1996) *Diamond and Relat. Mater.*, **5**, 1516-1518

Kittel, C., (1986) *Introduction to Solid State Physics*, 6th edition, John Wiley & Sons, New York

Klein, S.S. and Rijken, H.A., (1992) *Nucl. Instr. and Meth. B*, **66**, 393-396

Kluev, Yu.A., Dudenkov, Yu.A. and Nepsha, B.I., (1973) *Geokhimiya*, 1029-1035

Knudson, A.R., (1980) *Nucl. Instr. and Meth.*, **168**, 163-167

Kohn, W. and Sham, L.J., (1965) *Phys. Rev.*, **140**, A1133-A1138

Landstrass, M.I. and Ravi, K.V., (1989a) *Appl. Phys. Lett.*, **55**, 975-977

Landstrass, M.I. and Ravi, K.V., (1989b) *Appl. Phys. Lett.*, **55**, 1391-1393

L'Ecuyer, J., Brassard, C., Cardinal, C., Chabbal, J., Deschênes, L., Labrie, J.P., Terrault, B., Martel, J.G. and St.-Jacques, R., (1976) *J. Appl. Phys.*, **47**, 381-382

L'Ecuyer, J., Davies, J.A. and Matsunami, N., (1980) *Radiat. Effects*, **47**, 229-232

Leitch, A.W.R., Alex, V. and Weber, J., (1998) *Phys. Rev. Lett.*, **81**, 421-424

Leo, W.R., (1994) *Techniques for Nuclear and Particle Physics Experiments*, 2nd edition, Springer-Verlag, Berlin

Lervig, P., Lindhard, J. and Nielsen, V., (1967) *Nucl. Phys. A*, **96**, 481-504

Levy, D.H. and Gleason, K.K., (1992) *J. Phys. Chem.*, **96**, 8125-8131

Levy, M., (1979) *Proc. Natl. Acad. Sci. (USA)*, **76**, 6062-6065

Li, L.H. and Lowther, J.E., (1997) *J. Phys. Chem. Solids*, **58**, 1607-1610

Lightowlers, E.C. and Collins, A.T., (1976) *Diamond Research 1976*, Industrial Diamond Information Bureau, London, 14-21

Lindhard, J., (1965) *Mat. Fis. Medd. Dan. Vid. Selsk.*, **34**, No.14

Lindner, G., Hofsäss, H., Winter, S., Besold, B., Recknagel, E., Weyer, G. and Petersen, J.W., (1986) *Phys. Rev. Lett.*, **57**, 2283-2286

Looi. H.J., Pang, L.Y.S., Molloy, A.B., Jones, F., Foord, J.S. and Jackman, R.B., (1998) *Diamond and Relat. Mater.*, **7**, 550-555

Maas, A.J.H., Kelin, S.S., Simons, D.P.L. and de Voigt, M.J.A., (1996) *Nucl. Instr. and Meth. B*, **118**, 268-273

Machi, I.Z, Connell, S.H., Schaaff, P., Doyle, B.P., Maclear, R.D., Bharuth-Ram, K, Formenti, P. and Sellschop, J.P.F., (1997) *Nucl. Instr. and Meth. B*, **127/128**, 212-216

Machi, I.Z., Butler, J.E., Connell, S.H., Doyle, B.P., Maclear, R.D., Sellschop, J.P.F., Sideras-Haddad, E. and Rebuli, D.B., (1999) *Diamond and Relat. Mater.*, in press

Machi, I.Z., Connell, S.H., Baker, M., Sellschop, J.P.F., Bharuth-Ram, K., Cox, S.F.J. and Butler J.E., (1999) *Hyperfine Interact.*, submitted

Maclear, R.D., Connell, S.H., Doyle, B.P., Machi, I.Z., Butler, J.E., Sellschop, J.P.F., Naidoo, S.R. and Fritsch, E., (1998) *Nucl. Instr. and Meth. B*, **136-8**, 579-582

Maclear, R.D., Butler, J.E., Connell, S.H., Doyle, B.P., Machi, I.Z., Rebuli, D.B., Sellschop, J.P.F. and Sideras-Haddad, E., (1999) *Diamond and Relat. Mater.*, in press

Madiba, C.C.P., Sellschop, J.P.F, Annegarn, H.J. and Appleton, B.R., (1983) *Nucl. Instr. and Meth.*, **218**, 409-414

Madiba, C.C.P., Sellschop, J.P.F. van Wyk, J.A. and Annegarn, H.J., (1988) *Nucl. Instr. and Meth. B*, **35**, 442-445

Mainwood, A and Stoneham, A.M., (1984) *J. Phys. C.*, **17**, 2513-2524

Marion, J.B. and Young, F.C., (1968) *Nuclear Reaction Analysis*, North-Holland, Amsterdam, p142

Mayer, J.W., Ericksson, L. and Davies, J.A., (1970) *Ion Implantation in Semiconductors: Silicon and Germanium*, Academic Press, New York, p169 and refs. therein

Mayer, J.W. and Rimini, E., (1977) *Ion Beam Handbook for Materials Analysis*, Academic Press, New York

McNamara, K.M., Levy, D.H., Gleason, K.K. and Robinson, C.J., (1992) *Appl. Phys. Lett.*, **60**, 580-582

McNamara, K.M., Williams, B.E., Gleason, K.K. and Scruggs, B.E., (1994) *J. Appl. Phys.*, **76**, 2466-2472

McNamara Rutledge, K.M., Scruggs, B.E. and Gleason, K.K., (1995) *J. Appl. Phys.*, **77**, 1459-1462

McNamara Rutledge, K.M. and Gleason, K.G., (1996) *Chem. Vap. Deposition*, **2**, 37-43

Mehandru, S.P., Anderson, A.B. and Angus, J.C., (1992) *J. Mater. Res.*, **7**, 689-695

Mehandru, S.P. and Anderson, A.B., (1994) *J. Mater. Res.*, **9**, 383-395

Mitra, S. and Gleason, K.K., (1993) *Diamond and Relat. Mater.*, **2**, 126-129

Murakami, K., Fukata, N., Sasaki, S., Ishioka, K., Kitajima, M., Fujimura, S., Kikuchi, J. and Haneda, H., (1996) *Phys. Rev. Lett.*, **77**, 3161-3164

Nadolinny, V.A., Yelisseyev, A.P., Yuryeva, O.P. and Feygelson, B.N., (1997) *Appl. Magn. Reson.*, **12**, 543-554

Nielsen, O.H., Larsen, F.K, Damgaard, S., Petersen, J.W. and Weyer, G., (1983) *Z. Phys. B*, **52**, 99-109

Nilen, R.W.N., (1998) Ph.D. Thesis, University of the Witwatersrand

Patterson, B.D., (1988) *Rev. Mod. Phys.*, **60**, 69-159

Payne, M.C., Teter, M.P., Allan, D.C., Arias, T.A. and Joannopoulos, J.D., (1992) *Rev. Mod. Phys.*, **64**, 1045-1097

Percus, J.K., (1978) *Int. J. Quantum Chem.*, **13**, 89

Perdew, J.P. and Zunger, A., (1981) *Phys. Rev. B*, **23**, 5048-5079

Perdew, J.P. and Wang, Y., (1992) *Phys. Rev. B*, **45**, 13244-13249

Perdew, J.P., Burke, K. and Ernzerhof, M., (1996) *Phys. Rev. Lett.*, **77**, 3865-3868

Phillips, J.C., (1958), *Phys. Rev.*, **112**, 685-695

Piercy, G.R., Brown, F., Davies, J.A. and McCargo, M., (1963) *Phys. Rev. Lett.*, **10**, 399-400

Pogany, A.P. and Turner, P.S., (1968) *Acta Cryst.*, A**24**, 103-109

Popovici, G., Wilson, R.G., Sung, T., Prelas, M.A. and Khasawinah, S., (1995) *J. Appl. Phys.*, **77**, 5103-5106

Prins, J.F., (1988) *Phys. Rev. B*, **38**, 5576-5584

Prins, J.F., (1989) *Phys. Rev. B*, **39**, 3764-3770

Prins, J.F., (1992) *Mater. Sci. Rep.*, **7**, 271-364

Prins, J.F., (1993a) *Nucl. Instr. and Meth. B*, **80/81**, 1433-1440

Prins, J.F., (1993b) *Physica B*, **185**, 132-143

Prins, J.F., (1998a) *Mat. Res. Innovat.*, **1**, 243-253

Prins, J.F., (1998b) *Diamond and Relat. Mater.*, in press

Prins, J.F., (1998c), private communication

Prins, J.F., (1998d) *Diamond Films and Techn.*, in press

Prins, J.F., (1998e) *Diamond and Relat. Mater.*, **7**, 545-549

Quintel, H., Bharuth-Ram, K., Hofsäss, H., Restle, M. and Ronning, C., (1996) *Nucl. Instr. and Meth. B*, **118**, 72-75

Raudies, J.H., Appel, H., Then, G.M., Thies, W.-G., Freitag, K., Sellschop, J.P.F. and Stemmet, M.C., (1983) *Hyperfine Interact.*, **15/16**, 487-490

Rauhala, E., (1995) in *Handbook of Modern Ion Beam Materials Analysis*, eds. Tesmer, J.R., Nastasi, M., Charles Barbour, J., Maggiore, C.J. and Mayer, J.W., MRS, Pittsburgh, p3-20

Ross, G. and Terreault, B., (1980) *J. Appl. Phys.*, **51**, 1259-1261

Ross, G.G., Terreault, B., Gobeil, G., Abel, G., Boucher, C. and Veilleux, G., (1984) *J. Nucl. Mater.*, **128/129**, 730-733

Runciman, W.A. and Carter, T., (1971) *Solid State Commun.*, **9**, 315-317

Salomon, M., (1964) *Nuclear Physics*, **54**, 171-176

Schatz, G. and Weidinger, A., (1992) *Nuclear Condensed Matter Physics*, John Wiley & Sons, Chichester

Schiettekatte, F., Chevarier, A., Chevarier, N., Plantier, A. and Ross G.G., (1996) *Nucl. Instr. and Meth. B*, **118**, 307-311

Schmid, K. and Ryssel, H., (1974) *Nucl. Instr. and Meth.*, **119**, 287-289

Sellschop, J.P.F., Keddy, R.J., Mingay, D.W., Renan, M.J. and Schuster, D.G., (1975) *Int. J. App. Rad. Isotopes*, **26**, 640-647

Sellschop, J.P.F., Madiba, C.C.P. and Annegarn, H.J., (1979) *Diamond Conf. (Cambridge)*, abstracts p43-44

Sellschop, J.P.F., Madiba, C.C.P. and Annegarn, H.J., (1980) *Nucl. Instr. and Meth.*, **168**, 529-534

Sellschop, J.P.F., (1987) *Diamond Conf. (Bristol)*, abstracts p45-52

Sellschop, J.P.F., (1992) in *The Properties of Natural and Synthetic Diamond*, ed. J.E. Field, Academic Press, London, p89-91

Sellschop, J.P.F., (1998), private communication

Siegele, R., Assmann, W., Davies, J.A. and Forster, J.S., (1996) *Nucl. Instr. and Meth. B*, **118**, 283-290

Sigmund, P., (1997) *Phys. Rev. A*, **56**, 3781-3793

Sigmund, P. and Glazov, L., (1998) *Nucl. Instr. and Meth. B*, **136-138**, 47-54

Skudlik, H., Deicher, M., Keller, R., Magerle, R., Pfeiffer, W., Steiner, D., Recknagel, E. and Wichert, Th., (1992a) *Phys. Rev. B*, **46**, 2159-2171

Skudlik, H., Deicher, M., Keller, R., Magerle, R., Pfeiffer, W., Pross, P., Recknagel, E. and Wichert, Th., (1992b) *Phys. Rev. B*, **46**, 2172-2182

Smallman, C.G., Connell, S.H, Madiba, C.C.P. and Sellschop, J.P.F., (1996) *Nucl. Instr. and Meth. B*, **118**, 688-692

Sørensen, A.H. and Uggerhøj, E., (1989) *Nuclear Science Applications*, **3**, 147-205

Spits, R.A., Derry, T.E., Prins, J.F. and Sellschop, J.P.F., (1991) *Nucl. Instr. and Meth. B*, **59/60**, 1366-1371

Spits, R.A., Prins, J.F. and Derry, T.E., (1994) *Nucl. Instr. and Meth. B*, **85**, 347-351

Stoneham, A.M., (1992) in *The Properties of Natural and Synthetic Diamond*, ed. J.E. Field, Academic Press, London, p11-13

Stoquert, J.P., Guillaume, G., Hage-Ali, M., Grob, J.J., Ganter, C. and Siffert, P., (1989) *Nucl. Instr. and Meth. B*, **44**, 184-194

Storbeck, E.J., (1999) Ph.D. Thesis, University of the Witwatersrand

Talbot-Ponsonby, D.F., Newton, M.E., Baker, J.M., Scarsbrook, G.A., Sussmann, R.S. and Wort, C.J.H, (1996) *J. Phys. C*, **8**, 837-849

Talbot-Ponsonby, D.F., Newton, M.E., Baker, J.M., Scarsbrook, G.A., Sussmann, R.S., Whitehead, A.J. and Pfenninger, S., (1998a) *Phys. Rev. B*, **57**, 2264-2270

Talbot-Ponsonby, D.F., Newton, M.E., Baker, J.M., Scarsbrook, G.A., Sussmann, R.S. and Whitehead, A.J., (1998b) *Phys. Rev. B*, **57**, 2302-2309

Tamura, A. and Ohtsuki, Y.H., (1974) *Phys. stat. sol. (b)*, **62**, 477-480

Thomas, J.P., Fallavier, M., Ramdane, D., Chevarier, N. and Chevarier, A., (1983) *Nucl. Instr. and Meth.*, **218**, 125-128

Toulemonde, M., Bouffard, S. and Studer, F., (1994) *Nucl. instr. and Meth. B*, **91**, 108-123

Troullier, N. and Martins, J.L., (1991), *Phys. Rev. B*, **43**, 1993-2006

Turos, A. and Meyer, O., (1984) *Nucl. Instr. and Meth. B*, **4**, 92-97

Uggerhøj, E., (1966) *Phys. Lett.*, **22**, 382-383

Uzan-Saguy, C., Cytermann, C., Brener, R., Richter, V., Shaanan, M. and Kalish, R., (1995) *Appl. Phys. Lett.*, **67**, 1194-1196

Vainonen, E., Likonen, J., Ahlgren, T., Haussalo, P., Keinonen, J. and Wu, C.H., (1997) *J. Appl. Phys.*, **82**, 3791-3796

von Barth, U., (1992) in *Lectures on Methods of Electronic Structure calculations*, ed. Kumar, V., Andersen, O.K. and Mookerjee, A., World Scientific, p21-62

Vermeulen, L.A. and Farrer, R.G., (1975) *Diamond Research 1975 (Suppl. Ind. Diamond Rev.)*, 18

Wahl, U., Correia, J.G., Cardoso, S., Marques, J.G., Vantomme, A., Langouche, G. and the ISOLDE collaboration, (1998) *Nucl. Instr. and Meth B*, **136-138**, 744-750

Wahl, U. and the ISOLDE collaboration, (1997) *Phys. Rep.*, **280**, 145-285

Wahl, U., (1998), private communication

Wahl, U., Vantomme, A., Langouche, G. and the ISOLDE collaboration, (1999) *Nucl. Instr. and Meth. B*, **148**, 492-496

Wang, Z.G., Dufour, Ch., Paumier, E. and Toulemonde, M., (1994) *J. Phys. C*, **6**, 6733-6750

Weilhammer, P., Nygård, E., Dulinski, W., Czermak, A., Djama, F., Gadomski, S., Roe, S., Rudge, A., Schopper, F. and Strobel, J., (1996) *Nucl. Instr. and Meth. A*, **383**, 89-97

Whitlow, H.J., Keinonen, J., Hautala, M. and Hautojärvi, A., (1984) *Nucl. Instr. and Meth. B*, **5**, 505-510

Wichert, Th., Swanson, M.L. and Quenneville, A.F., (1986) *Phys. Rev. Lett.*, **57** 1757-1760

Wichert, Th., Skudlik, H., Deicher, M., Grübel, G., Keller, R., Recknagel, E. and Song, L., (1987) *Phys. Rev. Lett.*, **59**, 2087-2090

Wielunski, L., Benenson, R., Horn, K. and Lanford, W.A., (1986) *Nucl. Instr. and Meth. B*, **15**, 469-474

Wielunski, L.S., (1996) *Nucl. Instr. and Meth. B*, **118**, 256-261

Wielunski, L.S., Szilágyi, E. and Harding, G.L., (1998) *Nucl. Instr. and Meth. B*, **136-138**, 713-718

Williams, J.S. and Möller, W., (1978) *Nucl. Instr. and Meth.*, **157**, 213-221

Woods, G.S. and Collins, A.T., (1983) *J. Phys. Chem. Solids*, **44**, 471-475

Woods, G.S., (1994) in *Properties and Growth of Diamond*, ed. G. Davies, INSPEC, the Institution of Electrical Engineers, London, p83-84

Yin, M.T. and Cohen, M.L., (1982) *Phys. Rev. B*, **25**, 7403-7412

Yu, R. and Gustafsson, T., (1986) *Surf. Sci.*, **177**, L987-L993

Zhou, X., Watkins, G.D., McNamara Rutledge, K.M., Messmer, R.P. and Chawla, S., (1996), *Phys. Rev. B*, **54**, 7881-7890

Ziegler, J.F., Biersack, J.P. and Littmark, U., (1985) *The Stopping and Range of Ions in Solids*, Pergamon, New York

Ziegler, J.F., (1998) *Nucl. Instr. and Meth. B*, **136-138**, 141-146

Appendix A

Publications

1. **Lattice locations of indium implanted in diamond**
   Doyle, B.P., Dewhurst, J.K., Lowther, J.E. and Bharuth-Ram, K., (1998)
   Phys. Rev. B, **57**, 4965-4967

2. **3D-micro-ERDA microscopy of hydrogen distributions in diamond using a 2D-PSD with event reconstruction**
   Doyle, B.P., Maclear, R.D., Connell, S.H., Formenti, P., Machi, I.Z., Butler, J.E., Schaaff, P., Sellschop, J.P.F., Sideras-Haddad, E. and Bharuth-Ram,K., (1997)
   Nucl. Instr. and Meth. B, **130**, 204-210

3. **Study of indium-defect interactions in diamond using 2-D CEEC**
   Doyle, B.P., Storbeck, E.J., Wahl, U., Connell, S.H. and Sellschop, J.P.F., (2000)
   J. Phys. Condens. Matter, **12**, 67-78

4. **The Schonland Micro-Scanning Ion Beam Analysis Facility**
   Andeweg, A.H., Ballestrero, S., Beer, J.U.M., Butler, J.E., Breese, M.B.H., Connell, S.H., Dini, L., Doyle, B.P., Drummond, M.L., Formenti, P., Hart, R.J., Machi, I.Z., Maclear, R.D., McQueen, I.D., Schaaff, P., Sideras-Haddad, E., Sellschop, J.P.F. and Wernick, G., (1997)
   Nucl. Instr. and Meth. B, **130**, 37-44

5. **Site Occupancy and Molecular Complex Formation of 19F Ions in Fullerenes C60 and C70 Studied by TDPAD**

Bossenger, M.G., Connell, S.H., Sideras-Haddad, E., Appel, H., Doyle, B.P., Verwoerd, W., Bharuth-Ram, K., Sellschop, J.P.F., Fischer, C.G. and Nolting, V., (1999)
Hyperfine Interact., **120/121**, 557-562

6. **The solid state physics of hydrogen in diamond studied by micro-3D-ERDA**
Connell, S.H., Doyle, B.P., Machi, I.Z., Maclear, R.D., Nilen, R.W.N., Rebuli, D.B., Sellschop, J.P.F., Sideras-Haddad, E. and Butler, J.E., (2000)
Nucl. Instr. and Meth. B, submitted

7. **Hydrogen and Hydrogen-like Defects in Diamond**
Connell, S.H., Sellschop, J.P.F., Maclear, R.D., Doyle, B.P., Machi, I.Z., Nilen, R.W.N., Butler, J.E. and Bharuth-Ram, K., (1997)
Mat. Sci. For., **258-263**, 751-756

8. **A study of the mobility and trapping of minor hydrogen concentrations in diamond in three dimensions using quantitative ERDA microscopy**
Connell, S.H., Sellschop, J.P.F., Butler, J.E., Maclear, R.D., Doyle, B.P. and Machi, I.Z., (1998)
Diamond and Relat. Mater., **7**, 1714-1718

9. **Heavy ion and proton beams in high resolution imaging of a fungi spore specimen using STIM tomography**
Formenti, P., Breese, M.B.H., Connell, S.H., Doyle, B.P., Drummond, M.L., Machi, I.Z., Maclear, R.D., Schaaff, P., Sellschop, J.P.F., Bench, G., Sideras-Haddad, E., Antolak A. and Morse, D., (1997)
Nucl. Instr. and Meth. B, **130**, 230-236

10. **Diffusion Characteristics of Hydrogen in Diamond**
Machi, I.Z., Butler, J.E., Connell, S.H., Doyle, B.P., Maclear, R.D., Sellschop, J.P.F., Sideras-Haddad, E. and Rebuli, D.B., (1999)
Diamond and Relat. Mater., 8, 1611-1614

11. **Hydrogen mobility in diamond studies using HI-ERDA microscopy**
Machi, I.Z., Connell, S.H., Schaaff, P., Doyle, B.P., Maclear, R.D., Bharuth-Ram, K., Formenti, P. and Sellschop, J.P.F., (1997)
Nucl. Instr. and Meth. B, **127/128**, 212-216

12. **Muonium studies of p-type semi-conducting diamond under conditions of UV-visible illumination**
Machi, I.Z., Connell, S.H., Major, J., Smallman, C.G., Sellschop, J.P.F., Bharuth-Ram, K., Maclear, R.D., Doyle, B.P., Butler, J.E., Scheuermann, R. and Seeger, A., (1999)
Hyperfine Interact., **120/121**, 585-589

13. **Quantum diffusion of tetrahedral interstitial muonium in diamond**
Machi, I.Z., Connell, S.H., Sellschop, J.P.F., Smallman, C.G., Bharuth-Ram, K., Major, J., Doyle, B.P. and Maclear, R.D., (2000)
Physica B, submitted

14. **Quantitative trace hydrogen distributions in natural diamond using 3D-micro-ERDA microscopy**
Maclear, R.D., Connell, S.H., Doyle, B.P., Machi, I.Z., Butler, J.E., Sellschop, J.P.F., Naidoo S.R. and Fritsch, E., (1998)
Nucl. Instr. and Meth. B, **136-8**, 579-582

15. **The distribution of hydrogen in polycrystalline CVD diamond**
Maclear, R.D., Butler, J.E., Connell, S.H., Doyle, B.P., Machi, I.Z., Rebuli, D.B., Sellschop, J.P.F. and Sideras-Haddad, E., (1999)
Diamond and Relat. Mater., **8**, 1615-1619

16. **Oxygen on diamond surfaces**
Rebuli, D.B., Derry, T.E., Sideras-Haddad, E., Doyle, B.P., Maclear, R.D., Connell, S.H. and Sellschop, J.P.F., (1999)
Diamond and Relat. Mater., **8**, 1620-1622

17. **Oxygen Surface Studies in Ultra-Thin Diamond using a Resonance Reaction and Transmission Channeled Rutherford Forward Scattering**
Rebuli, D.B., Aggerholm, P., Butler, J.E., Connell, S.H., Derry, T.E., Doyle, B.P., Maclear, R.D., Sellschop, J.P.F. and Sideras-Haddad, E., (2000)
Nucl. Instr. and Meth. B, in press

Appendix B

Possible effects of the ^{111}In decay on the lattice site observed by CEEC

The decay of ^{111}In to the ground-state of ^{111}Cd is a dynamic process (see Figure 4.1), involving various nuclear and atomic processes that must be taken into account, when determining the information obtained via the emitted conversion electrons. In particular these include: 1) the neutrino recoil received by the nucleus in the electron capture (EC) decay, 2) the initial excited state of the ^{111}Cd and 3) the length of the various life-times of the excited states in the decay compared with the various other processes occurring during the same time interval.

The effect of the neutrino recoil is thought to be small. In the case of ^{118}Xe this is known to have an effect, imparting 49 eV to the daughter nuclei (Hofsäss *et al*, 1986). However the ^{118}Xe EC decay has a Q value of 3.3 MeV whereas the Q value of the ^{111}In decay is much smaller (866 keV) and thus much less energy will be imparted. Various authors note the presence of neutrino recoil,but do not not seem to consider it important with regards ^{111}In (Hofsäss and Lindner, 1991, and Lindner *et al*, 1986). More particularly PAC measurements using the isotope ^{111m}Cd, which does not have the EC decay, showed identical results to measurements performed by the same group on ^{111}In in diamond (Bharuth-Ram *et al*, 1998). This can be seen as proof of no substantial effect of the EC decay. It should be noted that the neutrino recoil has no preferred direction the lattice. Thus the displacement of the ^{111}In would be isotropic

in the crystal. The effect of this would be merely to increase the detected random fraction in the crystal.

The process of electron capture removes an electron from the K-shell of the atom, resulting in a highly excited electronic configuration. This ionization of the atom is fairly short lived, but in ionic materials can be of importance. In a molecular solid like diamond it should not have the same importance. The work of Bharuth-Ram mentioned above also disproves any such effect. The so -called after-effects present in PAC measurements due to this highly excited configuration (see for example Salomon, 1964), should not be relevant in CEEC, as their effect is merely to momentarily distort the atomic wavefunctions.

In the previous two paragraphs we have determined that the effect of the various dynamical processes on the position occupied by the probe atom is small. Thus the life-times of the excited states of ^{111}Cd (namely 120 ps and 85 ns), are unimportant. In summary the above processes (1-3) during the decay of ^{111}In to ^{111}Cd are not thought to significantly perturb the information obtained in a CEEC measurement.